

**Understanding written artefacts on rock-base supports at the
atomic-scale level: weathering and crystal chemistry of the rock-
forming minerals**

Dissertation

with the aim of achieving a doctoral degree
at the Faculty of Mathematics, Informatics and Natural Sciences
Department of Earth Sciences
at Universität Hamburg

submitted by
Stylios Aspiotis

Hamburg, 2022

Department of Earth Sciences

Date of Oral Defence:

28.02.2023

Reviewers:

Prof. Dr. Boriana Mihailova

Prof. Dr. Jochen Schlüter

Members of the examination commission:

Prof. Dr. Boriana Mihailova

Prof. Dr. Jochen Schlüter

Univ. Prof. Dr. Kaja Harter-Uibopuu

Prof. Dr. Stefan Jung

Prof. Dr. Markus Fischer

Chair of the Subject Doctoral Committee

Earth System Sciences:

Prof. Dr. Hermann Held

Dean of Faculty MIN:

Prof. Dr.-Ing. Norbert Ritter

Abstract

Raman spectroscopy is an analytical method applied in Earth's Sciences for structural and crystallochemical characterization of mineral phases and molecular inclusions that has gained popularity over the last three decades due to the introduction of more sensitive spectrometers and its truly preparation-free nature. The latter makes this method applicable to fields such as cultural heritage.

In this study, the ability of Raman spectroscopy for mapping the lateral distribution of weathering-related secondary phases or molecular species in a host matrix via the guest-to-host peak intensity ratio was utilized to detect differences between inscribed and non-inscribed areas of marble-based written artefacts. This approach can potentially be used to unravel vanished or hardly readable inscriptions on inorganic rock-based writing supports, which is extremely important for epigraphic and to cultural-heritage studies. In particular, two types of engraved marble characterized by different environmental conditions and inscription ages from Hamburg (Germany) and Asia Minor (western Turkey) have been analyzed by Raman spectroscopy, as well as by complementary powder X-ray diffraction (XRD), wavelength-dispersive electron microprobe analysis (WD-EMPA) and Fourier-transform infrared (FTIR) spectroscopy. The results clearly reveal that Raman spectroscopy is sensitive enough for detecting cracks introduced through the inscribing process, via the inhabiting weathering-related products or molecular species and can be used for tracking of faded or lost inscribed text. This is justified by the Raman intensity ratio between the strongest peak of weathering-related product ($\nu(\text{C}=\text{C}) \sim 1520 \text{ cm}^{-1}$ for carotenoids or the G peak $\sim 1595 \text{ cm}^{-1}$ for soot-like carbon) and the strongest peak of marble (CO_3 stretching near 1087 cm^{-1}), which is higher in value and can be detected at greater depths beneath inscribed letters than away from them. In addition, the nature of weathering-related products or foreign material inhabiting cracks is dictated by environmental conditions, since metabolic products produced by lichen and amorphous carbon are mostly found in the humid climate of Hamburg and the Mediterranean climate of Asia Minor, respectively. Moreover, weather-exposure time, mineral grain size and letter coloring are critical for the propagation of weathering-related products beneath and far from engraved areas.

For the second part of this project, the potential of Raman spectroscopy for the non-destructive crystallochemical characterization of layered silicates, important rock-forming minerals that can be found in cultural-heritage objects as well, has been explored by analyzing a series of biotite- and serpentine-group minerals as well as talc samples with various iron (Fe) contents. Particularly, 18 biotite samples

with various chemical compositions covering the whole biotite solid-solution series between the endmembers phlogopite ($\text{KMg}_3\text{AlSi}_3\text{O}_{10}(\text{OH})_2$) and annite ($\text{KFe}^{2+}_3\text{AlSi}_3\text{O}_{10}(\text{OH})_2$) have been studied by Raman spectroscopy combined with WD-EMPA and Mössbauer spectroscopy. The results show that Raman signals (peak positions ω , full widths at half maximum; FWHMs, and integrated intensities I) of the framework ($15\text{-}1215\text{ cm}^{-1}$) and OH-stretching ($3500\text{-}3800\text{ cm}^{-1}$) vibrations can be correlated with the contents of octahedrally (M -site) and tetrahedrally (T -site) coordinated cations, as well as with the content of cations occupying the interlayered space. According to the established correlation trends, the content of major M -site cations such as Mg, Fe^{2+} and Fe^{3+} can be calculated based on the one-mode behavior of the MO_6 vibrations and the two-mode behavior of the OH-stretching vibrations with relative uncertainties smaller than 8%. Accordingly, TO_4 -ring modes can be used for the quantification of M -site Ti content and T -site Si and Al amounts, while the stretching and bending vibration at $\sim 730\text{ cm}^{-1}$ for the estimation of K content in the interlayer space and indirectly of vacancies related to it.

The same methodological approach was applied to Mg-dominant phyllosilicates with empty interlayer space, which can be found in cultural-heritage objects, namely serpentine ($\text{Mg}_3\text{Si}_2\text{O}_5(\text{OH})_4$) and talc ($\text{Mg}_3\text{Si}_4\text{O}_{10}(\text{OH})_2$), where a series of 22 and 10 samples, respectively have been analyzed by Raman spectroscopy and WD-EMPA. The Raman spectral profiles of the OH-stretching region of serpentine can be applied as a tool to distinguish the main serpentine minerals. The established calibration curves between the Raman signals of the framework vibrations and the crystal chemistry of serpentine and talc samples can be used for the quantification of $^{\text{M}}\text{Mg}$ and $^{\text{M}}\text{Fe}^{2+}$ contents in serpentine and $^{\text{M}}\text{Mg}$ amount in talc with relative uncertainties of ~ 5 , 5 , and $2\text{-}3\%$, respectively.

Our results demonstrate that: (i) the Raman signals of weathering-related products inhabiting cracks formed during the engraving can potentially be used to improve the readability of an inscribed text affected by rock weathering and in general, Raman spectroscopy can help understanding rock-weathering processes on atomic-scale level and (ii) the determination of the crystal chemistry of phyllosilicates can be a marker of provenance, thus benefiting cultural-heritage studies, where sampling is mostly prohibitive, and can be broadly applied in Geosciences, for instance to grains in polished and glass-covered thin sections or in crude rock samples, thereby assisting to the understanding of the mineral formation and alteration processes.

Zusammenfassung

Die Ramanspektroskopie ist eine analytische Methode, die in den Geowissenschaften zur strukturellen und kristallchemischen Charakterisierung von Mineralphasen und molekularen Einschlüssen eingesetzt wird und die in den letzten drei Jahrzehnten aufgrund der Einführung empfindlicherer Spektrometer und der Tatsache, dass sie Proben zerstörungsfrei analysieren kann, an Popularität gewonnen hat. Das letztere Merkmal macht diese Methode immer mehr zu einem sehr wertvollen Instrument bei der Erforschung unseres Kulturerbes.

In dieser Studie wurde die Fähigkeit der Ramanspektroskopie, die laterale Verteilung verwitterungsbedingten Sekundärphasen oder molekularen Spezies in einer Wirtsmatrix mittels des Intensitätsverhältnisses der Peaks von Gast- und Wirtsmaterial abzubilden, genutzt, um Unterschiede zwischen beschrifteten und nicht-beschrifteten Bereichen von Marmorartefakten zu erkennen. Diese Methode kann voraussichtlich in Zukunft dazu verwendet werden, verschwundene oder schwer lesbare Inschriften auf anorganischen gesteinsbasierten Schriftträgern zu rekonstruieren bzw. zu entschlüsseln und dadurch die Epigraphik zu unterstützen und bei der Erforschung unseres Kulturerbes beizutragen. Insbesondere wurden zwei gravierte Marmore aus Hamburg (Deutschland) und Kleinasien (Westtürkei), die durch unterschiedliche Umweltbedingungen und Inschriftenalter gekennzeichnet sind, mittels Ramanspektroskopie, Röntgenpulverdiffraktometrie (XRD), wellenlängen-dispersiver Elektronenstrahl-Mikrosonde (WD-EMPA), und Fourier-Transform-Infrarotspektrometrie (FTIR) untersucht. Die Ergebnisse zeigen deutlich, dass die Ramanspektroskopie empfindlich genug ist, um Risse im Gestein, die durch den Beschriftungsprozess unterhalb von Schriftzügen entstanden sind, über die darin enthaltenen Verwitterungsprodukte oder Molekülspezies aufzuspüren. Somit kann diese Methode zur Nachverfolgung verblasster oder verlorener Inschriften verwendet werden. Dies ist über das Verhältnis der Raman-Intensität zwischen dem stärksten Peak des Verwitterungsprodukts ($\nu(\text{C}=\text{C}) \sim 1520 \text{ cm}^{-1}$ für Carotinoide oder dem G-Peak $\sim 1595 \text{ cm}^{-1}$ für rußähnlichen Kohlenstoff) und dem stärkeren Peak des Marmors (CO_3 Streckschwingung bei 1087 cm^{-1}) möglich. Die Natur der Verwitterungsprodukte beziehungsweise des Fremdmaterials in den Rissen wird durch die Umweltbedingungen bestimmt, da Stoffwechselprodukte von Flechten oder amorpher Kohlenstoff vor allem im feuchten Klima Hamburgs beziehungsweise im mediterranen Klima Kleinasiens auftreten. Außerdem sind die Dauer der Verwitterung, die Korngröße der Minerale, das Korngefüge, und die möglicherweise ursprüngliche Abdeckung der eingravierten

Buchstaben durch Farbmittel entscheidend für die Ausbreitung der Verwitterungsprodukte unterhalb und entfernt von den eingravierten Bereichen.

Im zweiten Teil dieses Projektes wurde das Potential der Ramanspektroskopie für die zerstörungsfreie kristallchemische Charakterisierung von Schichtsilikaten, wichtigen gesteinsbildenden Mineralen, die auch in Objekten des Kulturerbes zu finden sind, durch die Analyse einer Reihe von Mineralen der Biotit- und Serpentinegruppe sowie von Talkproben mit unterschiedlichen Eisengehalten (Fe) untersucht. Insbesondere wurden 18 Biotitproben mit unterschiedlichen chemischen Zusammensetzungen, die die gesamte Biotit-Mischkristallreihe zwischen den Endgliedern Phlogopit ($\text{KMg}_3\text{AlSi}_3\text{O}_{10}(\text{OH})_2$) und Annit ($\text{KFe}^{2+}_3\text{AlSi}_3\text{O}_{10}(\text{OH})_2$) abdecken, durch Ramanspektroskopie in Kombination mit WD-EMPA und Mössbauer-Spektroskopie untersucht. Die Ergebnisse zeigen, dass die Raman-Signale (Peak-Positionen ω , Halbwertsbreiten FWHM, und integrierte Intensitäten I) der Gerüstschwingungen ($15\text{-}1215\text{ cm}^{-1}$) und der OH- Streckschwingungen ($3500\text{-}3800\text{ cm}^{-1}$) mit dem Gehalt an oktaedrisch (M -Position) und tetraedrisch (T -Position) koordinierten Kationen sowie mit dem Gehalt an Kationen, die die Schichtzwischenräume besetzen, korreliert werden können. Auf der Basis der sich daraus ergebenden Korrelationstrends kann der Gehalt an Hauptkationen der M -Position, wie Mg, Fe^{2+} und Fe^{3+} auf der Grundlage des Ein-Moden-Verhaltens der MO_6 -Schwingungen und des Zwei-Moden-Verhaltens der OH-Streckschwingungen mit relativen Unsicherheiten von weniger als 8% berechnet werden. Dementsprechend können die TO_4 -Ringmoden zur Quantifizierung des Ti-Gehaltes an der M -Position und der Si- und Al-Anteile an der T -Position verwendet werden, während die Streck- und Deformationsschwingung bei $\sim 730\text{ cm}^{-1}$ zur Einschätzung des K-Gehaltes im Schichtzwischenraum und indirekt auch der damit verbundenen Leerstellen dienen.

Der gleiche methodische Ansatz wurde auf Mg-dominante Schichtsilikate mit leerem Schichtzwischenraum angewandt, die ebenfalls in Objekten des Kulturerbes vorkommen. Dazu wurden 22 Serpentin- ($\text{Mg}_3\text{Si}_2\text{O}_5(\text{OH})_4$) und 10 Talkproben ($\text{Mg}_3\text{Si}_4\text{O}_{10}(\text{OH})_2$) mittels Ramanspektroskopie und WD-EMPA analysiert. Die Raman-Spektralprofile des OH-Streckschwingungsbereiches von Serpentin können als Hilfsmittel zur Unterscheidung der wichtigsten Serpentinminerale verwendet werden. Die etablierten Kalibrierungskurven zwischen den Raman-Signalen der Gerüstschwingungen und der Kristallchemie der Serpentin- und Talkproben können zur Quantifizierung des $^{\text{M}}\text{Mg}$ - und $^{\text{M}}\text{Fe}^{2+}$ -Gehaltes in Serpentin- und der $^{\text{M}}\text{Mg}$ -Menge in Talk mit relativen Unsicherheiten von $\sim 5, 5$, beziehungsweise 2-3% benutzt werden.

Unsere Ergebnisse weisen darauf hin, dass: (i) die Raman-Signale von Verwitterungsprodukten in Rissen, die durch den Beschriftungsprozess entstanden sind, potenziell genutzt werden können, um die Lesbarkeit eines eingravierten Textes zu verbessern, der von der Gesteinsverwitterung betroffen ist, und dass die Ramanspektroskopie generell zum Verständnis von Gesteinsverwitterungsprozessen auf atomarer Ebene beitragen kann und (ii) die durch ramanspektroskopische Analysen ermittelte Kristallchemie von Schichtsilikaten gegebenenfalls ein Herkunftsmerkmal sein kann und dadurch kulturhistorische Studien unterstützen, wo eine Probennahme überhaupt nicht erlaubt ist. Außerdem, kann die hier erarbeitete kristallchemische Charakterisierung von Schichtsilikaten in den Geowissenschaften allgemein angewandt werden, z.B. auf Körner in polierten oder abgedeckten Dünnschliffen oder an Rohgesteinsproben, und dadurch zum Verständnis der Genese und Alteration von Gesteinen beitragen.

Table of contents

1. Motivation	1
2. Objectives	5
3. Results and discussion	6
a. Weathering-induced changes in engraved marble	6
b. Raman spectroscopy for crystallochemical analysis of layered silicates	10
4. Outline and future research	18
Acknowledgments	19
References	20
Appendix	i
A. Publications	i
a. List of publications related to the doctoral thesis	i
b. Other publications	i
c. Contributions to conferences/workshops related to the doctoral thesis	i
d. Other contributions to conferences/workshops	ii
B. Publication 1	iii
a. Crack-enhanced weathering in inscribed marble: a possible application in epigraphy	iii
b. Supplementary material	xxvii
C. Publication 2	xxxii
a. Non-destructive determination of the biotite crystal chemistry using Raman spectroscopy: how far we can go?	xxxii
b. Supplementary material	lxi
Versicherung an Eides statt	lxviii

1. Motivation

Knowledge of the roots and development of ancient civilizations is mainly owed to the content of written artefacts, as written language is the most secure way of transmitting valuable information through time. Among different writing supports that have been used since the introduction of written artefacts in Mesopotamia already during the 4th millennium BCE (e.g. Artioli, 2010; Michel, 2021), inorganic rock-based inscriptions, for instance cuneiform clay tablets and marble plaques, are known to be the most persistent and widespread in time. Thus, mineralogical analyses of rock-based writing supports can deliver valuable information about peculiar characteristics of societies, besides the message of the engraved text. However, as any rock, rock-based engravings are subjected to weathering, as they are mostly exposed to diverse environmental conditions that can cause the in-situ deterioration and alteration of the superficial rock layers. As a result, inscriptions are severely affected by weathering-related processes and can become hardly readable or entirely disappear. This raises a challenging task to material sciences, which is to develop non-destructive methods able to unravel lost or heavily damaged inscribed text.

Weathering-related changes in rock inscriptions can cause the formation of new mineral phases, such as metal oxalates (Frost and Weier, 2003) and incorporation of microorganisms such as fungi or lichen together with their metabolic products (Holder et al., 2000; Gadd, 2017). Foreign molecular species like airborne particles and soot; signs of urban environmental pollution (Wentzel et al., 2003; Engling and Gelencsér, 2010; Gieré and Querol, 2010; Grobéty et al., 2010), can be found as well on the surface and into the host mineral matrix (Edwards and Farwell, 2008). Overall, the formation and deposition of such weathering-related products on rock-based writing supports depends on the local climate in terms of humidity, temperature, and urbanization of the area (Dragovich, 1991; Cooke et al., 1995; Frost and Weier, 2003) and on the actual position of the engraved object, which specifies the extent of exposure to rain, sun, and wind (Moropoulou et al., 1998).

It is highly anticipated that a common feature among different rock-based written artefacts will be the higher density of microcracks and extended structural defects near inscribed areas compared to non-inscribed ones, which have been introduced during the mechanical treatment of the engraving process (Fig. 1: Aspiotis et al., 2021b). Therefore, the content of newly formed minerals or molecular inclusions should be higher beneath engraved letters than away from them and non-destructive methods that can identify

such weathering-related products may help to recover unreadable inscribed text on rock-based writing supports.

So far, the chemical composition and structure of weathering-related products on the surface of epigraphic stone objects and monuments, as well as of the conservation state of cultural-heritage objects has been analyzed by X-ray fluorescence (XRF), atomic absorption and emission spectroscopy, EMPA, FTIR, and Raman spectroscopy (e.g. Moropoulou et al., 1998; Powers et al., 2005; Twilley, 2006; Edwards and Farwell, 2008; Pinna et al., 2015). Moreover, none of the aforementioned studies focused on material differences between inscribed and non-inscribed areas of the same specimen. It should be noted that most of these analytical methods require sampling, which is strongly undesirable or entirely prohibitive in the field of cultural heritage. Accordingly, non-invasive and preparation-free methods are favoured, which include XRF reflection, FTIR and Raman spectroscopy. An attempt has been made to unravel the already hardly readable inscribed text using XRF mapping on Fe (Powers et al., 2005), but the analysis failed to recover the lost engravings, while the instrumental limitations of FTIR in reflection mode complicate the analysis of rough surfaces.

As a result, the ability of Raman spectroscopy to non-destructively map the spatial distribution of secondary phases (i.e. weathering-related products) in a host matrix (i.e. rock-based writing support) via the guest-to-host intensity ratio, has the great potential to yield a novel non-destructive technique for the visualization of damaged or lost rock-based engravings. Further advantages of Raman spectroscopy highlight its importance in the current study, such as: (a) the ability to identify crystalline and amorphous phases (e.g. carbonaceous material), (b) the detection of light element-containing (H- and C-bearing) compounds; for instance carotenoids in lichen, and (c) beam focusing down to 1-2 μm , by using a microscope, eliminates the surface-roughness-issue confronted in FTIR spectroscopy.

The identification of weathering-related products and of the factors that influence their propagation beneath inscribed and non-inscribed areas via non-destructive analytical methods is of great importance. An arising challenge is the determination of the crystal chemistry of mineral groups that can be found as weathering products on the surface of silicate-based rocks, by applying the same non-destructive analytical method. One of the most important groups of rock-forming minerals participating in alteration and metamorphic processes of silicate rocks are phyllosilicates. Among them, trioctahedral layered silicates such as biotite ($\text{K}(\text{Mg}, \text{Fe}^{2+}, \text{Fe}^{3+}, \text{Al})_3 \text{AlSi}_3 \text{O}_{10}(\text{OH}, \text{F})_2$), serpentine-group minerals ($\text{Mg}_3 \text{Si}_2 \text{O}_5(\text{OH})_4$, and talc ($\text{Mg}_3 \text{Si}_4 \text{O}_{10}(\text{OH})_2$), are common minerals of igneous and metamorphic rocks that can be formed in a wide range of geological conditions (e.g. Scordari et al., 2006). Based upon the

arrangement of tetrahedral (*Ts*) and octahedral sheets (*Os*), as well as the presence or absence of interlayer species (*A*-site), serpentine, talc and biotite are characterized by the *Ts-Os*, *Ts-Os-Ts*, and *Ts-Os-Ts-A* stacking sequences, respectively (Wang et al., 2015). Hence, the physicochemical characteristics of layered silicates can provide a better insight of the processes of mineral formation, magma differentiation and alteration (e.g. Środoń, 1999; Scordari et al., 2012, 2013). Meanwhile, the importance of these phyllosilicates expands to the field of cultural heritage as well, since they can be found in cylinder seals (Zazoff, 1983), inscribed gems (Wang et al., 2013; Bersani and Lottici, 2016; Mihailova et al., 2021), earth pigments (Hradil et al., 2011; Košářová et al., 2013; Corradini et al., 2021) and decoration-related ceramics (Bersani and Lottici, 2016; El Halim et al., 2018).

Commonly, XRD and WD-EMPA are the most suitable methods for crystallochemical characterization of minerals, where sampling is necessary, which is strongly undesirable from the viewpoint of cultural heritage, due to the uniqueness of the examined sample. Furthermore, sample preparation, measurement duration and data evaluation can be time consuming. Thus, non-destructive preparation-free and easy-to-handle analytical methods, such XRF operating in reflection mode, are preferred as they can serve as an alternative to characterize chemically a sample. However, XRF cannot separate different mineral phases within a polycrystalline material, as the final output is an average chemical composition given in oxide weight percent (wt. %) of the analyzed rock sample. In the contrary, Raman spectroscopy can determine the exact elemental distribution within each single mineral-phase because vibrational phonon modes are both sensitive to chemistry and structure. Consequently, Raman spectroscopy has successfully been applied for the establishment of quantitative relationships between the crystallochemical composition and the Raman signals (ω , I , and FWHMs) of silicates (Huang et al., 2000; Bendel and Schmidt, 2008; Prencipe et al., 2012) and complex hydrous silicate minerals (Leissner et al., 2015; Watenphul et al., 2016a, b; Waesermann et al., 2020).

Up to now, cationic distribution over the tetrahedral and octahedral sites of these phyllosilicates, and substitutional mechanisms have thoroughly been studied on natural and synthetic samples by various analytical techniques such as single-crystal XRD, WD-EMPA and Mössbauer spectroscopy (e.g. Fuchs et al., 1998; Redhammer et al., 2002; Gatta et al., 2013). In addition, biotite, talc, and serpentine-group minerals (antigorite, chrysotile and lizardite), have been studied over the last three decades by FTIR and Raman spectroscopy. In the case of serpentine, intergrowths can be observed leading to two further fibrous serpentine varieties, i.e. polyhedral and polygonal (PS) serpentine, with typical alternating curved and flat domains in an onion-like wrapped (Baronnet et al., 2007; Andreani et al., 2008) and polygonised

(Baronnet and Devouard, 1996; Tarling et al., 2018) morphology, respectively. The assignment of the framework ($15\text{-}1215\text{ cm}^{-1}$) and OH-stretching vibrations ($3500\text{-}3800\text{ cm}^{-1}$) to certain atomic displacements facilitated the distinction between different serpentine- and biotite-group minerals (e.g. McKeown et al., 1999; Auzende et al., 2004; Wang et al., 2015; Fritsch et al., 2021). In particular, the comprehensive analysis of the OH-stretching region of these layered silicates led to the assignment of the observed peaks to specific octahedrally coordinated cationic *MMM* triplets (e.g. Redhammer et al., 2000; Petit et al., 2004; Scordari et al., 2012; Fritsch et al., 2021). An attempt by Wang et al. (2015) has been made to linearly correlate the amount of Fe in biotite with the Raman peak positions at ~ 730 and $\sim 780\text{ cm}^{-1}$, characteristic of the TO_4 stretching and bending vibrations, although without separating $^{\text{M}}\text{Fe}$ from $^{\text{T}}\text{Fe}$ and without specifying the valence state of Fe. Moreover, Raman spectroscopic analysis of an insufficient number of samples (a total of 4) belonging to the biotite-group minerals that have been analyzed by Tlili et al. (1989) showed a linear trend between ω_{195} and Al contents at both tetrahedral and octahedral sites. It has also been reported that the FTIR peak around 3680 cm^{-1} in antigorite, which is related to the in-phase stretching of interlayer OH groups, shifts towards lower wavenumbers with increasing $^{\text{M}}\text{Fe}^{2+}$ and $^{\text{M}}\text{Al}$ contents and that the integrated intensity of the FTIR band at 3625 cm^{-1} is increasing with increasing $^{\text{M}}\text{Fe}^{2+}$ content (Uehara and Shirozu, 1985). However, neither the behavior of the OH-stretching peaks of the other two serpentine minerals nor the dependence of the framework vibrations on the crystal chemistry has been thoroughly analyzed. Correlation trends between the crystallochemical composition and FTIR signals (FWHM and integrated intensities) of the OH-stretching region in talc delivered reliable quantifications of the octahedrally coordinated cations (Petit et al., 2004), although the vibrational modes between $15\text{-}1215\text{ cm}^{-1}$ were not considered. Consequently, a systematic description, according to a non-destructive analytical method, of the behavior of the Raman spectral features of these layered silicates, namely talc, serpentine- and biotite-group minerals, as a function of their crystallochemical composition is missing.

2. Objectives

The goal of this study was twofold: first to comprehensively analyze the weathering-induced changes beneath inscribed and non-inscribed regions of marble-based written artefacts in different atmospheric environments engraved in different time periods. Suitable samples were engraved marble headstones from the cemetery of Hamburg (with 66 ± 14 -year-old inscriptions) and engraved marble segments from Asia Minor (with ~ 2000 -year-old inscriptions), which have been subjected to Raman spectroscopy and complementary XRD, WD-EMPA, and FTIR spectroscopy.

Second, to thoroughly study the relationship between the crystal chemistry and Raman scattering arising from the framework and OH-stretching vibrations of selected phyllosilicates by establishing correlation curves. A series of 22 serpentine-group minerals, 10 talc samples with different Fe contents, and 18 biotite samples along the phlogopite-annite join were selected and studied by Raman spectroscopy and WD-EMPA. The biotite samples were also analyzed to verify the fractionation of Fe^{2+} and Fe^{3+} over both tetrahedral and octahedral sites. The aim was to establish quantitative relations between the Raman spectral parameters and the content of major and minor elements, as the latter are significant crystallographic markers that may advance provenance studies, especially in the field of cultural heritage.

The expected results from both parts of my Ph.D. study have large implication in Mineralogy and Geosciences in general, since they can help elucidating weathering processes on atomic-scale level and facilitate the crystallochemical analyses of mineral assemblages.

3. Results and discussion

This section is based on the papers:

- i. *Aspiotis, S., Schlüter, J., Harter-Uibopuu, K. and Mihailova, M.: Crack-enhanced weathering in inscribed marble: a possible application in epigraphy. Eur. J. Mineral., 33, 189-202, 2021b.*
- ii. *Aspiotis, S., Schlüter, J., Redhammer, G.J., and Mihailova, B.: Non-destructive determination of the biotite crystal chemistry using Raman spectroscopy: how far we can go? Eur. J. Mineral., 34, 573-590, 2022.*
- iii. *Aspiotis, S., Schlüter, J., and Mihailova, B.: Raman spectroscopy for crystallochemical analysis of Mg-rich 1:1 layer silicates: serpentine polymorphs and talc. J. Raman Spectrosc., submitted, JRS-23-0177.*

3.a. Weathering-induced changes in engraved marble

To testify our working hypothesis, cross-section cuts through the inscribed and non-inscribed areas of the same specimen have been prepared from the engraved marble headstones of the cemetery of Hamburg (Fig. 2: Aspiotis et al., 2021b) and the marble segments of Asia Minor. Raman measurements on samples listed in Table 1 (Aspiotis et al., 2021b) were conducted along line profiles beneath and away from engravings, where the first measurement was on the surface of the cross section and the final reached a depth of either 1 or 2 mm. Additional cuts were prepared for WD-EMPA and the results of the mineral-phase composition of the analyzed samples, according to WD-EMP and powder XRD analyses, are given in Table 1 (Aspiotis et al., 2021b). For the purposes of powder XRD and FTIR analyses, samples AM_C1 (Asia Minor) and MaB1A (Hamburg) were selected as representative and material was gently scraped under the microscope from the surface of altered and unaltered areas.

As expected, XRD analyses showed that marble from both localities is composed of calcite (CaCO_3) with minor quantities of accessory dolomite ($\text{CaMg}(\text{CO}_3)_2$) and quartz (SiO_2), without being able to spot any differences between inscribed and non-inscribed areas of the same specimen. Besides, EMPA data indicated the relatively homogenous distribution of minor phosphate phase, probably apatite ($\text{Ca}_5(\text{PO}_4)_3(\text{F},\text{Cl},\text{OH})$), in both the matrix and altered layer of all studied marble specimens. Micas, feldspars, fluorite (CaF_2) and pyrite (FeS_2) were found as random inclusions either in the unaltered mass or within the alteration zone of engraved marbles of Asia Minor and Hamburg, without being

systematically associated with one of them. However, WD-EMP analyses accompanied by backscattered electron (BSE) images and chemical element maps of the studied cross sections (Fig. 4, 5: Aspiotis et al., 2021b), noted the first obvious difference between samples of Hamburg and Asia Minor, which is a much thicker alteration rim of the latter one being associated with longer exposure time to weathering. Otherwise, the altered layer of both marble types is characterized by decreasing Ca and increasing C contents, indicating degradation of calcite, a phenomenon that can be observed along the induced irregular cracks in the marble matrix beneath engraved areas, as well as along natural cracks following the cleavage planes or twin boundaries of calcite. In the altered areas, enrichment in Fe, Mg, Al, Si, K, S, P, and N (Fig. 4, 5, and Supplement: Aspiotis et al., 2021b) can be related to incorporation of micrometre-sized weathering-related products, such as phyllosilicates, from airborne natural mineral dust or as an effect of the urban environment (e.g. Grobéty et al., 2010).

FTIR results clearly imply that compositional differences occur between the alteration zone and the unaltered mass of engraved marble from both localities and can be mainly observed by the presence of additional IR peaks (marked with red in Fig. 6: Aspiotis et al., 2021b) centred at ~ 1047 , 1072 , 1084 , 1132 , 1267 , 1724 , 2931 , and 3447 cm^{-1} . The peak at 1047 cm^{-1} can be attributed to the $\nu_3(\text{PO}_4^{3-})$ antisymmetric stretching of apatite (e.g. Markovic et al., 2004; Balan et al., 2011), while the peak at 1072 cm^{-1} can be a sign of the SiO_4 antisymmetric stretching in layered silicates like muscovite (e.g. Singha and Singh, 2016). These observations can further be supported by the elevated concentrations of P, Al, Si, and K in the alteration zone of inscribed marble, which was indicated by the WD-EMP data. The peaks at 1084 cm^{-1} and 1132 cm^{-1} are assigned to the strongest absorption bands of quartz (Saikia et al., 2008) and gypsum ($\text{CaSO}_4 \cdot 2\text{H}_2\text{O}$), (Bishop et al., 2014), respectively, while the peaks at 1267 , 1724 , 2931 cm^{-1} to organic compounds or to biological activity connected to lichen and their metabolic products, such as oxalic acid (Coates, 2000). Since oxalic acid is the most important bioweathering agent produced by lichens, it can lead to the secondary formation of calcium oxalates, after its reaction with carbonates (Gadd, 2017), like whewellite ($\text{CaC}_2\text{O}_4 \cdot \text{H}_2\text{O}$), with its characteristic peak at 1267 cm^{-1} (e.g. Frost, 2004) being suppressed by the strongest IR peak of calcite (Pinna et al. 2015). The broad IR band near 3447 cm^{-1} , arising from O-H bond stretching, is most probably due to H_2O incorporated in microvoids and defect OH^- groups on internal surfaces, which is systematically stronger in the IR spectra of the altered marble areas (Fig. 6: Aspiotis et al., 2021b). Hydrus minerals like gypsum and whewellite may also contribute to this band.

Nevertheless, XRD, WD-EMPA, and FTIR could not demonstrate any difference between inscribed and non-inscribed areas of the same sample, which is still the main open question of this study. Raman

spectra beneath inscribed areas of the coarse-grained marbles of Hamburg showed the presence of weathering-related products at the first 100 μm from the surface, via their characteristic peaks at 1154 and 1517 cm^{-1} (Fig. 7a: Aspiotis et al., 2021b), whereas away from engravings they are confined at the 50 μm from the surface. This observation confirms that the inscription introduces cracks and microvoids facilitating thereby the formation and propagation of weathering-related products through the bulk and allow the host to be infiltrated by foreign substances. The peaks at 1154 and 1517 cm^{-1} match very well the $\nu(\text{C}-\text{C})$ and $\nu(\text{C}=\text{C})$ stretching modes of carotenoids in lichen, respectively (Holder et al., 2000; Edwards et al., 2003). As can be noted in Fig. 7a, additional peaks at 960 and 1005 cm^{-1} can be spotted at the first 50-100 μm beneath inscriptions and can be attributed to the symmetric PO_4 stretching mode of apatite (Edwards et al., 2004; Jegova et al., 2013; Litasov and Podgornykh, 2017) and to the $\nu_1(\text{SO}_4)$ symmetric stretching mode of gypsum (Takahashi et al., 1983; Prasad et al., 2001), respectively. The extra peaks at ~ 1187 and 1278 cm^{-1} can be ascribed to the aromatic ring breathing typical of diverse organic compounds and the $\text{CH}_2=\text{CH}_2$ in-plane rocking mode of alkenes (e.g. Holder et al., 2000), respectively.

The fine-grained marbles from Ohlsdorf, after 60-70 years of weathering, demonstrated identical Raman spectra beneath inscribed (Fig. 7c: Aspiotis et al., 2021b) and non-inscribed regions of the same sample, indicating that the mineral grain size is an important factor for the propagation of weathering-related products. However, this may change when a written artefact is exposed to weathering for a much longer period.

Another factor that suppresses the presence of weathering-related products beneath inscriptions is letter colouring, as some of the engraved letter on the coarse-grained marble headstones of Ohlsdorf were coloured white. In particular, the superficial layer (0 μm) displays a very strong peak at 152 cm^{-1} and 5 weaker peaks at ~ 204 , 335, 390, 506, and 628 cm^{-1} (Fig. 7b, S5: Aspiotis et al., 2021b). These peaks are typical of synthetic nanosized anatase (TiO_2) with a large internal surface, which is used in white pigments (Sahoo et al., 2009). Despite that, it should be mentioned that the observed Raman peaks of nanosized anatase are broader and shifted compared to those of well crystalline anatase due to the competing phonon confinement effect and the impact of inherent structural defects (Zhang et al., 2000). As a result, TiO_2 -based pigments prevent lichen formation on inscriptions, but may be used at the same time as potential trackers for hardly readable inscriptions.

The comparison of Fig. 7a with 7d (Aspiotis et al., 2021b) revealed that local climate influences the nature of the weathering-related products inhabiting cracks. Two broad additional peaks centered around 1365 and 1595 cm^{-1} , which at depths of ~ 60 -120 μm were systematically stronger beneath the inscription

than away from it, characterize the line profiles beneath engraved areas of medium- to coarse-grained marbles from Asia Minor. The peaks can be attributed to the so-called D (diamond-like) and G (graphite-like) peaks in amorphous carbon arising from the ring breathing and C–C bond stretching of sp²-hybridized C (e.g. Ferrari and Robertson, 2004), respectively. The presence of aragonite instead of calcite within the first 50 μm beneath the engravings (Fig. 7d: Aspiotis et al., 2021b) seems to be statistically irrelevant, at least for the sole inscribed marble from Asia Minor and further experiments are needed to state whether the existence of aragonite is indeed a feature of engraved areas only subjected to Mediterranean climate. Thus, the dominant weathering-related product in engraved letters of Asia Minor seems to be soot-like carbon, while in inscribed marble from Hamburg carotenoids produced by lichen and gypsum mark the corresponding line profiles.

To quantify the abundance and penetration depth of the extra phases (lichen and amorphous C) the integrated intensity of the strongest Raman peak of the corresponding guest compound [$\nu(\text{C}=\text{C}) \sim 1520 \text{ cm}^{-1}$ for carotenoids and the G peak $\sim 1595 \text{ cm}^{-1}$ for soot-like carbon] normalized to that of the major peak of the host matrix (CO_3 stretching near 1087 cm^{-1}) was used. The resulting intensity ratios, $\rho_1 = I_{1595}/I_{1086}$ for Asia Minor and $\rho_2 = I_{1520}/I_{1087}$ for Hamburg, were plotted against the distance to the surface beneath and away from inscriptions as can be seen in Fig. 8 (Aspiotis et al., 2021b). The evolution of the data points can be fitted with an asymmetric lognormal statistical distribution $\rho_1(d) = \frac{A}{\sqrt{2\pi}wd} e^{-\left(\ln\left(\frac{d}{d_c}\right)\right)^2/(2w^2)}$ and with an exponential function $\rho_2(d) = Ae^{-d/t}$, respectively. Dispersion of points is large but apparently, a maximum can be observed for both cases, which is around 60 μm for the non-inscribed areas and around 70–80 μm for the inscribed areas of engraved marbles from Asia Minor. In general, the strong Raman signal from sp²-hybridized C–C bond stretching is more pronounced beneath inscriptions than away from them, as being shown from $\rho_1(d)$ values that are higher and persist at greater depths beneath engraved areas than beneath untreated ones. Therefore, this Raman signal is a feasible way to scan the lateral distribution of cracks in weathered marble containing amorphous carbon (Asia Minor).

In the case of inscribed marble from Hamburg, ρ_2 intensity ratio decreases rapidly with depth, but the Raman signal from $\nu(\text{C}=\text{C})$ of carotenoids can be identified at depths up to $\sim 100 \text{ μm}$ beneath engraved letters of the coarse-grained marbles, whilst away from them carotenoids were less abundant and limited within the first 50 μm from the surface. Thus, the abundance of metabolic products, i.e. carotenoids produced by lichen, is apparently enhanced beneath the inscribed areas of the coarse-grained gravestones.

Finally, the presence of gypsum that has been monitored by FTIR and Raman spectroscopy in the outer altered film of the coarse-grained gravestones (Hamburg) beneath and away from inscribed letters can be used as a sign of inscribed areas. Particularly, gypsum could be detected via Raman spectroscopy at a depth of 50–100 μm beneath inscriptions and to a lesser extent, or entirely not, at a depth of 0–50 μm beneath untreated areas of the same cuts. Thus, the critical depth of 50 μm is the threshold of inscribed areas only, and similarly to carotenoids and carbonaceous material gypsum formation is facilitated by cracks induced during the inscribing process.

3.b. Raman spectroscopy for crystallochemical analysis of layered silicates

Reliable relationships between the mineral chemical composition and Raman parameters (ω , FWHMs, and I) require a precise determination of the chemical composition of the mineral samples used to establish calibration curves. WD-EMPA was performed on selected biotites, expanding over the whole biotite solid-solution series (Table 1 and S1: Aspiotis et al., 2022), serpentine-group minerals and talc samples (Aspiotis et al., *submitted*). According to the Excel spreadsheet of Li et al. (2020) the contents of hydroxyl groups, $^T\text{Fe}^{3+}$ and $^M\text{Fe}^{3+}$ were estimated and used to calculate the biotite chemical formulas in atoms per formula unit (apfu). Selected biotite samples were further subjected to ^{57}Fe Mössbauer spectroscopy to define the fraction of Fe^{3+} and Fe^{2+} and their distribution over the M and T sites (Fig. S1, Table S2: Aspiotis et al., 2022). For serpentine and talc, a conventional charge-balance approach has been applied by assuming that the anionic site in the crystal structure of serpentine and talc is occupied by a total of 4 and 2 apfu, respectively, without any vacancies at the anionic site.

However, EMPA cannot directly measure the real cation partitioning at different crystallographic sites. Raman spectroscopy has already been proven to have the great potential for the determination of the exact elemental distribution within each single mineral-phase given that vibrational phonon modes are both sensitive to chemistry and structure (e.g. Leissner et al., 2015; Hawthorne, 2016; Watenphul et al., 2016a, b; Waesermann et al., 2020). This characteristic is significant in studying solid solutions, for instance biotites, where different types of atoms can enter the same crystallographic site, but also in other Mg-dominant phyllosilicates without interlayer cation, i.e. serpentines and talc, where incorporation of R^{2+} and R^{3+} cations (Fe^{2+} , Fe^{3+} and Al^{3+}), can mostly be observed at the octahedral site (Petit et al., 2004; Corona et al., 2015; Balan et al., 2021b).

Given that the largest chemical variations occurs at the octahedral sites of these layered silicates, there are two possibilities for the quantification of the major elements occupying the M -site: (a) directly, by analyzing the octahedral MO_6 vibrations (see spectral range I of Fig. 4: Aspiotis et al., 2022) and (b) indirectly, by studying the influence of the M -site cations and MMM local configurations on the TO_4 -ring mode vibrations (see spectral range II of Fig. 4: Aspiotis et al., 2022) and OH-stretching phonon modes (see spectral range IV of Fig. 4: Aspiotis et al., 2022), respectively. In particular, the different chemical surroundings may lead to one-mode or two-mode behavior. In the former case only one peak is observed in the mixed (e.g. $^M(\text{Mg}_{3-x}\text{Fe}_x)$) compound, whose position ω depends on the concentration x (Chang and Mitra, 1971), whereas in the latter case more Raman peaks than those predicted by group-theory analysis can appear in the spectrum of a solid solution, whose fractional intensities correlate with the composition x . Thus, site-group theory analysis is obligatory to clarify the exact number of the expected phonon modes for all atoms, including H.

According to group-theory considerations, the expected Raman-active phonon modes for biotite, lizardite and talc are 30 for each mineral, whilst for chrysotile and antigorite they are 105 and 870, respectively (Table 3.b.1). It should be noted that the group-theory analysis of antigorite is based on the modulated structure of an antigorite polysome $\text{M}_{3m-3}\text{T}_{2m}\text{O}_{5m}(\text{OH})_{4m-6}$ with $m = 17$ (Capitani and Mellini, 2004).

Table 3.b.1: Group-theory analysis for biotite, lizardite and talc according to Kroumova et al. (2003).

Mineral	Symmetry	General formula	Total Raman-active modes	Raman-active OH-stretching vibrations
Biotite	Monoclinic $C2/m$	$\text{K}(\text{Mg}_{3-x}\text{Fe}_x^{2+})(\text{AlSi}_3)\text{O}_{10}(\text{OH},\text{F})_2$	$16 A_g + 14 B_g$	$1 A_g$
Lizardite	Trigonal $P31m$	$\text{Mg}_3\text{Si}_2\text{O}_5(\text{OH})_4$	$12 A_1 + 18 E$	$2 A_1 + E$
Chrysotile	Monoclinic Cc	$\text{Mg}_3\text{Si}_2\text{O}_5(\text{OH})_4$	$52A' + 53A''$	$4A' + 4A''$
Antigorite	Monoclinic Pm	$\text{Mg}_3\text{Si}_2\text{O}_5(\text{OH})_4$	$483A' + 387A''$	$47A' + 15A''$
Talc	Triclinic $P\bar{1}$	$\text{Mg}_3\text{Si}_4\text{O}_{10}(\text{OH})_2$	$30 A_g$	$1 A_g$

Table 3.b.1 reveals that H atoms generate only one A_g mode in the case of biotite (see also Table 2: Aspiotis et al., 2022) and talc (Aspiotis et al., *submitted*), which corresponds, upon considering the directions of the atomic vector displacements via the Bilbao Crystallographic server (Kroumova et al., 2003), to the OH-stretching vibration perpendicular to the (001) plane (see Fig. 1: Aspiotis et al., 2022). In the case of lizardite, $2 A_1$ and E phonon modes are related to the OH-stretching vibration that can be further divided into (i) the inner OH groups, bonded to an octahedrally coordinated cationic MMM triplet, vibrating perpendicular to the M -layer and pointing towards the center of the quasi-two-dimensional

system of six-membered TO_4 rings and (ii) the interlayer OH groups which are located on the top of the octahedral layer and are H-bonded, pointing towards the O atoms of the basal plane of the adjacent $Ts\text{-Os}$ sequence (Fig. 3.b.1). Therefore, the presence of more than one Raman peaks in the OH-stretching region of biotite and talc implies a chemical deviation from the endmember composition and the existence of diverse M -site cations surrounding the OH groups. Hence, two-mode behavior of the O-H bond stretching can be applied for the crystallochemical analysis of the M -site of these phyllosilicates.

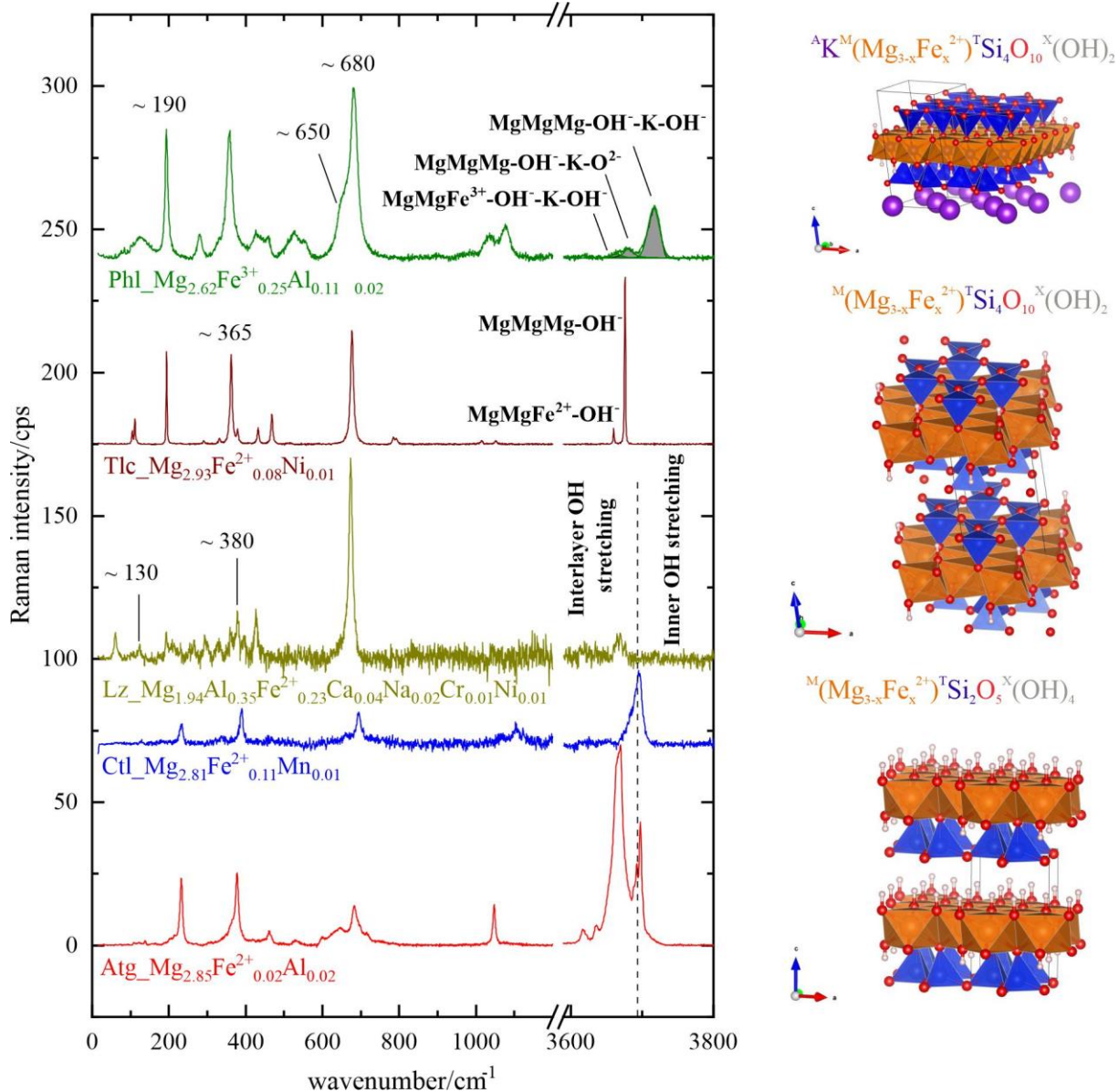


Figure 3.b.1: Raman spectra of selected samples from the studied mineral groups of layered silicates, where only the composition of the M -site is given. Mineral abbreviations (Whitney and Evans, 2010): Atg: antigorite; Ctl: chrysotile; Lz: lizardite; Phl: phlogopite; and Tlc: talc. The atomic fragments on the right represent the structure

of biotite (top), talc (middle), serpentine (bottom); VESTA software package (Momma and Izumi, 2008) was used to plot the atomic structure.

In the case of serpentines, this approach is not applicable, since the effect of structural differences among the serpentine-group minerals is stronger than that of chemistry (Fig. 3.b.1). Therefore, the assignment of the OH-stretching peaks to specific *MMM* triplets is hindered by: (a) the layer curvature in antigorite, as an effect of diverse O-H bond lengths changing along the modulated structure (Capitani and Mellini, 2004; Balan et al., 2021a), (b) possible splitting between transverse optical (TO) and longitudinal optical (LO) phonon modes (Prencipe et al., 2009; Compagnoni et al., 2021; Balan et al., 2021b), (c) perturbation of the tetrahedral and octahedral layers caused by substitutions (Libowitzky, 1999; Balan et al., 2021b), and (d) the H \cdots O bond geometry, since a bent O-H \cdots O bridge will upshift the OH-stretching vibrations by $\sim 70\text{ cm}^{-1}$ compared to a straight O-H \cdots O (Libowitzky, 1999). However, the Raman spectral patterns of the OH-stretching region (see Fig. 3.b.1) can be used as a tool to distinguish the serpentine-group minerals.

Thus, the introduction of a second vibrational group, i.e. framework vibrations, sensitive to the *M*-site and *T*-site chemistry is mandatory to solve this issue. Moreover, the crosschecking of the calculations gained from the two-mode behavior of the OH-stretching vibrations and those of the framework vibrations, for example ^MMg , $^M\text{Fe}^{2+}$ and $^M\text{Fe}^{3+}$ contents in biotite (Fig.5, 6: Aspiotis et al., 2022), will reduce the uncertainties and give an unequivocal determination of the major elements occupying the *M*-sites. It should be noted that minor elements, such as Ti in biotite, cannot be quantified from the OH-stretching vibrations, as the peak positions of Ti-containing *MMM* triplets may coincide with other already assigned local configurations, resulting only to the broadening of the corresponding peaks.

As a result, the established calibration curves between the Raman signals and the chemical composition of the analysed biotites derived from EMP analyses and Mössbauer spectroscopic data provide a preparation-free, fast, and easy-to-handle tool for the crystallochemical characterization of those phyllosilicates. In particular:

- By following the recommended OH-stretching peak assignment to different local cationic arrangements (Table 3: Aspiotis et al., 2022), $^M\text{Mg}_{\text{Raman (aver.)}}$, $^M\text{Fe}^{2+}_{\text{Raman (aver.)}}$, and $^M(\text{Fe}^{2+}+\text{Fe}^{3+})_{\text{Raman (aver.)}}$ can be calculated (Fig. 5c, d and 6b,c: Aspiotis et al., 2022) with relative uncertainties of ~ 6 , 6, and 8%, respectively.

-
- Deviations from the one-to-one correlation lines, in the case of estimating the ${}^M\text{Fe}^{2+}$ and ${}^M\text{Fe}^{3+}$ amounts, demonstrate incorporation of non-(Mg, Fe) cations in the octahedral layer (Fig. 6d: Aspiotis et al., 2022).
 - The amount of *M*-site Mg, Fe^{2+} , and Fe^{3+} can be cross-checked by the position of the strong Raman peak near 190 cm^{-1} , typical of MO_6 vibrations; FWHM_{190} can be used as well for the quantification of ${}^M\text{Mg}$.
 - ${}^M\text{Ti}$ content can be estimated by ω and FWHM of the TO_4 -ring mode at $\sim 680\text{ cm}^{-1}$ (Fig. 7c-f: Aspiotis et al., 2022). It is recommended to use the ${}^M\text{Ti}(\text{FWHM}_{680})$ trend, if two peaks near 650 and 680 cm^{-1} can be resolved as the relative uncertainties are $\sim 20\%$.
 - The presence of ${}^M\text{Al} > 0.8$ apfu in annite can be detected by cross-checking the ${}^M\text{Mg}$ contents derived from ω_{190} and of the integrated intensities of the OH-stretching peaks.
 - The amount of ${}^T\text{Si}$ can be monitored using the peak position of the TO_4 -ring modes at $\sim 650\text{ cm}^{-1}$ with relative uncertainties of 3% (Fig. 7a, b: Aspiotis et al., 2022). ${}^T\text{Al}$ content of phlogopite can indirectly be extracted by ${}^T\text{Al} = 4 - {}^T\text{Si}$.
 - Potassium content in the interlayer space of phlogopites can be quantified from ω_{730} with relative uncertainties of 3% (Fig. 8: Aspiotis et al., 2022), whereas interlayer-deficient annite can be recognized by the position of the strongest OH-stretching mode, appearing at 3570 instead of $\sim 3650\text{ cm}^{-1}$.

For serpentine-group minerals and talc, the same methodological approach for the non-destructive estimation of their crystal chemistry has been followed. Particularly in talc, the fractional intensities of the Raman peaks of the OH-stretching vibrations have been used to quantify ${}^M\text{Mg}$ and ${}^M(\text{Fe}^{2+}+\text{Mn})$ contents (Fig. 3.b.2) and the data points follow an one-to-one correlation line, which is fully compatible with the reported quantification of ${}^M\text{Mg}$ and ${}^M\text{Fe}^{2+}$ based on FTIR data (Petit et al., 2004). Moreover, it is evident that the accuracy obtained from the Raman spectroscopic analysis is as good as by EMPA, though the separation of Raman peaks, which can exclusively be assigned to Mn- and Fe-containing *MMM* triplets, is not feasible. The reason for that, as has been already reported for tourmalines (Watenphul et al., 2016a), is the almost identical mass and ionic radii of those two octahedrally coordinated cations, which results in similar Raman peak positions of the associated local configurations.

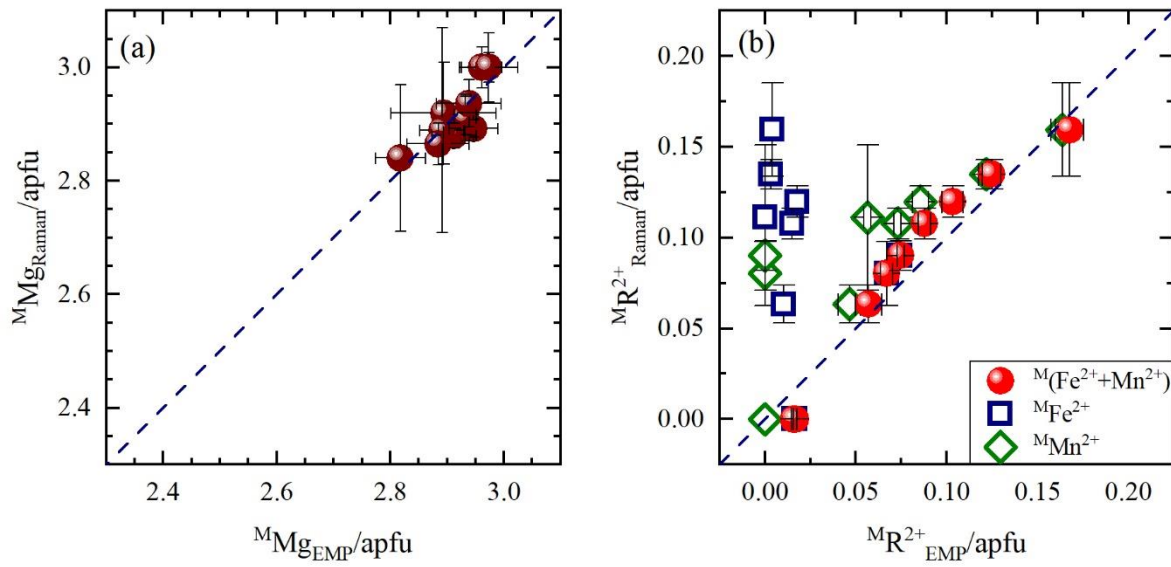


Figure 3.b.2: (a) ${}^M\text{Mg}$ content in talc derived from EMP analysis (${}^M\text{Mg}_{\text{EMP}}$) plotted against ${}^M\text{Mg}$ content from the Raman spectroscopic analysis (${}^M\text{Mg}_{\text{Raman}}$) of the OH-stretching region and (b) ${}^M\text{R}^{2+}$ amount calculated from EMPA (${}^M\text{R}^{2+}_{\text{EMP}}$) vs. that quantified from the Raman spectroscopic analysis (${}^M\text{R}^{2+}_{\text{Raman}}$) of the OH-stretching vibrations, where $\text{R} = \text{Fe}, \text{Mn}, \text{or } (\text{Fe}+\text{Mn})$.

Interestingly, the FWHM of the Raman peak around 380 cm^{-1} (FWHM_{380}) in serpentines, associated with MO_6 vibrations (Prencipe et al., 2009), was proven to be the most sensitive spectral parameter to ${}^M\text{Mg}$ amount (Fig. 3.b.3a), regardless of the serpentine polymorph/variety. Thus, FWHM_{380} can be promoted as a reliable spectral parameter to quantify ${}^M\text{Mg}$ amount, which is in line with the fact that FWHM of a phonon peak is generally sensitive to substitutional disorder (Petit et al., 2004). Thus, after assigning each analyzed sample to one of the four types of serpentine minerals (polyhedral serpentine has not been identified in any of the samples examined) the following equations can be used to estimate the content of ${}^M\text{Mg}$ in each of the serpentine polymorphs/variety:

- Antigorite (black line in Fig. 3.b.3a): $\text{FWHM}_{380} = (2.06 \pm 0.06) + (0.152 \pm 0.005) {}^M\text{Mg}_{\text{Atg}} - 0.008 ({}^M\text{Mg}_{\text{Atg}})^2$.
- Lizardite-dominant PS and lizardite (red line in Fig. 3.b.3a): $\text{FWHM}_{380} = (3.77 \pm 0.05) - 0.088 {}^M\text{Mg}_{\text{Lz}}$.
- Chrysotile-dominant PS (blue line in Fig. 3.b.3a): $\text{FWHM}_{380} = (3.10 \pm 0.03) - 0.023 {}^M\text{Mg}_{\text{Ctl-PS}}$.

- Chrysotile (brown line in Fig. 3.b.3a): $\text{FWHM}_{380} = (2.96 \pm 0.01) - (0.030 \pm 0.001)^M \text{Mg}_{\text{Ctl}}$.

The resulting plot between the amount of ^MMg calculated from the Raman spectroscopic analysis against that from EMPA (Fig. 3.b.3b), provided a one-to-one correlation line with relative uncertainties that do not exceed 5%. Similarly, the FWHM of the strongest Raman-active phonon mode of the octahedral vibrations near 230 cm^{-1} (FWHM_{230}), exhibits a linear correlation with $^M\text{Fe}^{2+}$ in the crystal structures of chrysotile-dominant PS and chrysotile (Fig. 3.b.3c). As can be seen in Fig. 3.b.3d, a one-to-one correlation for all values between 0.02 and 0.15 apfu with relative errors of $\sim 5\%$, is noted.

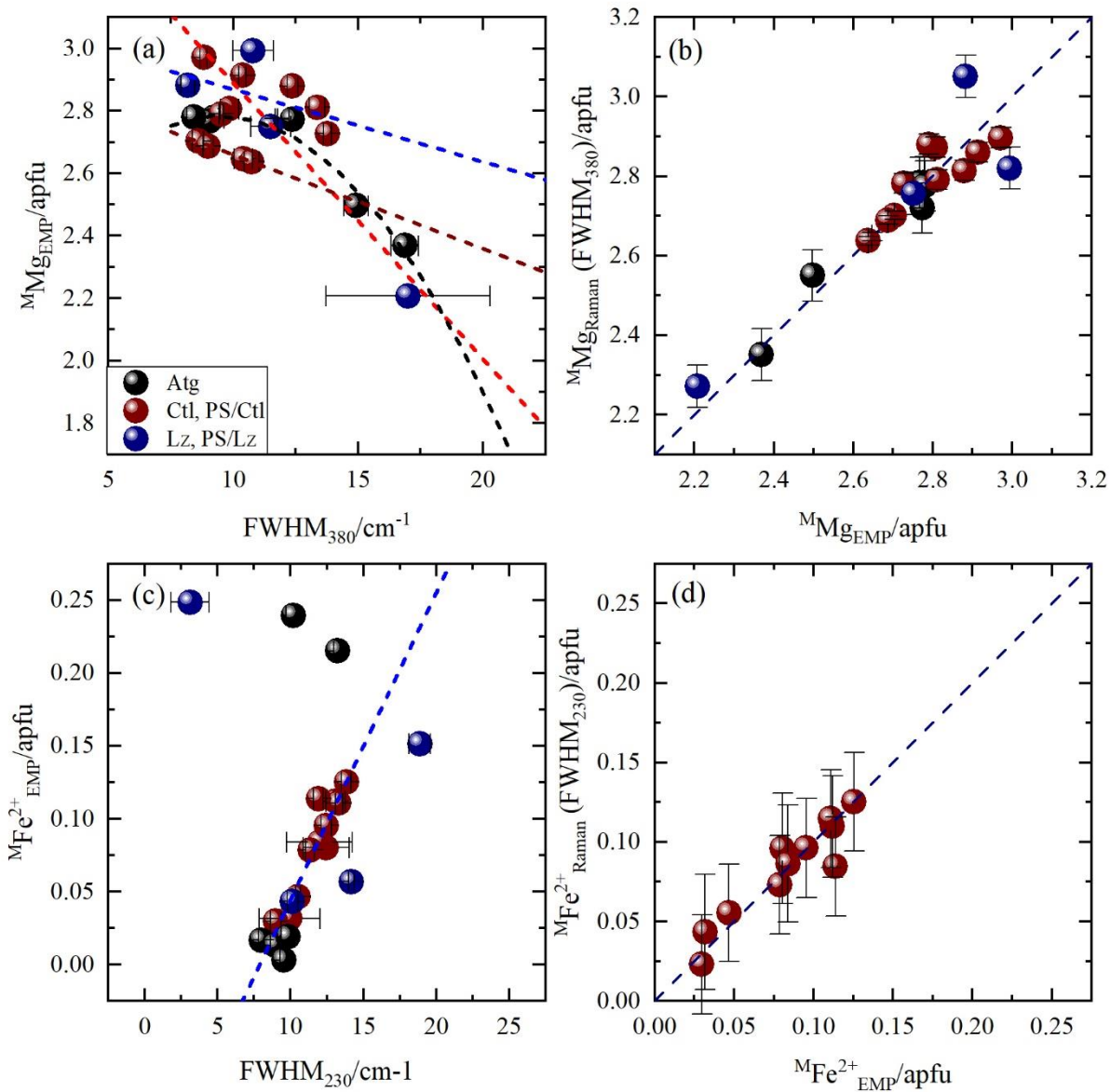


Figure 3.b.3: Quantification of M-site Mg and Fe^{2+} in serpentine polymorphs/varieties according to the MO_6 vibrations at 380 and 230 cm^{-1} : (a) $^M\text{Mg}^+$ content plotted against FWHM_{380} and (b) ^MMg amount of each serpentine

polymorph calculated from the Raman spectroscopic analysis (${}^M\text{Mg}_{\text{Raman}}$) of the MO_6 vibrations at 380 cm^{-1} against that determined by EMPA (${}^M\text{Mg}_{\text{EMPA}}$), (c) ${}^M\text{Fe}^{2+}$ amount vs. FWHM_{230} in chrysotile-dominant PS and chrysotile, and (d) ${}^M\text{Fe}^{2+}$ amount for chrysotile-like PS and chrysotile obtained from the Raman spectroscopic analysis (${}^M\text{Fe}^{2+}_{\text{Raman}}$) of FWHM_{230} vs. that calculated from EMPA (${}^M\text{Fe}^{2+}_{\text{EMPA}}$).

4. Outline and future research

Overall, the outcomes of this study provide a conceivable way for uncovering hardly readable or completely vanished inscribed text on rock-based written artefacts via the incorporation of weathering-related products or foreign material, whose nature and propagation is influenced by different inscription ages, local climate and urbanization of the area, grain size, and letter colouring. Further work, based on Raman spectroscopy and newly developed methods such as micro-spatially offset Raman spectroscopy (μ -SORS) that can non-destructively probe subsurface layers even on rock-based writing supports (e.g. Realini et al., 2016, 2017), is of highly importance to understand the conservation history and evolution of a cultural-heritage object in time.

Moreover, our study on complex trioctahedral layered silicates with filled, i.e. biotites, and empty, i.e. serpentine-group minerals and talc, interlayer space, shows that Raman spectroscopy is a reliable analytical method for the crystallochemical characterization of these phyllosilicates. The truly non-destructive nature of Raman spectroscopy makes it an extremely useful tool, not only in Geosciences, but also in characterizing cultural-heritage objects, comprised of layered silicates, as the trends provided here demonstrate that they can be used even for quantitative analyses. It is highly anticipated that a similar analytical approach to other groups of phyllosilicates, such as smectites, will facilitate the non-invasive determination of their crystallochemical composition.

The application of non-destructive analytical methods can bridge the gap between natural sciences and cultural heritage since both disciplines have more things in common than differences. The only secure practice for further achievements is combining forces, which will certainly help us to obtain better results.

Acknowledgements

The research for this study was funded by the Deutsche Forschungsgemeinschaft (DFG, German Research Foundation) under Germany's Excellence Strategy – EXC 2176 “Understanding Written Artefacts: Material, Interaction and Transmission in Manuscript Cultures”, project no. 390893796. The research was conducted within the scope of the Centre for the Study of Manuscript Cultures (CSMC) at Universität Hamburg. I thank Stefanie Heidrich and Peter Stutz, Universität Hamburg, for help with WD-EMPA measurements and sample preparation, as well as Joachim Ludwig and Leonie Tipp for partial help with XRD and Raman measurements, respectively. I am very grateful to the administration and employees of the cemetery of Ohlsdorf for kindly providing the marble gravestones. The Mineralogical Museum, at Universität Hamburg is greatly acknowledged for kindly providing us the series of the studied phyllosilicates.

I would personally like to thank my supervisors Prof. Dr. Boriana Mihailova and Prof. Dr. Jochen Schlüter for their great support and patience throughout my Ph.D. studies and their guidance of how to overcome obstacles that can emerge.

Last but not least, I would like to thank my colleagues at the Mineralogisch-Petrographisches Institute and in the Graduate School of CSMC for all the fruitful discussions and support during my studies. Yet even more importantly, my greatest thanks to my family and friends that have supported me through this wonderful journey.

References

- Andréani, M., Grauby, O., Baronnet, A., and Muñoz, M.: Occurrence, composition and growth of polyhedral serpentine. *Eur. J. Mineral.*, 20, 159-171, 2008.
- Artioli, G. (Eds.): *Scientific methods and cultural heritage*. Oxford University Press Inc., New York, 2010.
- Aspiotis, S., Schlüter, J., Harter-Uibopuu, K., and Mihailova, B.: Crack-enhanced weathering in inscribed marble: a possible application in epigraphy. *Eur. J. Mineral.*, 33, 189-202, 2021b.
- Aspiotis, S., Schlüter, J., Redhammer, G.J., and Mihailova, B.: Non-destructive determination of the biotite crystal chemistry using Raman spectroscopy: how far we can go? *Eur. J. Mineral.*, 34, 573-590, 2022.
- Auzende, A.-L., Daniel, I., Reynard, B., Lemaire, C., and Guyot, F.: High-pressure behaviour of serpentine minerals: a Raman spectroscopic study. *Phys. Chem. Minerals*, 31, 269-277, 2004.
- Balan, E., Delattre, S., Roche, D., Segalen, L., Morin, G., Guillaumet, M., Blanchard, M., Lazzeri, M., Brouder, C., and Salje, E.K.H.: Line-broadening effects in the powder infrared spectrum of apatite. *Phys. Chem. Minerals*, 38, 111-122, 2011.
- Balan, E., Fritsch, E., Radtke, G., Paulatto, L., Juillot, F., and Petit, S.: First-principles modeling of the infrared spectrum of antigorite. *Eur. J. Mineral.*, 33, 389-400, 2021a.
- Balan, E., Fritsch, E., Radtke, G., Paulatto, L., Juillot, F., Baron, F., and Petit, S.: First-principles modeling of the infrared spectrum of Fe- and Al-bearing lizardite. *Eur. J. Mineral.*, 33, 647-657, 2021b.
- Baronnet, A. and Devouard, B.: Topology and crystal growth of natural chrysotile and polygonal serpentine. *J. Cryst. Growth*, 166, 952-960, 1996.
- Baronnet, A., Andréani, M., Grauby, O., Devouard, B., Nitsche, S., and Chaudanson, D.: Onion morphology and microstructure of polygonal serpentine. *Am. Mineral.*, 92, 687-690, 2007.
- Bendel, V. and Schmidt, B.C.: Raman spectroscopic characterisation of disordered alkali feldspars along the join KAlSi_3O_8 - $\text{NaAlSi}_3\text{O}_8$: application to natural sanidine and anorthoclase. *Eur. J. Mineral.*, 20, 1055-1065, 2008.
- Bersani, D. and Lottici, P.P.: Raman spectroscopy of minerals and mineral pigments in archaeometry. *J. Raman Spectrosc.*, 47, 499-530, 2016.
- Bishop, J.L., Lane, M.D., Dyar, M.D., King, S.J., Brown, A.J., and Swayze, G.A.: Spectral properties of Ca-sulfates: Gypsum, basanite, and anhydrite. *Am. Mineral.*, 99, 2105-2115, 2014.

- Capitani, G. and Mellini, M.: The modulated structure of antigorite: the $m = 17$ polysome. *Am. Mineral.*, 89, 147-158, 2004.
- Chang, I.F. and Mitra, S.S.: Long wavelength optical phonons in mixed crystals. *Adv. Phys.*, 20, 359-404, 1971.
- Coates, J.: Interpretation of infrared spectra, a practical approach, in: *Encyclopedia of Analytical Chemistry*, edited by Meyers, R.A., John Wiley & Sons Ltd, Chichester, 10815-10837, 2000.
- Compagnoni, R., Cossio, R., and Mellini, M.: Raman anisotropy in serpentine minerals, with a *caveat* on identification. *J. Raman Spectrosc.*, 52, 1334-1345, 2021.
- Cooke, R.U., Inkpen, R.J., and Wiggs, G.F.S.: Using gravestones to assess changing rates of weathering in the United Kingdom. *Earth Surf. Process. Landf.*, 20, 531-546, 1995.
- Corona, J.C., Jenkins, D.M., and Dyar, M.D.: The experimental incorporation of Fe into talc: a study using X-ray diffraction, Fourier-transform infrared spectroscopy, and Mössbauer spectroscopy. *Contrib. Mineral. Petrol.*, 170, 29, 2015.
- Corradini, M., de Ferri, L., and Pojana, G.: Spectroscopic characterization of commercial pigments for pictorial retouching. *J. Raman Spectrosc.*, 52, 35-58, 2021.
- Dragovich, D.: Marble weathering in an industrial environment, Eastern Australia. *Environ. Geol. Water Sci.*, 17, 127-132, 1991.
- Edwards, H.G.M., Farwell, D.W., and Seaward, M.R.D.: Raman spectra of oxalates in lichen encrustations on Renaissance frescoes. *Spectrochim. Acta A*, 47, 1531-1539, 1991.
- Edwards, H.G.M., Seaward, M.R.D., Attwood, S.J., Little, S.J., de Oliveira, L.F.C., and Tretiach, M.: FT-Raman spectroscopy of lichens on dolomitic rocks: an assessment of metal oxalate formation. *Analyst*, 128, 1218-1221, 2003.
- Edwards, H.G.M., Colomban, P., and Bowden, B.: Raman spectroscopic analysis of an English soft-paste porcelain plaque-mounted table. *J. Raman Spectrosc.*, 35, 656-661, 2004.
- El Halim, M., Daoudi, L., El Ouahabi, M., Rousseau, V., Cools, C., and Fagel, N.: Mineralogical and geochemical characterization of archaeological ceramics from the 16th century El Badi Palace, Morocco. *Clay Miner.*, 53, 459-470, 2018.
- Engling, G. and Gelencsér, A.: Atmospheric brown clouds: from local air pollution to climate change. *Elements*, 6, 223-228, 2010.
- Ferrari, A.C. and Robertson, J.: Raman spectroscopy of amorphous, nanostructured, diamond-like carbon, and nanodiamond. *Phil. Trans. R. Soc. Lond. A*, 362, 2477-2512, 2004.

- Fritsch, E., Balan, E., Petit, S., and Juillot, F.: Structural, textural, and chemical controls on the OH stretching vibrations in serpentine-group minerals. *Eur. J. Mineral.*, 33, 447-462, 2021.
- Frost, R.L. and Weier, M.L.: Raman spectroscopy of natural oxalates at 298 and 77K. *J. Raman Spectrosc.*, 34, 776-785, 2003.
- Frost, R.L.: Raman spectroscopy of natural oxalates. *Anal. Chim. Acta*, 517, 207-214, 2004.
- Fuchs, Y., Linares, J., and Mellini, M.: Mössbauer and infrared spectrometry of lizardite-1T from Monte Fico, Elba. *Phys. Chem. Minerals*, 26, 111-115, 1998.
- Gadd, G.M.: Fungi, rocks, and minerals. *Elements*, 13, 171-176, 2017.
- Gatta, G.D., Merlini, M., Valdré, G., Liermann, H.-P., Nénert, G., Rothkirch, A., Kahlenberg, V., and Pavese, A.: On the crystal structure and compressional behavior of talc: a mineral of interest in petrology and material science. *Phys. Chem. Minerals*, 40, 145-156, 2013.
- Gieré, R. and Querol, X.: Solid particulate matter in the Atmosphere. *Elements*, 6, 215-222, 2010.
- Grobéty, B., Gieré, R., Dietze, V., and Stille, P.: Airborne particles in the urban environment. *Elements*, 6, 229-234, 2010.
- Hawthorne, F.C.: Short-range atomic arrangements in minerals. I: The minerals of the amphibole, tourmaline and pyroxene supergroups. *Eur. J. Mineral.*, 28, 513-536, 2016.
- Holder, J.M., Wynn-Williams, D.D., Rull Perez, F., and Edwards, H.G.M.: Raman spectroscopy of pigments and oxalates in situ within epilithic lichens: *Acaroscopy* from the Antarctic and Mediterranean. *New Phytol.*, 145, 271-280, 2000.
- Hradil, D., Píšková, A., Hradilová, J., Bezdička, P., Lehrberger, G., and Gerzer, S.: Mineralogy of Bohemian green earth pigment and its microanalytical evidence in historical paintings. *Archaeometry*, 53, 563-586, 2011.
- Huang, E., Chen, C.H., Huang, T., Lin, E.H., and Xu, J.-A.: Raman spectroscopic characteristics of Mg-Fe-Ca pyroxenes. *Am. Mineral.*, 85, 473-479, 2000.
- Jegova, G., Titorenkova, R., Rashkova, M., Mihailova, B.: Raman and IR reflection micro-spectroscopic study of Er:YAG laser treated permanent and deciduous human teeth. *J. Raman Spectrosc.*, 44, 1483-1490, 2013.
- Košářová, V., Hradil, D., Němec, I., Bezdička, P., and Kanický, V.: Microanalysis of clay-based pigments in painted artworks by the means of Raman spectroscopy. *J. Raman Spectrosc.*, 44, 1570-1577, 2013.

- Kroumova, E., Aroyo, M.I., Perez-Mato, J.M., Kirov, A., Capillas, C., Ivantchev, S., and Wondratschek, H.: Bilbao 554 Crystallographic Server: useful databases and tools for phase-transition studies. *Ph. Transit.*, 76, 155-170, 2003.
- Leissner, L., Schlüter, J., Horn, I., and Mihailova, B.: Exploring the potential of Raman spectroscopy for crystallochemical analyses of complex hydrous silicates: I. Amphiboles. *Am. Mineral.*, 100, 2682-2694, 2015.
- Li, X., Zhang, C., Behrens, H., and Holtz, F.: Calculating amphibole formula from electron microprobe analysis data using a machine learning method based on principal components regression. *Lithos*, 362-363, 105469, 2020.
- Libowitzky, E.: Correlation of O-H stretching frequencies and O-H...O hydrogen bond lengths in minerals. *Monatsh. Chem.*, 130, 1047-1059, 1999.
- Litasov, K.D. and Podgornykh N.M.: Raman spectroscopy of various phosphate minerals and occurrence of tuite in the Elga IIE iron meteorite. *J. Raman Spectrosc.*, 48, 1518-1527, 2017.
- Markovic, M., Fowler, B.O., Tung, M.S.: Preparation and comprehensive characterization of a calcium hydroxyapatite reference material. *J. Res. Natl. Inst. Stand. Technol.*, 109, 553-568, 2004.
- McKeown, D.A., Bell, M.I., and Etz, E.S.: Raman spectra and vibrational analysis of the trioctahedral mica phlogopite. *Am. Mineral.*, 84, 970-976, 1999.
- Michel, C.: What about 3D manuscripts? The case of cuneiform clay tablets, in: *Exploring written artefacts: Objects, methods and concepts*, edited by Quenzer, J.B., De Gruyter, Berlin, Boston, 89-114, 2021.
- Mihailova, B., Schlüter, J., and Harter-Uibopuu, K.: Inscribed gems: Material profiling beyond visible examination, in: *Exploring written artefacts: Objects, methods and concepts*, edited by Quenzer, J.B., De Gruyter, Berlin, Boston, 229-244, 2021.
- Momma, K. and Izumi, F.: VESTA: a three-dimensional visualization system for electronic and structural analysis. *J. Appl. Crystallogr.*, 41, 653-658, 2008.
- Moropoulou, A., Bisbikou, K., Torfs, K., Van Grieken, R., Zezza, F., and Macri, F.: Origin and growth of weathering crusts on ancient marbles in industrial atmosphere. *Atmos. Environ.*, 32, 967-982, 1998.
- Petit, S., Martin, F., Wiewiora, A., De Parseval, P., and Decarreau, A.: Crystal-chemistry of talc: a near infrared (IR) spectroscopy study. *Am. Mineral.*, 89, 319-326, 2004.
- Pinna, D., Galeotti, M., and Rizzo, A.: Brownish alterations on the marble statues in the church of Orsanmichele in Florence; what is their origin? *Herit. Sci.*, 3, 7, 2015.

- Powers, J., Clinton, N.D., Huang, R., Smilgies, D.M., Bilderback, D., Clinton, K., and Thorne, R.E.: X-ray fluorescence recovers writing from ancient inscriptions. *Z. Papyr. Epigr.*, 152, 221-227, 2005.
- Prasad, P.S.R., Pradhan, A., and Gowd, T.N.: In situ micro-Raman investigation of dehydration mechanism in natural gypsum. *Curr. Sci.*, 80, 1203-1207, 2001.
- Prencipe, M., Noel, Y., Bruno, M., and Dovesi, R.: The vibrational spectrum of lizardite-1T [Mg₃Si₂O₅(OH)₄] at the Γ point: A contribution from an ab initio periodic B3LYP calculation. *Am. Mineral.*, 94, 986-994, 2009.
- Prencipe, M., Mantovani, L., Tribaudino, M., Bersani, D., and Lottici, P.P.: The Raman spectrum of diopside: a comparison between ab initio calculated and experimentally measured frequencies. *Eur. J. Mineral.*, 24, 457-464, 2012.
- Realini, M., Botteon, A., Conti, C., Colombo, C., Matousek, P.: Development of portable defocusing micro-scale spatially offset Raman spectroscopy. *Analyst*, 141, 3012-3019, 2016.
- Realini, M., Conti, C., Botteon, A., Colombo, C., Matousek, P.: Development of a full micro-scale spatially offset Raman spectroscopy prototype as a portable analytical tool. *Analyst*, 142, 351-355, 2017.
- Redhammer, G.J., Beran, A., Schneider, J., Amthauer, G., and Lottermoser, W.: Spectroscopic and structural properties of synthetic micas on the annite-siderophyllite binary: Synthesis, crystal structure refinement, Mössbauer, and infrared spectroscopy. *Am. Mineral.*, 85, 449-465, 2000.
- Redhammer, G.J., Amthauer, G., Lottermoser, W., and Roth, G.: Quadrupole splitting distribution of Fe²⁺ in synthetic trioctahedral micas. *Hyperfine Interact.*, 141/142, 345-349, 2002.
- Sahoo, S., Arora, A. K., and Sridharan V.: Raman line shapes of optical phonons of different symmetries in anatase TiO₂ nanocrystals. *J. Phys. Chem. C*, 113, 16927–16933, 2009.
- Saikia, B.J., Parthasarathy, G., and Sarmah, N.C.: Fourier transform infrared spectroscopic estimation of crystallinity in SiO₂ based rocks. *Bull. Mater. Sci.*, 31, 775-779, 2008.
- Scordari, F., Ventruti, G., Sabato, A., Bellatreccia, F., Della Ventura, G., and Pedrazzi, G.: Ti-rich phlogopite from Mt. Vulture (Potenza, Italy) investigated by a multianalytical approach: Substitutional mechanisms and orientation of the OH dipoles. *Eur. J. Mineral.*, 18, 379-391, 2006.
- Scordari, F., Schingaro, E., Lacalamita, M., and Mesto, E.: Crystal chemistry of trioctahedral micas-2M1 from Bunyaruguru kamafugite (southwest Uganda). *Am. Mineral.*, 97, 430-439, 2012.

- Scordari, F., Schingaro, E., Ventruti, G., Nicotra, E., Viccaro, M., and Mazziotti Tagliani, S.: Fluorophlogopite from Piano delle Concazze (Mt. Etna, Italy): Crystal chemistry and implications for the crystallization conditions. *Am. Mineral.*, 98, 1017-1025, 2013.
- Singha, M. and Singh, L.: Vibrational spectroscopic study of muscovite and biotite layered phyllosilicates. *Indian J. Pure Appl. Phys.*, 54, 116-122, 2016.
- Środoń, J.: Use of clay minerals in reconstructing geological processes: recent advances and some perspectives. *Clay Miner.*, 34, 27-37, 1999.
- Takahashi, H., Maehara, I., and Kaneko, N.: Infrared reflection spectra of gypsum. *Spectrochim. Acta A*, 39, 449-455, 1983.
- Tarling, M.S., Rooney, J.S., Viti, C., Smith, S.A.F., Gordon, K.C.: Distinguishing the Raman spectrum of polygonal serpentine. *J. Raman Spectrosc.*, 49, 1978-1984, 2018.
- Tlili, A., Smith, D.C., Beny, J.-M., and Boyer, H.: A Raman microprobe study of natural micas. *Mineral. Mag.*, 53, 165-179, 611 1989.
- Twilley, J.: Raman spectroscopy investigations of the weathering alteration of a predazzite marble mouflon of the Indus Valley Culture. *J. Raman Spectrosc.*, 37, 1201-1210, 2006.
- Uehara, S. and Shirozu, H.: Variations in chemical composition and structural properties of antigorites. *Mineral. Journal*, 12, 299-318, 1985.
- Waeselmann, N., Schlüter, J., Malcherek, T., Della Ventura, G., Oberti, R., and Mihailova, B.: Nondestructive determination of the amphibole crystal-chemical formulae by Raman spectroscopy: One step closer. *J. Raman Spectrosc.*, 51, 1530-1548, 2020.
- Wang, A., Freeman, J.J., and Jolliff, B.L.: Understanding the Raman spectral features of phyllosilicates. *J. Raman Spectrosc.*, 623 46, 829-845, 2015.
- Wang, Y.Y., Gan, F.X., and Zhao, H.X.: Inclusions of black-green serpentine jade determined by Raman spectroscopy. *Vib. Spectrosc.*, 66, 19-23, 2013.
- Watenphul, A., Burgdorf, M., Schlüter, J., Horn, I., Malcherek, T., and Mihailova, B.: Exploring the potential of Raman spectroscopy for crystallochemical analyses of complex hydrous silicates: II. Tourmalines. *Am. Mineral.*, 101, 970-985, 2016a.
- Watenphul, A., Schlüter, J., Bosi, F., Skogby, H., Malcherek, T., and Mihailova, B.: Influence of the octahedral cationic-site occupancies on the framework vibrations of Li-free tourmalines, with implications for estimating temperature and oxygen fugacity in host rocks. *Am. Mineral.*, 101, 2554-2563, 2016b.

- Wentzel, M., Gorzawski, H., Naumann, K-H., Saathoff, H., and Weinbruch, S.: Transmission electron microscopical and aerosol dynamical characterization of soot aerosols. *J. Aerosol Sci.*, 34, 1347-1370, 2003.
- Whitney, D.L. and Evans, B.W.: Abbreviations for names of rock-forming minerals. *Am. Mineral.*, 95, 185-187, 2010.
- Zazoff, P. (Eds.): *Die antiken Gemmen – Handbuch der Archäologie*, C.H. Beck'sche Verlagsbuchhandlung, Munich, Germany, 1983 (in German).
- Zhang, W.F., He, Y.L., Zhang, M.S., Yin, Z., and Chen, Q.: Raman scattering study on anatase TiO₂ nanocrystals. *J. Phys. D: Appl. Phys.*, 33, 912-916, 2000.

Appendix

A. Publications

A.a. List of publications related to the doctoral thesis

- I. Aspiotis, S., Schlüter, J., Harter-Uibopuu, K., and Mihailova B. (2021b). Crack-enhanced weathering in inscribed marble: a possible application in epigraphy. *European Journal of Mineralogy*, 33, 189-202. <https://doi.org/10.5194/ejm-33-189-2021>
- II. Aspiotis, S., Schlüter, J., Redhammer, G.J., and Mihailova, B.: Non-destructive determination of the biotite crystal chemistry using Raman spectroscopy: how far we can go? *European Journal of Mineralogy*, 34, 573-590. <https://doi.org/10.5194/ejm-34-573-2022>
- III. Aspiotis, S., Schlüter, J., and Mihailova, B.: Raman spectroscopy for crystallochemical analysis of Mg-rich 1:1 layer silicates: serpentine and talc. *Journal of Raman Spectroscopy*, *submitted*, JRS-23-0177.

A.b. Other publications

- I. Aspiotis, S., Jung, S., Hauff, F., and Romer, R.L. (2021a). Petrogenesis of a late-stage calc-alkaline granite in a giant S-type batholith – geochronology and Sr-Nd-Pb isotopes from the Nomatsaus granite (Donkerhoek batholith), Namibia. *International Journal of Earth Sciences*, 110, 1453-1476.

A.c. Contributions to conferences/workshops related to the doctoral thesis

- Aspiotis, S., Schlüter, J., and Mihailova, B.: Exploring Raman spectroscopy for crystallochemical analysis of biotite, 23rd General Meeting of the International Mineralogical Association, Lyon, France, 18-22 July, IMA2022-1353, 2022.
- Aspiotis, S., Schlüter, J., and Mihailova B. (2021). Estimating non-destructively the crystal chemistry of biotites by Raman spectroscopy. Oral presentation at the 3rd European Mineralogical Conference (EMC2020), Cracow, Poland.
- Aspiotis, S., Schlüter, J., Harter-Uibopuu, K., and Mihailova B. (2021). The decisive role of cracks for weathering of inscribed marble: application to epigraphy. Oral presentation at the 17th International Symposium on Experimental Mineralogy, Petrology and Geochemistry (EMPG-XVII), Potsdam, Germany.

- Aspiotis, S., Schlüter, J., Harter-Uibopuu, K., and Mihailova B. (2019). Crack-enhanced weathering in engraved marble: a possible application in epigraphy. Poster presentation at the Annual Conference of the DGGV and DMG (GeoMünster), Münster, Germany.

A.d. Other contributions to conferences/workshops

- Giotti, G., Bosch, S., Mohammed, H.A., and Aspiotis, S.: Palm-Leaf Manuscript Profiling Initiative (PLMPI) and the study of South Indian palm-leaf manuscripts, 34th Deutscher Orientalistentag, Berlin, Germany, 12-17 September, 2022.

B. Publication 1

B.a. Crack-enhanced weathering in inscribed marble: a possible application in epigraphy

Crack-enhanced weathering in inscribed marble: a possible application in epigraphy

Stylianos Aspiotis^{1,*}, Jochen Schlüter², Kaja Harter-Uibopuu³, Borianna Mihailova¹

¹ Fachbereich Erdsystemwissenschaften, Universität Hamburg, Grindelallee 48, 20146 Hamburg, email: stylianos.aspiotis@uni-hamburg.de, email: borianna.mihailova@uni-hamburg.de

² Mineralogisches Museum, CeNak, Universität Hamburg, Grindelallee 48, 20146 Hamburg, email: jochen.schlueter@uni-hamburg.de

³ Fachbereich Geschichte, Arbeitsbereich Alte Geschichte, Universität Hamburg, Überseering 35, 22297 Hamburg, email: kaja.harter@uni-hamburg.de

*Correspondence to: Stylianos Aspiotis (stylianos.aspiotis@uni-hamburg.de)

Abstract

Raman spectroscopy has been applied to check if there are detectible material differences beneath the inscribed and non-inscribed areas of marble-based written artefacts, which could be further used to visualize lost or hardly readable text via suitable mapping. As a case study, marble segments with ~2000-year-old inscribed letters from Asia Minor (western Turkey) and marble gravestones with 66 ± 14 -year-old inscriptions from the cemetery of Ohlsdorf (Hamburg, Germany) have been subjected to Raman spectroscopy as well as to complementary X-ray diffraction, wavelength-dispersive electron probe microanalysis, and Fourier-transform infrared spectroscopy to thoroughly study the effect of different environmental conditions, grain size, and inscription age on the nature and penetration depth of marble alteration. The results demonstrate that environmental conditions rule over the type of dominant weathering changes, which are carotenoid molecular inclusions produced by lichen and amorphous carbon for marbles from Hamburg and Asia Minor, respectively. The alteration is much stronger in medium- and coarse-grained than in fine-grained marble, but it is suppressed by letter colouring. In the absence of letter colouring, the weathering-related products in both ancient and modern engraved marbles are more abundant beneath than away from the engraved areas and the penetration depth is larger, due to the enhancement of fissures and micro-cracks around the inscribed areas. We show that the Raman intensity ratio between the strongest peak of the weathering-related product ($\nu(\text{C}=\text{C}) \sim 1520 \text{ cm}^{-1}$ for carotenoids or the G peak $\sim 1595 \text{ cm}^{-1}$ for soot-like carbon) and the strongest peak of marble (CO_3 stretching near 1087 cm^{-1}) can serve as a quantitative marker to indirectly map the lateral distribution of cracks induced during the inscribing process and hence, can potentially be used to trace lost text on vanished marble inscriptions. This approach can be applied to other rock types, but further studies are required to identify the corresponding autochthonous weathering-related products.

1 Introduction

Mineralogical analyses of rock-based writing supports are crucial to understand the roots of human civilization, since the written language, as a communicational expression, is the most widespread and secure practice of transmitting knowledge through time. In particular, inscribed rocks have been thought to be the most persistent medium in time and they were introduced in the form of rectangular mould-based bricks in Mesopotamia at least from the 4th or 3rd millennium BCE (Artioli, 2010 and references therein). In ancient Greece and Rome marble, limestone and granodiorite became the common writing supports in the 1st millennium BCE. However, even if rocks appear imperishable, rock-based inscriptions are attacked by the elements of nature. With time the environment causes the weathering of rocks, resulting in deterioration and destruction of the rock surface layers and limited visibility of the inscribed text. Since many ancient inscriptions are not visible anymore or virtually unreadable, much effort has been put in finding methods, which might unravel the epigraphic content of stone objects.

Commonly, a huge variation in weathering-induced changes in rock-based written artefacts of the same rock can be observed depending on the environmental conditions, which are determined by three main factors: (i) exposure to local climate in terms of humidity and temperature (e.g. Dragovich, 1991; Cooke et al., 1995; Frost and Weier, 2003); (ii) airborne particles of natural and anthropogenic origin and (iii) biological microorganisms. In particular, the local position and altitude of the weathered object can be differently affected by sun, rain and wind (e.g. Moropoulou et al., 1998). In an urban environment, the bottom layer of the atmosphere contains also airborne solid particles resulting mostly from industrial operations, demolition processes, exhaust gases, surface mining, and the combustion of fossil fuels and biomass. Naturally generated particulates can emerge predominantly from volcanic eruptions, dust storms (which are common in Mediterranean regions), and forest and peat fires (Gieré and Querol, 2010). These natural particles prevail over those of anthropogenic origin (98 wt.% versus 2 wt.% according to Gieré and Querol, 2010 and references therein) and hence can form a thick layer on rock-based artefacts. In addition, lichens as weathering agents and other microorganisms like fungi can alter substantially the structure, appearance, and chemical composition of the outermost layer of rocks and thereby the rock mineral-phase composition (Gadd, 2017). Rocks are the major construction constituents of many historical buildings, cultural heritage monuments, gravestones, and writing supports. It is anticipated that they will also be subjected to the impact of bioweathering processes triggered by lichens leading to the in situ alteration of the rock surface. These processes can lead to the formation of new minerals on their surface, like metal oxalates (Frost and Weier, 2003 and references therein), or to the incorporation of metabolic products of lichens like acids or proteins (Holder et al., 2000). Therefore, it is extremely important to study incorporated molecular species as well as possible mineral nanoparticles on the surface of rock-base written artefacts.

So far the chemical- and mineral-phase composition of weathered surfaces of monuments and engraved rocks has predominantly been analysed by X-ray fluorescence (XRF), ion chromatography, atomic absorption and emission spectroscopy, electron probe microanalysis (EPMA), Fourier-transform infrared (FTIR) spectroscopy, and Raman spectroscopy (e.g. Moropoulou et al., 1998; Powers et al., 2005; Twilley, 2006; Pinna et al., 2015). However, the majority of the aforementioned methods require sampling of the outer layer, which is strongly undesirable in the case of historical objects. Non-destructive analysis requires preparation-free methods operating in reflection mode such as XRF reflection, FTIR reflection and Raman spectroscopy, but the application of the first two methods to samples with rough surfaces is complicated. An attempt has been made to recover the lost inscribed text using XRF mapping on trace elements, such as Fe, introduced into the writing support during its engraving (Powers et al., 2005), but the obtained results were not satisfactory enough.

Raman spectroscopy is a method that can non-invasively map the lateral distribution of a guest secondary phase or molecular inclusion in a host matrix via the guest-to-host peak intensity ratio and has the potential for being the appropriate method for the visualization of hardly readable or vanished inscriptions on severely weathered writing supports. The advantage of Raman spectroscopy is fourfold: (i) it is truly non-destructive; (ii) it enables the identification of both crystalline and amorphous phases; (iii) it can detect light element-containing (organic and H-bearing) compounds; and (iv) the utilization of a microscope allows for beam focusing down to 1-2 μm and thus the non-problematic analysis also of rough surfaces. Raman spectroscopy has been applied so far to the determination of the conservational state of wall paintings and buildings (e.g. Edwards and Farwell, 2008) as well as of products being used during restoration treatment of paintings (e.g. Sodo et al., 2019). The ascertainment of the origin of degradation products, such as calcium oxalate films, on the surface of several monuments and frescoes has been achieved also through Raman spectroscopy (e.g. Edwards et al., 1991; Rampazzi et al., 2004; Conti et al., 2012). In particular, the recent development of micro-spatially offset Raman spectroscopy (μ -SORS) allows for probing subsurface layers (Realini et al., 2016; 2017) even in opaque samples (Matousek et al., 2016). Since the first attempts of Smith (2003), a lot of progress has been made in developing portable Raman spectrometers for the identification of decaying products on construction materials and overall on cultural heritage objects. However, such an instrumentation still suffers from some instrumental limitations, such as a low spectral resolution of 4-5 cm^{-1} (e.g. Martínez-Arkarazo et al., 2008; Crippa et al., 2021) which hinders the distinction between different carbonate, sulfate, and nitrate mineral phases (e.g. Colombari, 2012).

Generally, a mechanical treatment with sharp tools, like those used for stone carving, should produce dislocations and microcracks in the material, and the density of such structural defects should be highest in the vicinity of the applied mechanical load. Thus it is reasonable to assume that in rock-based written artefacts there are more cracks and extended structural defects (induced during the engraving of letters) beneath inscribed areas in comparison to non-inscribed ones, independent of whether the inscription is still well preserved or has completely vanished (Fig. 1). Consequently, the incorporation of foreign material into these voids is possible, and the alteration of the original base material is expected to be intensified. This feature can be explained with the elevated molecular diffusion from the external surface to the bulk rock and the enlargement of the effective internal surface area due to cracks and structural defects. For instance, filamentous hyphae from lichens and fungi may penetrate further into an inscribed area through fissures and cracks as well as in between mineral grains and onto cleavage plains if existing (Gadd, 2017). Therefore, the content of the weathering products as newly formed mineral phases or molecular inclusions should be higher beneath an inscription than in areas away from it. Moreover, if the signal from the weathered product can be detected by a certain non-destructive method, it can be used to improve the readability of rock-based written artefacts.

To test this concept, we have analysed two types of inscribed marble with contrasting environmental conditions and different inscription ages - gravestones from the cemetery of Ohlsdorf (Hamburg, Germany) and fragments of a marble slab from Asia Minor (western Turkey), with Raman spectroscopy as well as with complementary powder X-ray diffraction (XRD), wavelength-dispersive EPMA (WD-EPMA), and FTIR spectroscopy. The goals were (i) to identify the deterioration products in marble artefacts depending on the environmental conditions, (ii) to determine propagation depth of these weathering products, foreign particles, or inhabitants beneath inscribed and non-inscribed areas, depending on the weather-exposure time, mineral grain size, and letter colouring, and (iii) to explore the sensitivity of Raman spectroscopy for detecting cracks introduced in

marble while inscribing, via the Raman signal of secondary nanophase or molecular species inhabiting the cracks, which could be further used to develop a non-destructive method for tracing letter remnants.

2 Materials and methods

2.1 Samples

Figure 2a displays one of the marble gravestones, kindly provided by the administration of the Ohlsdorf cemetery in Hamburg, Germany. From the same gravestone, we have prepared cross-section cuts through the inscribed symbols (Fig. 2b) from which Raman spectra along line profiles beneath the inscription (dashed red line; bottom photograph in Fig. 2b) and away from the inscription (dashed blue line; bottom photograph in Fig. 2b) were collected. Additional cuts were prepared for WD-EPMA. The same sample preparation procedure was used for the ancient marble slab from Asia Minor, Turkey. The sample designation, provenance, inscription age, grain size, and letter colouring are given in Table 1. For the purposes of powder XRD and FTIR analyses, material was gently scraped under the microscope from the surface of altered and unaltered areas of samples AM_C1 (Asia Minor) and MaB1A (Hamburg).

2.2 Analytical methods

2.2.1 Powder X-ray diffraction (XRD)

The XRD patterns of powders taken from and far from the alteration zone of the Asia Minor marble were collected with a STOE STADI MP diffractometer operating in Bragg-Brentano geometry and equipped with a curved germanium (111) monochromator, providing $\text{CuK}\alpha_1$ radiation ($\lambda = 1.54056 \text{ \AA}$). Powder diffraction data were recorded at room temperature in a 2θ range between 10° - 70° , with a step size of 0.01° and signal resolution of 0.105° . The assignment of the crystalline phases composing the sample was carried out through the Crystallographica Search-Match 3.1 programme.

2.2.2 Wavelength-dispersive electron probe microanalysis (WD-EPMA)

Chemical element mapping and WD-EPMA of cross sections were conducted with a Cameca SX100 SEM (scanning electron microscope) system with a wavelength-dispersive detector. The electron accelerating voltage used was 15 kV, while the beam current was 20 nA. The following standards were used: albite for Na, MgO for Mg, corundum for Al, apatite for P, BaSO_4 for S and Ba, vanadinite for Cl, GaAs (gallium arsenide) for As, SrTiO_3 for Sr, LiF for F, andradite for Si, Ca, and Fe, and orthoclase for K. The chemical composition of the unaltered area of each marble rock was determined by averaging the EPMA data over 150 points for the Asia Minor artefact and 100 points for the Ohlsdorf gravestones. The altered zone of the Asia Minor fragments was considerably thicker than that of marble from Ohlsdorf and hence its chemical composition could be determined by averaging 45 points, whereas the composition of the altered zones of Ohlsdorf gravestones were analysed by averaging 16 and 25 points for fine- and course-grain marble, respectively. Additionally, randomly found inclusions in the altered zones of marbles from both localities were analysed in ~3-11 points.

2.2.3 Fourier-transform infrared (FTIR) spectroscopy

FTIR spectra were collected in transmittance with a Bruker FTIR spectrometer Vertex 70 equipped with a RT-DLaTGS detector, using the KBr-pellet technique. Spectra in the range of 200-8000 cm^{-1} were obtained by averaging over 32 scans with an instrumental resolution of 2 cm^{-1} and subsequently compensated for the contribution of atmospheric CO_2 and H_2O via the OPUS 7.5 software programme. The IR absorption spectra were baseline corrected with a polynomial function, temperature reduced to account for the Bose-Einstein distribution of phonons, and fitted with pseudo-Voigt peak-shape functions $PV = \mu L + (1-\mu)G$ (L and G stand for Lorentz and Gauss peak-shape functions, respectively, while μ is a variable weight coefficient) to determine the peak positions ω , full widths at half maximum (FWHMs), and integrated intensities I . The data evaluation was carried out through the OriginPro 2019 software package.

2.2.4 Raman spectroscopy

Samples listed in Table 1 were analysed by Raman spectroscopy at room temperature using a Horiba Jobin Yvon T64000 triple-monochromator system coupled with a Symphony LN_2 -cooled charge-coupled device (CCD) detector and an Olympus BH41 confocal microscope with a 50 \times long working distance objective. The Raman scattering was excited with the green line ($\lambda = 514.532 \text{ nm}$) of a Coherent INNOVA 90C FreD Ar^+ laser. The Raman spectrometer was calibrated against the peak at 520.5 cm^{-1} of a silicon standard wafer. The spectral resolution was $\sim 2 \text{ cm}^{-1}$, while the instrumental peak position accuracy was $\sim 0.35 \text{ cm}^{-1}$. The laser-spot diameter on the sample surface was $\sim 2 \text{ }\mu\text{m}$, while the laser power on the sample surface was 7.9 mW. Data were collected in the spectral range of 15-3800 cm^{-1} , with acquisition times varying between 15 and 30 s and averaged over 3-5 loops to improve the signal-to-noise ratio. The measured spectra were evaluated in the same manner as the IR absorption spectra.

3 Results

3.1 Powder XRD analysis

Figure 3 shows the powder XRD patterns collected from the alteration zone and unaltered bulk of the marble segments of Asia Minor to determine their mineral-phase constituents. As expected, calcite (CaCO_3) is the most abundant mineral in both samples, accompanied by minor quantities of dolomite ($\text{CaMg}(\text{CO}_3)_2$). The XRD pattern of the altered area (black line in Fig. 3) additionally indicated a very small amount of quartz (SiO_2). The XRD pattern of unaltered marble from Ohlsdorf resembles that of marble from Asia Minor. Powder XRD analysis could not be employed on the alteration zone of Ohlsdorf gravestones as its infinitesimal thickness did not enable us to collect enough sample material for measurements.

3.2 Wavelength-dispersive element mapping and EPMA

Figures 4 and 5 display the backscattered electron (BSE) images and chemical element maps of studied cross sections of engraved and non-engraved marble from Ohlsdorf and Asia Minor, respectively. As can be seen, the ancient marble from Asia Minor exhibits a much thicker alteration rim than the samples from Ohlsdorf, which most probably results from the longer exposure time to weathering. For both types of marble, the altered layer is characterized by diminishing contents of Ca and enhanced C, indicating degradation of calcite. A similar correlated change in the Ca and C content can be spotted in the irregular cracks in the marble matrix beneath engraved areas, which might have been induced during the engraving, as well as in the

natural cracks that follow the cleavage planes or twin boundaries of calcite (Figs 4 and 5). Furthermore, micrometre-sized particles rich in Fe (see Figs 4 and 5) as well as in Mg, Al, Si, and K (see the supplementary material) can be spotted in the altered layers, which are most probably phyllosilicate grains from the natural mineral dust embedded in the surface layer during the weathering process or randomly distributed phyllosilicates as accessory phases of marble. The maps also suggest that the altered layer is slightly enriched in S, P, and N (supplementary material), which can be related to the effect of the urban environment. The visual examination of the element maps however does not reveal any differences between the altered areas beneath and away from the inscription.

The quantitative chemical analysis (Table 2) verified the outcomes of the element maps. The most remarkable differences between altered and unaltered areas of the same specimen are observed in the Asia Minor marble, in which the $\text{CaO}/\text{sum}_{(\text{matrix})}$ ratio has an average value of 0.95(3), while $\text{CaO}/\text{Sum}_{(\text{AZ})}$ (CaO/Sum of the alteration zone) ratio is $\sim 0.78(15)$. In some cases, e.g. for $\text{SiO}_2_{(\text{matrix})}$ and $\text{Al}_2\text{O}_3_{(\text{matrix})}$ of the Asia Minor samples (Table 2), the standard deviation is greater than the average content, which is due to the heterogeneous distribution of the corresponding element. A common feature among the samples from Hamburg as well as from Asia Minor is that the Mg/Ca ratios tend to increase from the matrix towards the alteration zones of engraved regions and non-inscribed areas. The minor amount of dolomite in the marble segments of Asia Minor, which is less weatherable than calcite (Hartmann et al., 2013), can account for the elevated $\text{Mg}/\text{Ca}_{(\text{AZ})}$ with respect to $\text{Mg}/\text{Ca}_{(\text{matrix})}$. The EPMA data also indicate the relatively homogenous distribution of minor phosphate phase in both the matrix and altered layer of all studied marble specimens. Micas were found as accessory minerals in the matrix, as well as in the alteration zone, of the coarse-grained marbles of both localities. Fluorite (CaF_2) was observed as random inclusions in the unaltered mass of the fine-grained marbles (Hamburg), whereas feldspars and pyrite (FeS_2) were occasionally found in the Asia Minor marble.

3.3 Infrared absorption analysis

Compositional differences between altered and unaltered regions of the same specimen can also be deduced from the FTIR absorption spectra (Fig. 6). As expected, calcite dominates the inscription-free and unaltered area of the marble segments of Asia Minor (red spectrum of Fig. 6) with no extra peaks from additional phases. The characteristic peaks of calcite can be generally subdivided into two main categories, namely those generated by lattice phonon modes (involving Ca vibrations as well as external CO_3 modes) and those by CO_3 vibrational modes. The infrared bands centred around 222, 320, and 345 cm^{-1} pertain to the former vibrational group (e.g. Brusentsova et al., 2010), while the peaks near 712, 876, and 1430 cm^{-1} belong to the latter category and depict the in-plane bending (ν_4), out-of-plane bending (ν_2), and antisymmetric stretching mode (ν_3) of the carbonate ion group, respectively (e.g. Prencipe et al., 2004; Gunasekaran et al., 2006). Minor deviations from these peak positions have been noticed in the spectra of the alteration zones beneath and away from engraved letters (green and black spectra; Fig. 6) and may be caused by trace metal contents or natural impurities in these samples (Gunasekaran et al., 2006). A partial substitution of Ca by Mg in the alteration zones of the samples from Asia Minor and Hamburg could further explain the shift of the most prominent IR peak of calcite at $\sim 1430 \text{ cm}^{-1}$ to higher wavenumbers, which is in accordance with the IR absorption data on calcite, dolomite and magnesite (e.g. Gunasekaran et al., 2006; Schauble et al., 2006). Overtones and combinations of the fundamental calcite phonon modes can be recognized as weak features in the spectra of Fig. 6 at wavenumbers around 1800, 2517, 2860-2880, 2920 and 2982 cm^{-1} (Gaffey, 1986; Gunasekaran et al., 2006). The presence of additional phases in the alteration zone of marble from HH is revealed by the extra IR peaks centred at approximately 1072,

1132, 1267, 1724, 2931, and 3447 cm^{-1} . The assignment of the peak near 1070 cm^{-1} is ambiguous; it may originate from SiO_4 antisymmetric stretching in layered silicates like muscovite (e.g. Singha and Singh, 2016, and references therein) or even from organic compounds (e.g. Coates, 2000). The IR peak near 1132 cm^{-1} matches very well the strongest IR peak of gypsum ($\text{CaSO}_4 \cdot 2\text{H}_2\text{O}$), (Bishop et al., 2014, and references therein), attributed to the $\nu_3(\text{SO}_4)$ antisymmetric stretching. The broad band near 1267 cm^{-1} could be a sign of whewellite ($\text{CaC}_2\text{O}_4 \cdot \text{H}_2\text{O}$), assigned to the stretching modes of the oxalate group (Petrov and Šoptrajanov 1975; Frost, 2004) but suppressed by the strongest IR peak of calcite $\sim 1430 \text{ cm}^{-1}$ (e.g. Pinna et al., 2015). The peak at 1724 cm^{-1} is indicative of oxalic acid (e.g. Coates, 2000), which is the most important bioweathering agent produced by lichens and can lead to the secondary formation of calcium oxalates (like whewellite) after its reaction with carbonates (Gadd, 2017). Evidence of organic compounds in the altered area of the coarse-grained marbles of Hamburg (sample MaB1A) is supported also by the peak at ca. 2930 cm^{-1} , which is attributed to the symmetric stretching vibration of the methylene group (Coates, 2000). The broad IR band near 3447 cm^{-1} , arising from O-H bond stretching, is most probably due to H_2O incorporated in microvoids and defect OH^- groups on internal surfaces; water and hydroxyl groups in hydrous minerals like whewellite and gypsum resulting from weathering can also contribute to this band. It is worth noting that moisture remnants in the KBr pellets can also contribute to the broad IR band near 3447 cm^{-1} ; however, this band was systematically stronger in the spectra collected from the altered layers (Fig. 6), indicating the presence of extra hydrous species in the altered marble surface. The altered layer of the Asia Minor marble also exhibits a broad IR peak generated by O-H bond stretching, as well as extra peaks at 1047 and 1084 cm^{-1} . The peak at 1047 cm^{-1} is close in wavenumber to the $\nu_3(\text{PO}_4^{3-})$ antisymmetric stretching of apatite (e.g. Markovic et al., 2004; Balan et al., 2011; Eisa et al., 2015), whilst the peak at 1084 cm^{-1} matches very well the strongest IR absorption signal of quartz (Saikia et al., 2008).

3.4 Raman scattering analysis

Raman measurements were conducted on cross sections from each rock type along lines beneath and away from inscriptions where the line began from the surface and reached depths of either 1 or 2 mm. Figure 7 displays selected Raman spectra of representative marble cross sections. The Raman spectra collected from the matrix of coarse-grained (Fig. 7a, b, and d) and fine-grained marble (Fig. 7c) contain only peaks typical of calcite: the strongest peak at 1087 cm^{-1} ($\nu_1(\text{CO}_3^{2-})$ symmetric stretching) being accompanied by the considerably weaker peaks near 156 and 282 cm^{-1} (external (CO_3^{2-}) modes), as well as at 713 ($\nu_4(\text{CO}_3^{2-})$ in-plane bending) and 1436 cm^{-1} ($\nu_3(\text{CO}_3^{2-})$ antisymmetric stretching) (e.g. Behrens et al., 1995; De La Pierre et al., 2014). Some marble samples exhibited a weak peak at 1067 cm^{-1} which is due to the ^{18}O satellite mode of the ν_1 symmetric stretching vibration of the CO_3 anion with an isotopic shift of 19.7 cm^{-1} (De La Pierre et al., 2014).

The line profiles collected away from the letters on marble from Ohlsdorf did not reveal any additional peaks. In strong contrast, various weathering-related products were detected at the first 100 μm from the surface beneath uncoloured engraved letters on a coarse-grained marble from Ohlsdorf via their characteristic Raman peaks (Fig. 7a), which confirms that the inscription introduces cracks and voids that can facilitate the formation and propagation of weathering-related products through the bulk and allow the host to be infiltrated by foreign substances. The strongest extra peaks are observed near 1154 and 1517 cm^{-1} , indicating crack-enhanced organic molecular inclusions, as they result from the $\nu(\text{C-C})$ and $\nu(\text{C=C})$ stretching modes of carotenoids in lichen, respectively (Holder et al., 2000; Edwards et al., 2003). The Raman peak near 960 cm^{-1} should indicate the presence of the metal phosphate phase, e.g. hydroxylapatite or calcium orthosilicate, as its position matches very well the

wavenumber of the corresponding Raman-active symmetric PO_4 stretching mode (Edwards et al., 2004; Jegova et al., 2013; Litasov and Podgornykh, 2017; Stammeier et al., 2018); we assume this phase belongs to the apatite mineral group, which represents the most common accessory phosphate minerals in marble. The additional peaks around 1187 and 1278 cm^{-1} can be ascribed to the aromatic ring breathing typical of diverse organic compounds and the $\text{CH}_2=\text{CH}_2$ in-plane rocking mode of alkenes, respectively (e.g. Holder et al., 2000; Barnard and de Waal, 2006). Furthermore, in the first 100 μm of the same line profile we could also identify gypsum through its strongest peak at 1005 cm^{-1} generated by the $\nu_1(\text{SO}_4)$ symmetric stretching mode (Takahashi et al., 1983; Prasad et al., 2001; Buzgar et al., 2009).

The letter colouring apparently suppresses the weathering of marble as none of the above-mentioned organic compounds and minerals were detected beneath coloured letters on course-grained marble from Ohlsdorf (Fig. 7b). The superficial layer (0 μm) exhibits a very strong peak at $\sim 152 \text{ cm}^{-1}$ and several weak peaks at $\sim 204, 335, 390, 506,$ and 628 cm^{-1} (see also supplementary Fig. S5). This is a typical Raman pattern of synthetic nanosized anatase with a large internal surface which is used in white pigments (Sahoo et al., 2009). This indicates that the major ingredient of the white pigment used to colour the letters in Ohlsdorf marble is nanosized anatase. The Raman peaks of such nanosized anatase are broader and appear at slightly different positions with respect to those of well crystalline anatase (143, 197, 321, 395, 515 and 638 cm^{-1} ; see supplementary Fig. S5) due to the competing phonon confinement effect and the impact of inherent structural defects (Zhang et al., 2000; Ceballos-Chuc et al., 2018). The most intense Raman-active E_g mode ($\sim 143 \text{ cm}^{-1}$ in well crystalline anatase) predominately experiences phonon confinement effects, and thus its position ω and FWHM are directly related to the mean crystallite size (Ceballos-Chuc et al., 2018). Spectral fitting of the experimental data gives $\omega = 152.1 \text{ cm}^{-1}$ and $\text{FWHM} = 22 \text{ cm}^{-1}$ for the white pigment while giving $\omega = 143.0 \text{ cm}^{-1}$ and $\text{FWHM} = 8 \text{ cm}^{-1}$ for reference well crystalline anatase, revealing nanosized anatase in the pigment with an average particle size of 6 nm.

The size of the mineral grains in marble is also critical for the propagation of the weathering-related products. The Raman line profiles of the fine-grained gravestone from Ohlsdorf (Fig. 7c) disclosed no additional mineral phases or organic compounds beneath the engraved areas. It is however worth noting that the inscription age of the studied gravestones from Ohlsdorf is ~ 60 years, whereas for ancient written artefacts, exposed to weathering for a much longer time, the mineral grain size might be less important.

The Raman spectra collected along a line beneath the inscribed area of the ancient marble artefact from Asia Minor are shown in Fig. 7d. Two peculiar features are observed for this sample. (i) The dominant CaCO_3 polymorph within the first 50- μm beneath the inscription is aragonite rather than calcite, as revealed by the presence of the strongest aragonite peak at 1085 cm^{-1} , together with fingerprinting Raman peaks at 114, 153, 179, 194, 207, 246, 702, and 707 cm^{-1} (e.g. Frech et al., 1980; De La Pierre et al., 2014). Calcite was firstly detected at depths of approximately 120 μm , and (ii) two broad additional peaks centred around 1365 and 1595 cm^{-1} , which at depths of ~ 60 -120 μm were systematically stronger beneath the inscription than away from the inscription. These extra peaks correspond to the so-called D (diamond-like) and G (graphite-like) peaks in amorphous carbon arising from the ring breathing and C-C bond stretching of sp^2 -hybridized C, respectively (e.g. Ferrari and Robertson, 2004; Tomasini et al., 2012). Therefore, the main foreign material in ancient marble from Asia Minor seems to be soot-like carbon.

The abundance and penetration depth of the extra phases can be quantified by the integrated intensity of the strongest Raman peak of the corresponding guest compound normalized to that of the major peak of the host matrix. In the case of the

Asia Minor marble, we used the intensity ratio between the G peak near 1595 cm⁻¹, representing the carbonaceous material, and the strongest carbonate peak near 1086 cm⁻¹. The resulting intensity ratio ($\rho_1 = I_{1595}/I_{1086}$) was plotted against the distance to the surface beneath inscribed and non-inscribed regions (Fig. 8a), and the data points were fitted with asymmetric lognormal statistical distribution $\rho_1(d) = \frac{A}{\sqrt{2\pi wd}} e^{-\left(\ln\left(\frac{d}{dc}\right)\right)^2 / (2w^2)}$. We have chosen a simplified single-peak statistical function to fit $\rho_1(d)$ because such a function represents best the apparent existence of a maximum around 60 μm for the non-inscribed areas and around 70-80 μm for the inscribed areas. It is obvious that the peak of $\rho_1(d)$ beneath inscriptions is much higher and wider than that of $\rho_1(d)$ away from them, and it is positioned at greater depth. This clearly shows that carbonaceous material is more abundant in inscribed areas than in untreated ones of the ancient marbles of Asia Minor, as a result of the presence of cracks and voids formed during the engraving process.

In the case of marble from Ohlsdorf, subjected mainly to biodegradation due to the specifics of the local climate, we used the intensity ratio $\rho_2 = I_{1520}/I_{1087}$, that is, the Raman signal from $\nu(\text{C}=\text{C})$ of carotenoids versus that from $\nu_1(\text{CO}_3)$ of calcite (Fig. 8b). As can be seen, the $\rho_2(d)$ ratio rapidly decreases with depth, following an exponential decay $\rho_2(d) = Ae^{-d/t}$. However, the metabolic products of lichens were much more abundant and persist at depths up to ~100 μm beneath engraved letters (Fig. 8b; red lines) of the coarse-grained marbles from Ohlsdorf, as opposed to away from them (Fig. 8b; blue lines), carotenoids were less abundant and limited within the first 50 μm from the surface of the rock-based written artefact. In some cases (e.g. sample MaB1B) carotenoids could only be detected on the outermost surface (1-2 μm in depth) of untreated marble regions. Furthermore, ρ_2 has much higher values in every specific measured point beneath inscriptions in comparison with non-inscribed areas when we consider the same cross section (e.g. line profile L1 versus line profile L102 of sample MaB1A in Fig. 8b). Thus, the abundance of metabolic products, i.e. carotenoids produced by lichen, is apparently enhanced beneath the inscribed areas of the coarse-grained gravestones.

4 Discussion

As shown above, due to the strongest Raman cross section of organic C=C stretching, its Raman signal can be potentially used to trace the heterogeneous lateral distribution of cracks in the altered layer of biodegraded marble (Hamburg). Likewise, the strong Raman signal from sp²-hybridized C-C bond stretching provides a feasible way to scan the lateral distribution of cracks in weathered marble containing amorphous carbon (Asia Minor). The latter could have been formed as a result of the impact of airborne carbonaceous particles of anthropogenic origin, e.g. electric-power generation, traffic, oil- and wood-fired heating, industrial manufacturing processes, and fossil fuel combustion. Indeed, soot is a feature of ascribed urban environmental pollution (e.g. Wentzel et al., 2003; Engling and Gelencsér, 2010; Grobétý et al., 2010) and should be present in the altered layer of ancient written artefacts from the vicinity of large cities. Soot deposition on the surface of a late Bronze Age/Iron Age mortar found in Danebury (Hampshire, UK) has been detected via Raman spectroscopy (Edwards and Farwell, 2008). Moreover, the Raman signal from both the organic and inorganic C-C stretching vibrations may be resonantly enhanced by using UV laser excitation radiation (e.g. Ferrari and Robertson 2004). The peak position of the $\nu(\text{C}=\text{C})$ stretching mode, as well of sp²-hybridized C-C bond, may slightly vary due to substitutional or structural defects (e.g. Barnard and de Waal, 2006; De Oliveira et al., 2010), but it may also slightly change with the laser wavelength (e.g. Ferrari and Robertson 2004). Hence,

in a follow-up study we are going to investigate in detail the feasibility of Raman spectroscopy, varying the excitation laser wavelength between 633 and 325 nm, to map cracks on marble-written artefacts with a mechanically removed upper-layer material to the level where the inscription becomes hardly readable.

The detection of aragonite instead of calcite beneath the inscribed areas in the Asia Minor marble artefacts seems to be statistically irrelevant at least for the sole ancient inscribed marble studied here. Further experiments are necessary to check whether aragonite is indeed a feature related to inscribed areas of marble artefacts subjected to Mediterranean climate. Therefore, although aragonite is well distinguished from calcite by its Raman signature below 300 cm^{-1} , currently we cannot recommend that it be used as a reliable criterion to indirectly trace topological defects and plastic deformations in marble. However, another candidate to scan cracks and voids introduced during the inscribing could be gypsum. The presence of gypsum in the outer altered film of the coarse-grained gravestones beneath and away from inscribed letters was monitored by FTIR and Raman spectroscopy. Element mapping (see supplementary material) and EPMA (Table 2) also indicated a slight increase in S in the altered layer. Gypsum has been already reported to be the main weathering product of marble or limestone monuments and statues due to the acid damage of SO_2 -gas pollutant in urban and industrial environments (e.g. Moropoulou et al., 1998; Rampazzi et al., 2004; Crisci et al., 2009; Conti et al., 2012; Pinna et al., 2015); SO_2 interacts with atmospheric water, forming sulfuric acid (H_2SO_4), whose wet deposition on the marble or limestone surface drives the formation of gypsum (e.g. Maguregui et al., 2012). In the coarse-grained gravestone samples from Ohlsdorf gypsum could be detected via Raman spectroscopy at a depth of 50-100 μm beneath inscriptions and to a lesser extent, or entirely not, at a depth of 0–50 μm beneath untreated areas of the same cuts. Therefore, the presence of gypsum at depths that exceed 50 μm is denotative of inscribed areas only, and similarly to carotenoids and soot-like carbon, it is facilitated by cracks induced during the carving of the letters. It is worth noting that gypsum as a weathered product has been found beneath the surface of the monuments at a depth ranging from 200 to 500 μm , depending on the construction age (15th century BCE-13th century CE) and whether it was exposed to or sheltered from rainfall (Moropoulou et al., 1998; Conti et al., 2012). Therefore, since $\nu_1(\text{SO}_4)$ also has a relatively high Raman cross section, nanosized gypsum can be potentially used to scan letters in the absence of other weathering-related products exhibiting stronger Raman peaks.

The extra content of mica, apatite, and quartz mineral particles in the altered layers of marble from Ohlsdorf and Asia Minor, detected by the combined application of Raman, IR, EPMA, and XRD, is most probably related to natural airborne mineral dust (e.g. Engelbrecht and Derbyshire, 2010, e.g. Grobéty et al., 2010). None of the applied analytical methods revealed any differences in the distribution of these mineral phases beneath and away from the inscribed areas.

The Raman spectra of coloured inscriptions disclosed that pigment, i.e. synthetic anatase, prevents lichen formation on their surface. Nevertheless, traces of TiO_2 -pigments could be potentially used for tracking hardly readable engravings as pigment particles could also enter the cracks and voids of the inscribed medium like the other weathering-related products. The extremely strong Raman peak of anatase near $142\text{-}152\text{ cm}^{-1}$ allows for the detection of this compound with fractions less than 0.1%. Thus the huge Raman scattering of synthetic anatase might be used as a marker of inscribed regions not only for modern artefacts but also for ancient rock-based written artefact as traces of this white pigment have been monitored already on Roman wall paintings (Roman villa in UK) from ~150 CE (Edwards et al., 2006).

5 Conclusions

The results from our Raman spectroscopic analysis clearly reveal detectable dissimilarities in the weathering-induced molecular and mineral embeddings beneath inscribed and non-inscribed areas of the same specimen. This was feasible through the Raman intensity of the sp^2 -hybridized C-C bond stretching and organic C=C stretching modes normalized to the Raman intensity of the host marble, illustrating a higher abundance and in-depth penetration of soot-like carbon (in the case of Asia Minor) and carotenoids produced by lichens (in the case of Hamburg) beneath inscribed letters. Therefore, such Raman signals, originating from suitable weathering-related products, can potentially be used to scan the lateral distribution of cracks, introduced during the engraving procedure. Of critical importance could be also the presence of gypsum which could be used as a second marker of cracks and fissures induced during the inscribing process, especially when the studied artefacts are from urban environments.

Significant factors that influence the nature and propagation of weathering-related products of the same rock type are as follows (i) different inscription age. BSE images and chemical element maps highlighted an approximately 3 times thicker alteration layer of the ~2000-year-old inscribed marble from Asia Minor than the ~60-year-old engraved marbles from Hamburg. (ii) Local climate and urban environment. Marble in a Mediterranean (Asia Minor) and in temperate oceanic climate (Hamburg) near or within an urban environment can be influenced by diverse decaying agents or characterized by different degradation products, i.e. bioweathering triggered by lichen and acid damage of SO_2 gases in the case of Hamburg versus airborne mineral dust and soot-like carbonaceous particles in the case of Asia Minor. (iii) Grain size. No additional mineral phases or organic compounds could be monitored beneath the engravings of the fine-grained gravestones of Ohlsdorf.

Letter colouring behaves as an inhibitor for the propagation of lichen bioweathering of marble as none of the above-mentioned weathering-related products were detected beneath coloured letters on coarse-grained marbles from Ohlsdorf. However, the strong Raman scattering of the white pigment that we observed, i.e. synthetic anatase, could be used as a marker of the exact location of inscriptions as pigments are expected to enter the small cavities and cracks characteristic of inscribed rock-based written artefacts.

Overall, the outcomes of this study provide a conceivable way for uncovering hardly readable or completely vanished inscribed text on rock-based written artefacts via the further systematic study of relevant samples through Raman 2D mapping, especially if combined with the novel μ -SORS method (e.g. Conti et al., 2015). Further work, based on Raman spectroscopy, is in progress to ascertain the effect of different acids and atmospheric CO_2 under controlled temperature and humidity levels upon freshly inscribed marble and limestone pieces as a next step to understand the response of rock-based written artefacts in an urban environment and to assist in the conservation of our cultural heritage.

Data availability

All data derived from this research are available upon request from the corresponding author.

Author contributions

BM, JS, and KH initiated the project. SA performed the data collection and evaluation. SA wrote the paper with input from BM, JS, and KH. All authors discussed and interpreted the results.

Competing interests

The authors declare that they have no conflict of interest.

Acknowledgements

The research for this study was funded by the Deutsche Forschungsgemeinschaft (DFG, German Research Foundation) under Germany's Excellence Strategy – EXC 2176 'Understanding Written Artefacts: Material, Interaction and Transmission in Manuscript Cultures', project no. 390893796. The research was conducted within the scope of the Centre for the Study of Manuscript Cultures (CSMC) at Universität Hamburg. We thank Stefanie Heidrich and Peter Stutz, Universität Hamburg for help with WD-EPMA measurements and sample preparation as well as to Joachim Ludwig and Leonie Tipp for partial help with XRD and Raman measurements, respectively. We are very grateful to the administration and employees of the cemetery of Ohlsdorf for kindly providing marble gravestones.

References

- Artioli, G. (Eds.): Scientific methods and cultural heritage. Oxford University Press Inc., New York, 2010.
- Balan, E., Delattre, S., Roche, D., Segalen, L., Morin, G., Guillaumet, M., Blanchard, M., Lazzeri, M., Brouder, C., and Salje, E.K.H.: Line-broadening effects in the powder infrared spectrum of apatite. *Phys. Chem. Minerals*, 38, 111-122, 2011.
- Barnard, W. and de Waal, D.: Raman investigation of pigmentary molecules in the molluscan biogenic matrix. *J. Raman Spectrosc.*, 37, 342-352, 2006.
- Behrens, G., Kuhn, L.T., Ubig, R., and Heuer, A.H.: Raman spectra of vateritic calcium carbonate. *Spectrosc. Lett.*, 28, 983-995, 1995.
- Bishop, J.L., Lane, M.D., Dyar, M.D., King, S.J., Brown, A.J., and Swayze, G.A.: Spectral properties of Ca-sulfates: Gypsum, basanite and anhydrite. *Am. Mineral.*, 99, 2105-2115, 2014.
- Brusentsova, T.N., Peale, R.E., Maukonen, D., Harlow, G.E., Boesenberg, J.S., and Ebel, D.: Far infrared spectroscopy of carbonate minerals. *Am. Mineral.*, 95, 1515-1522, 2010.
- Buzgar, N., Buzatu, A., and Sanislav, I.V.: The Raman study of certain sulfates. *An. Stiint. Univ. Al. I. Cuza Iasi Geol.*, 55, 5-23, 2009.
- Ceballos-Chuc, M.C., Ramos-Castillo, C.M., Alvarado-Gil, J.J., Oskam, G., and Rodríguez-Gattorno, G.: Influence of brookite impurities on the Raman spectrum of TiO₂ anatase nanocrystals. *J. Phys. Chem. C*, 122, 19921-19930, 2018.
- Coates, J.: Interpretation of infrared spectra, a practical approach, in: *Encyclopedia of Analytical Chemistry*, edited by Meyers, R.A., John Wiley & Sons Ltd, Chichester, 10815-10837, 2000.
- Colomban, P.: The on-site/remote Raman analysis with mobile instruments: a review of drawbacks and success in cultural heritage studies and other associated fields. *J. Raman Spectrosc.*, 43, 1529-1535, 2012.
- Conti, C., Aliatis, I., Colombo, C., Greco, M., Possenti, E., Realini, M., Castignoli, C., and Zerbi, G.: μ -Raman mapping to study calcium oxalate historical films. *J. Raman Spectrosc.*, 43, 1604-1611, 2012.

- Conti, C., Colombo, C., Realini, M., and Matousek, P.: Subsurface analysis of painted sculptures and plasters using micrometer-scale spatially offset Raman spectroscopy (micro-SORS). *J. Raman Spectrosc.*, 46, 476-482, 2015.
- Cooke, R.U., Inkpen, R.J., and Wiggs, G.F.S.: Using gravestones to assess changing rates of weathering in the United Kingdom. *Earth Surf. Process. Landf.*, 20, 531-546, 1995.
- Crippa, M., Legnaioli, S., Kimbriel, C., and Ricciardi, P.: New evidence for the international use of calomel as a white pigment. *J. Raman Spectrosc.*, 52, 15-22, 2021.
- Crisci, G.M., La Russa, M.F., Malagodi, M., Mariani, F., Mazzoleni, P., Pezzino, A., and Ruffolo, S.A.: Study of alteration and degradation products of a Roman marble sarcophagus located in the medieval cloister of the old St Cosimato's Convent, now the new "Regina Margherita Hospital" (Rome). *Conserv. Sci. Cult. Herit.*, 9, 143-156, 2009.
- De La Pierre, M., Carteret, C., Maschio, L., André E., Orlando, R., and Dovesi, R.: The Raman spectrum of CaCO₃ polymorphs calcite and aragonite: A combined experimental and computational study. *J. Chem. Phys.*, 140, 164509, 2014.
- De Oliveira, V.E., Castro, H.V., Edwards, H.G.M., and de Oliveira, L.F.C.: Carotenes and carotenoids in natural biological samples: a Raman spectroscopic analysis. *J. Raman Spectrosc.*, 41, 642-650, 2010.
- Dragovich, D.: Marble weathering in an industrial environment, Eastern Australia. *Environ. Geol. Water Sci.*, 17, 127-132, 1991.
- Edwards, H.G.M., Colombari, P., and Bowden, B.: Raman spectroscopic analysis of an English soft-paste porcelain plaque-mounted table. *J. Raman Spectrosc.*, 35, 656-661, 2004.
- Edwards, H.G.M. and Farwell, D.W.: The conservational heritage of wall paintings and buildings: an FT-Raman spectroscopic study of prehistoric, Roman, medieval and Renaissance lime substrates and mortars. *J. Raman Spectrosc.*, 39, 985-992, 2008.
- Edwards, H.G.M., Farwell, D.W., and Seaward, M.R.D.: Raman spectra of oxalates in lichen encrustations on Renaissance frescoes. *Spectrochim. Acta A*, 47, 1531-1539, 1991.
- Edwards, H.G.M., Hassan, N.F.N., and Middleton, P.S.: Anatase – a pigment in ancient artwork or a modern usurper? *Anal. Bioanal. Chem.*, 384, 1356-1365, 2006.
- Edwards, H.G.M., Seaward, M.R.D., Attwood, S.J., Little, S.J., de Oliveira, L.F.C., and Tretiach, M.: FT-Raman spectroscopy of lichens on dolomitic rocks: an assessment of metal oxalate formation. *Analyst*, 128, 1218-1221, 2003.
- Eisa, M.Y., Al Dabbas, M., and Abdulla, F.H.: Quantitative identification of phosphate using X-ray diffraction and Fourier transform infrared (FTIR) spectroscopy. *Int. J. Curr. Microbiol. App. Sci.*, 4, 270-283, 2015.
- Engelbrecht, J.P. and Derbyshire, E.: Airborne mineral dust. *Elements*, 6, 241-246, 2010.
- Engling, G. and Gelencsér, A.: Atmospheric brown clouds: from local air pollution to climate change. *Elements*, 6, 223-228, 2010.
- Ferrari, A.C. and Robertson, J.: Raman spectroscopy of amorphous, nanostructured, diamond-like carbon, and nanodiamond. *Phil. Trans. R. Soc. Lond. A*, 362, 2477-2512, 2004.
- Frech, R., Wang, E.C., and Bates, J.B.: The i.r. and Raman spectra of CaCO₃ (aragonite). *Spectrochim. Acta A*, 36, 915-919, 1980.
- Frost, R.L. and Weier, M.L.: Raman spectroscopy of natural oxalates at 298 and 77K. *J. Raman Spectrosc.*, 34, 776-785, 2003.
- Frost, R.L.: Raman spectroscopy of natural oxalates. *Anal. Chim. Acta*, 517, 207-214, 2004.

- Gadd, G.M.: Fungi, rocks, and minerals. *Elements*, 13, 171-176, 2017.
- Gaffey, S.J.: Spectral reflectance of carbonate minerals in the visible and near infrared (0.35-2.55 microns): calcite, aragonite, and dolomite. *Am. Mineral.*, 71, 151-162, 1986.
- Gieré, R. and Querol, X.: Solid particulate matter in the Atmosphere. *Elements*, 6, 215-222, 2010.
- Grobéty, B., Gieré, R., Dietze, V., and Stille, P.: Airborne particles in the urban environment. *Elements*, 6, 229-234, 2010.
- Gunasekaran, S., Anbalagan, G., and Pandi, S.: Raman and infrared spectra of carbonates of calcite structure. *J. Raman Spectrosc.*, 37, 892-899, 2006.
- Hartmann, J., West, A.J., Renforth, P., Köhler, P., De La Rocha, C.L., Wolf-Gladrow, D.A., Dürr, H.H., and Scheffran, J.: Enhanced chemical weathering as a geoengineering strategy to reduce atmospheric carbon dioxide, supply nutrients, and mitigate ocean acidification. *Rev. Geophys.*, 51, 113-149, 2013.
- Holder, J.M., Wynn-Williams, D.D., Rull Perez, F., and Edwards, H.G.M.: Raman spectroscopy of pigments and oxalates in situ within epilithic lichens: *Acarospora* from the Antarctic and Mediterranean. *New Phytol.*, 145, 271-280, 2000.
- Jegova, G., Titorenkova, R., Rashkova, M., Mihailova, B.: Raman and IR reflection micro-spectroscopic study of Er:YAG laser treated permanent and deciduous human teeth. *J. Raman Spectrosc.*, 44, 1483-1490, 2013.
- Litasov, K.D. and Podgornykh N.M.: Raman spectroscopy of various phosphate minerals and occurrence of tuite in the Elga IIE iron meteorite. *J. Raman Spectrosc.*, 48, 1518-1527, 2017
- Maguregui, M., Knuutinen, U., Martínez-Arkarazo, I., Giakoumaki, A., Castro, K., and Madariaga, J.M.: Field Raman analysis to diagnose the conservation state of excavated walls and wall paintings in the archaeological site of Pompeii (Italy). *J. Raman Spectrosc.*, 43, 1747-1753, 2012.
- Markovic, M., Fowler, B.O., Tung, M.S.: Preparation and comprehensive characterization of a calcium hydroxyapatite reference material. *J. Res. Natl. Inst. Stand. Technol.*, 109, 553-568, 2004.
- Martínez-Arkarazo, I., Smith, D.C., Zuloaga, O., Olazabal, M.A., and Madariaga, J.M.: Evaluation of three different mobile Raman microscopes employed to study deteriorated civil building stones. *J. Raman Spectrosc.*, 39, 1018-1029, 2008.
- Matousek, P., Conti, C., Realini, M., Colombo, C.: Micro-scale spatially offset Raman spectroscopy for non-invasive subsurface analysis of turbid materials. *Analyst*, 141, 731-739, 2016.
- Moropoulou, A., Bisbikou, K., Torfs, K., Van Grieken, R., Zezza, F., and Macri, F.: Origin and growth of weathering crusts on ancient marbles in industrial atmosphere. *Atmos. Environ.*, 32, 967-982, 1998.
- Petrov, I. and Šoptrajanov, B.: Infrared spectrum of whewellite. *Spectrochim. Acta A.*, 31, 309-316, 1975.
- Pinna, D., Galeotti, M., and Rizzo, A.: Brownish alterations on the marble statues in the church of Orsanmichele in Florence; what is their origin? *Herit. Sci.*, 3, 7, 2015.
- Powers, J., Clinton, N.D., Huang, R., Smilgies, D.M., Bilderback, D., Clinton, K., and Thorne, R.E.: X-ray fluorescence recovers writing from ancient inscriptions. *Z. Papyr. Epigr.*, 152, 221-227, 2005.
- Prasad, P.S.R., Pradhan, A., and Gowd, T.N.: In situ micro-Raman investigation of dehydration mechanism in natural gypsum. *Curr. Sci.*, 80, 1203-1207, 2001.
- Prencipe, M., Pascale, F., Zicovich-Wilson, C.M., Saunders, V.R., Orlando, R., and Dovesi, R.: The vibrational spectrum of calcite (CaCO₃): an ab initio quantum-mechanical calculation. *Phys. Chem. Minerals*, 31, 559-564, 2004.

- Rampazzi, L., Andreotti, A., Bonaduce, I., Colombini, M.P., Colombo, C., and Toniolo, L.: Analytical investigation of calcium oxalate films on marble monuments. *Talanta*, 63, 967-977, 2004.
- Realini, M., Botteon, A., Conti, C., Colombo, C., Matousek, P.: Development of portable defocusing micro-scale spatially offset Raman spectroscopy. *Analyst*, 141, 3012-3019, 2016.
- Realini, M., Conti, C., Botteon, A., Colombo, C., Matousek, P.: Development of a full micro-scale spatially offset Raman spectroscopy prototype as a portable analytical tool. *Analyst*, 142, 351-355, 2017.
- Saikia, B.J., Parthasarathy, G., and Sarmah, N.C.: Fourier transform infrared spectroscopic estimation of crystallinity in SiO₂ based rocks. *Bull. Mater. Sci.*, 31, 775-779, 2008.
- Schauble, E.A., Ghosh, P., and Eiler, J.M.: Preferential formation of ¹³C-¹⁸O bonds in carbonate minerals, estimated using first-principles lattice dynamics. *Geochim. Cosmochim. Acta*, 70, 2510-2529, 2006.
- Singha, M. and Singh, L.: Vibrational spectroscopic study of muscovite and biotite layered phyllosilicates. *Indian J. Pure Appl. Phys.*, 54, 116-122, 2016.
- Smith, D.C.: In situ mobile subaquatic archaeometry evaluated by non-destructive Raman microscopy of gemstones lying under impure waters. *Spectrochim. Acta A*, 59, 2353-2369, 2003.
- Sodo, A., Tortora, L., Biocca, P., Muncicchia, A.C., Fiorin, E., and Ricci, M.A.: Raman and time of flight secondary ion mass spectrometry investigation answers specific conservation questions on Bosch painting Saint Wilgefortis Triptych. *J. Raman Spectrosc.*, 50, 150-160, 2019.
- Stammeier, J.A., Purgstaller, B., Hippler, D., Mavromatis V., and Dietzel, M.: In-situ Raman spectroscopy of amorphous calcium phosphate to crystalline hydroxyapatite transformation. *Methods X*, 5, 1241-1250, 2018.
- Takahashi, H., Maehara, I., and Kaneko, N.: Infrared reflection spectra of gypsum. *Spectrochim. Acta A*, 39, 449-455, 1983.
- Tomasini, E.P., Halac, E.B., Reinoso, M., Di Liscia, E.J., and Maier, M.S.: Micro-Raman spectroscopy of carbon-based black pigments. *J. Raman Spectrosc.*, 43, 1671-1675, 2012.
- Twilley, J.: Raman spectroscopy investigations of the weathering alteration of a predazzite marble mouflon of the Indus Valley Culture. *J. Raman Spectrosc.*, 37, 1201-1210, 2006.
- Wentzel, M., Gorzawski, H., Naumann, K-H., Saathoff, H., and Weinbruch, S.: Transmission electron microscopical and aerosol dynamical characterization of soot aerosols. *J. Aerosol Sci.*, 34, 1347-1370, 2003.
- Zhang, W.F., He, Y.L., Zhang, M.S., Yin, Z., and Chen, Q.: Raman scattering study on anatase TiO₂ nanocrystals. *J. Phys. D: Appl. Phys.*, 33, 912-916, 2000.

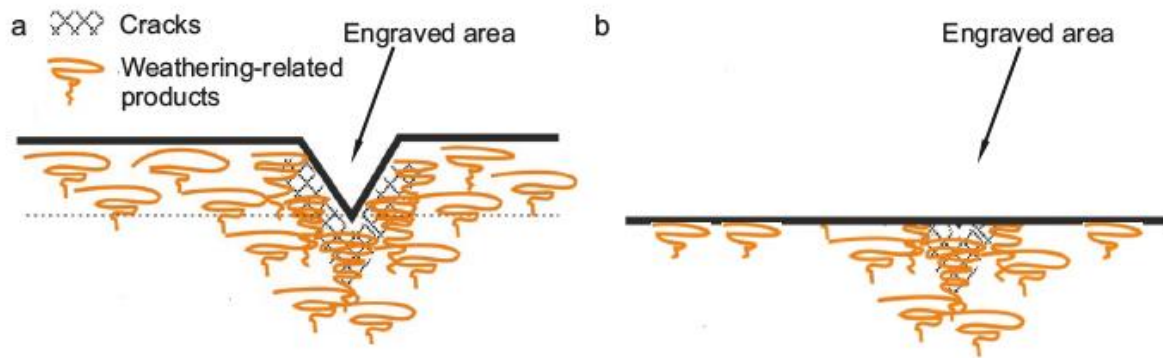


Figure 1: Schematic representations of cross sections of an inscribed object in which the products directly or indirectly induced by weathering processes are more prominent beneath the engraved area than away from it. (a): the inscription is still legible; (b): the surface is deteriorated to the extent in which the inscription is hardly readable or no longer readable.



Figure 2: (a) Photograph of engraved gravestone (MaD1) from Ohlsdorf (Hamburg Germany); the solid red rectangular lines mark the areas from which samples were cut, where A and B denote cuts from the upper and bottom part of the gravestone (e.g. MaD1A and MaD1B, respectively). (b) Top and side view of sample MaD1B_C4, corresponding to the dashed white rectangle in (a) The dashed red and blue lines in (b) trace the measured line profiles beneath and away from inscriptions, respectively.

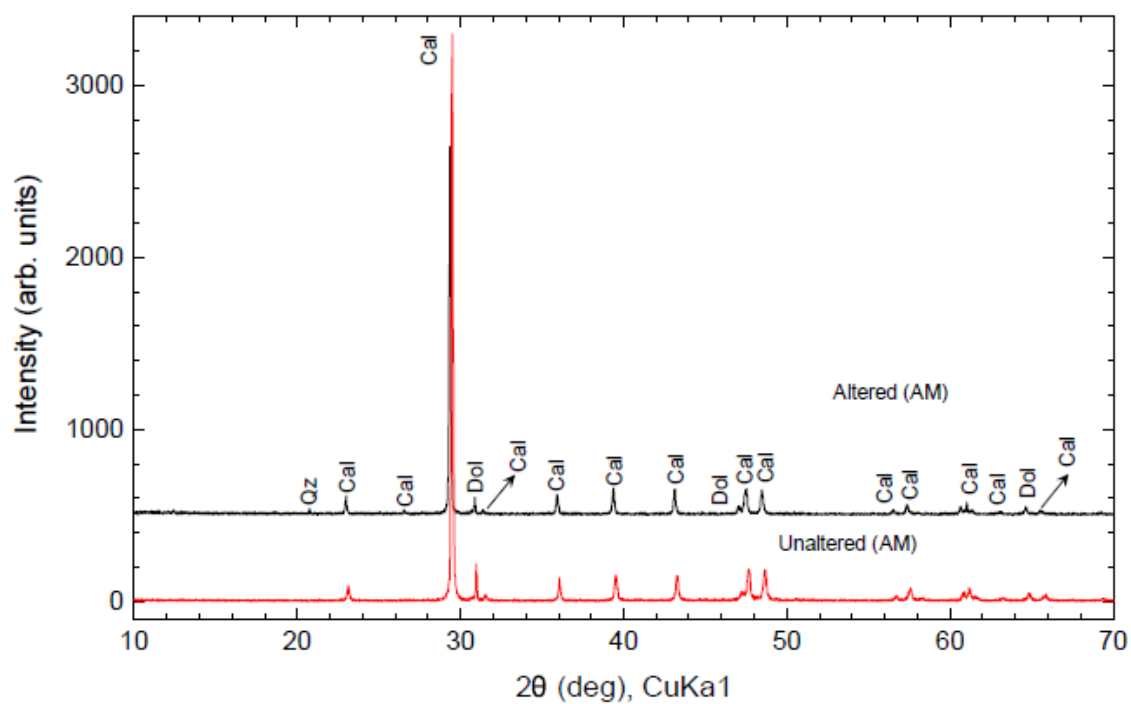


Figure 3: Powder XRD patterns of the altered and unaltered zones of marble from Asia Minor (Turkey). Cal, Dol, and Qz mark the Bragg peaks arising from calcite, dolomite and quartz, respectively.

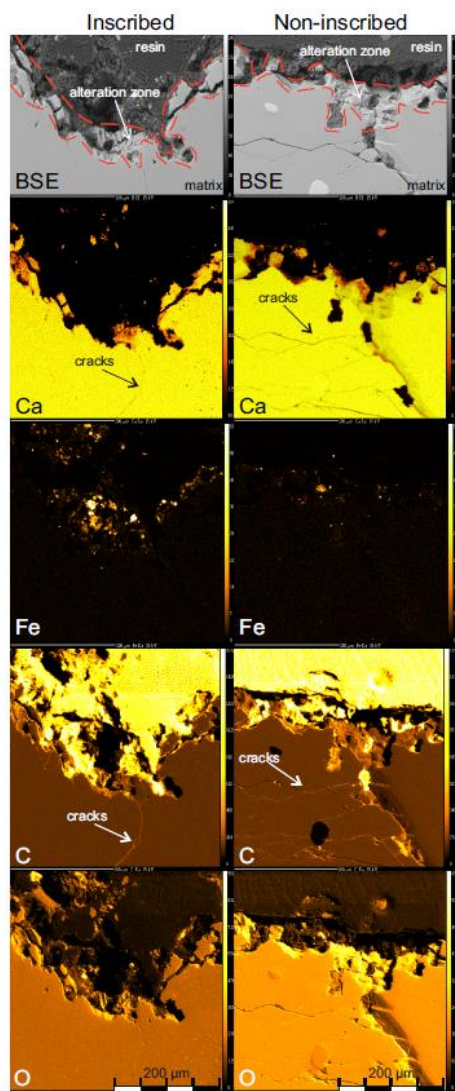


Figure 4: Backscattered electron (BSE) image and maps of selected elements of a polished cross section of sample MaD1B (Hamburg) beneath and away from engraved letters. Dashed lines trace the altered surface layer.

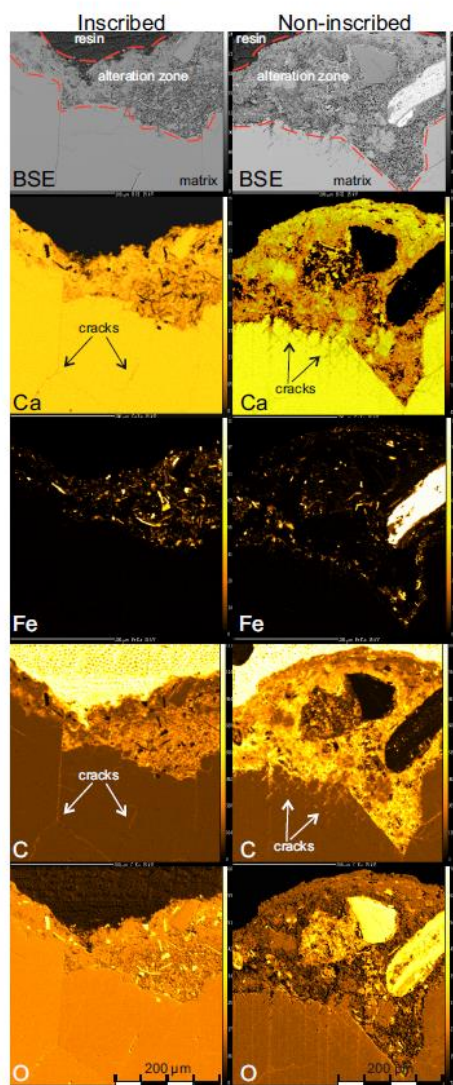


Figure 5: Backscattered electron (BSE) image and maps of selected elements of a polished cross section of sample AM_C1 (Asia Minor) beneath and away from engraved letters. Dashed lines trace the altered surface layer; note that the difference in the thickness of the altered layers is not statistically relevant.

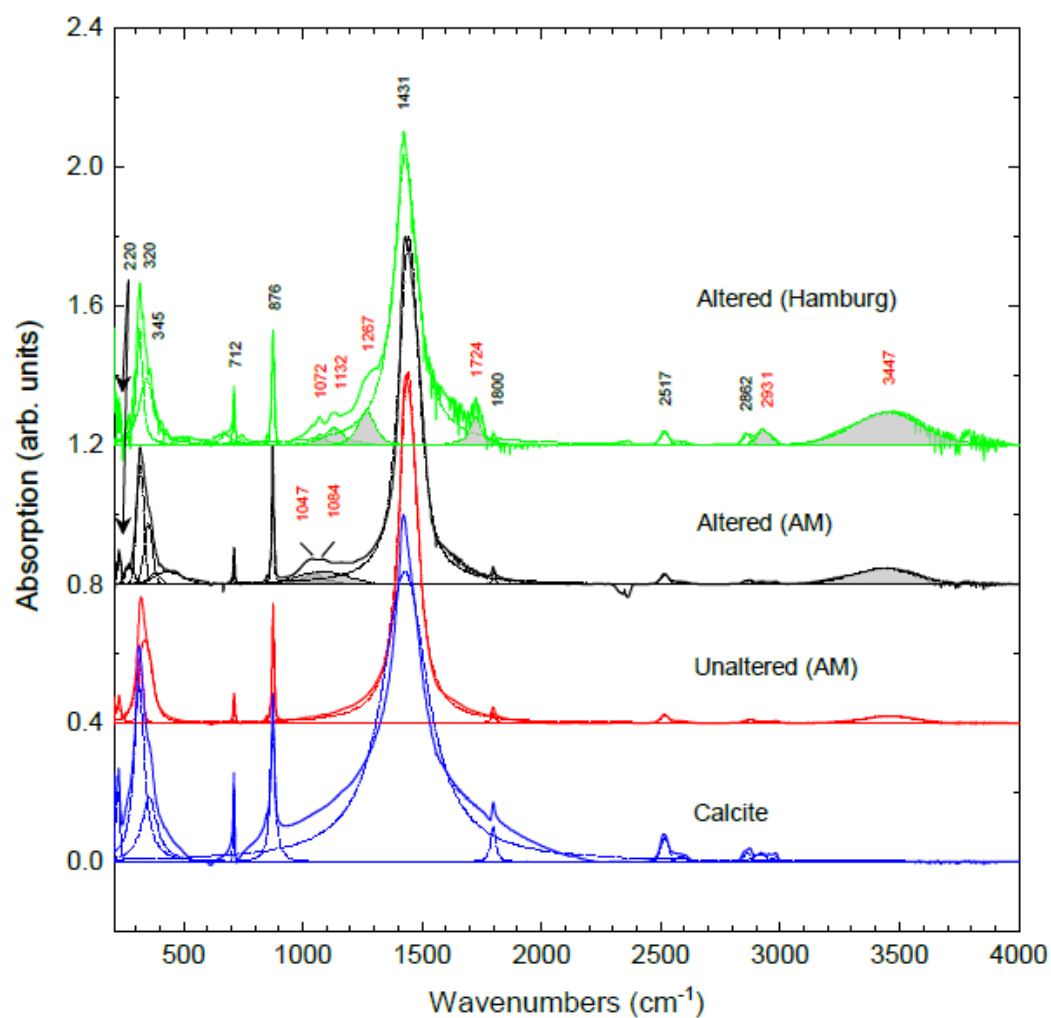


Figure 6: Infrared absorption spectra of altered areas of marbles from Ohlsdorf and Asia Minor (sample MaB1A and AM_C1, respectively), as well as of unaltered areas of the sample AM_C1, along with a reference calcite spectrum. Peak positions typical of calcite are marked in black, whilst the positions of extra peaks in the spectra from altered marble are given in red. The spectra were vertically offset for clarity.

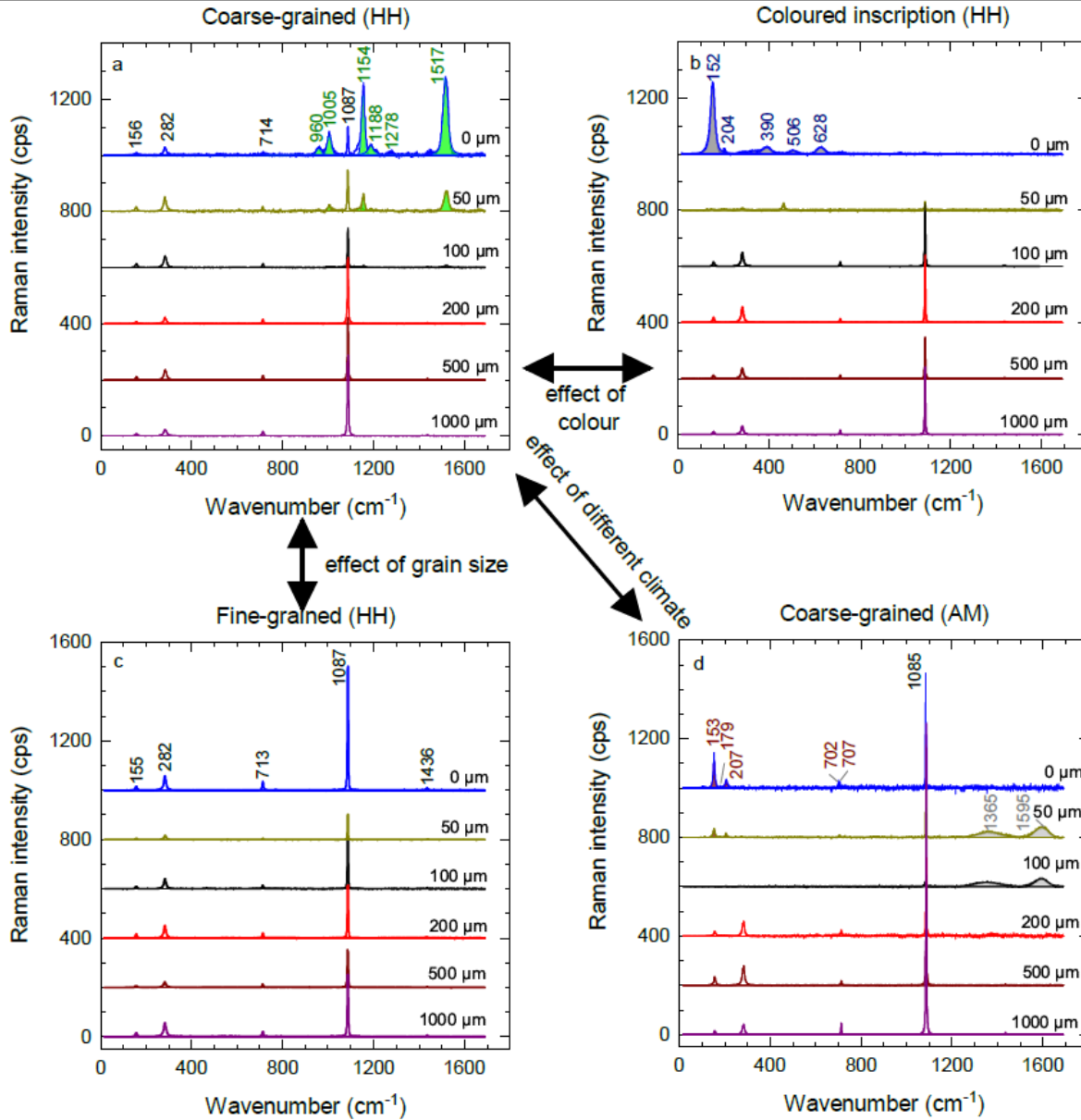


Figure 7: Raman spectra collected along line profiles beneath engravings of selected samples, revealing differences emerging from the effect of colour (a vs. b; sample MaD1B_C4L2 vs. MaD1A_C1L4, respectively), grain size (a vs. c; sample MaD1B_C4L2 vs. MaE1B_C2L1, respectively), and diverse environmental conditions (a vs. d; sample MaD1B_C4L2 vs. Am_C1L1, respectively). The shaded extra peaks in (a) are generated by lichen, those in (b) by anatase, and those in (d) by sooth. Sample AM_C1 (d) exhibits a typical spectrum of aragonite at the surface (0 μm) and of calcite for all other points. Black letters in (a) and (c) are indicative of the calcite vibrational modes, while those with green letters characterize additional minerals and compounds (see text for details). Additional peaks at the 0- μm level of (b) are attributed to TiO_2 , while those with red and grey colour in (d) are attributed to aragonite and carbonaceous material, respectively. Abbreviations in the figure: C is cut and, L is line. The spectra within the same plot were vertically offset for clarity.

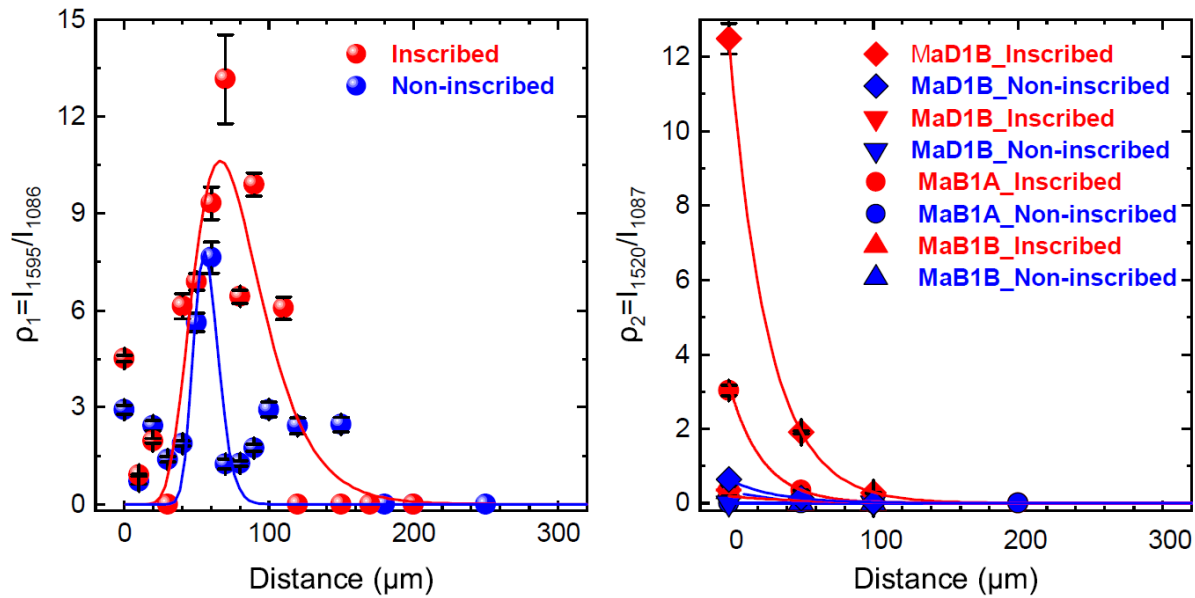


Figure 8: Intensity ratios of $I_{1595/1086}$ (a) and $I_{1520/1087}$ (b) plotted against the distance to the surface measured along the lines inferred in the legend beneath inscribed and non-inscribed regions of samples from Asia Minor (a) and Hamburg (b). Lines in (a) are lognormal fits, whereas lines in (b) are exponential decay fits to the corresponding data points.

Table 1: Sample designation, provenance, inscription age, mineral grain size, and letter colouring. The mineral-phase composition was determined by XRD and WD-EPMA (mineral abbreviations: Cal: calcite; Qz: quartz; Dol: dolomite; Ap: apatite; Fsp: feldspar; Py: pyrite; Fl: fluorite).

Sample	Location	Inscription age	Grain size	Coloured	Mineral inventory	
					Major minerals	Accessory minerals
AM	Asia Minor (W Turkey)	At least 2000 years ago	Medium-to coarse	No	Cal ± Qz ± Dol ^a	Ap ± mica ± Fsp ± Py ^a
MaB1	Hamburg, Germany	1940	Coarse	No	Cal ± Qz ± Dol ^b	Ap ± mica ^b
MaD1	Hamburg, Germany	1967	Coarse	Cross-section MaD1A	Cal ± Qz ± Dol ^b	Ap ^b
MaE1	Hamburg, Germany	1943	Fine	No	Cal ± Qz ± Dol ^b	Ap ± Fl ^b

^a The mineral composition of the altered and unaltered areas regarding the major minerals is the same, while Py and Ap could be detected only in the unaltered bulk and mica only in the alteration zone. Fsp appears in both cases.

^b The mineralogy of the altered and unaltered areas is the same regarding the major minerals. Accessory minerals could be found solely in the unaltered bulk as inclusions.

Table 2: Average chemical composition of the studied samples from Asia Minor (AM_C1) and from the cemetery of Ohlsdorf (Hamburg, Germany) in oxides weight per cent (wt.%), determined by WD-EPMA. Abbreviations in the table: AZ: alteration zone; n.d.: not determined; C1, 4: cut 1, 4, respectively.

	AM_C1				MaD1B_C4			MaE1B_C1		
	1/1 -1/5	Matrix	AZ (inscr.)	AZ (non-inscr.)	Matrix	AZ (inscr.)	AZ (non-inscr.)	Matrix	AZ (inscr.)	AZ (non-inscr.)
SiO ₂	0.22(11)	0.10(24)	6(5)	5(6)	0.11(20)	0.06(7)	0.01(3)	0.04(11)	0.03(5)	n.d.
Al ₂ O ₃	0.07(15)	0.04(22)	2(3)	1(2)	n.d.	0.04(8)	0.01(2)	n.d.	n.d.	n.d.
FeO	0.010(23)	0.001(7)	1(1)	0.4(8)	n.d.	0.01(3)	n.d.	n.d.	n.d.	n.d.
MgO	0.8(1)	0.9(4)	0.7(4)	0.6(6)	1.1(3)	1(1)	0.7(6)	0.26(5)	0.37(15)	0.45(1)
CaO	58(1)	53.6(9)	43(9)	42(10)	54(1)	53(2)	53.8(8)	55(1)	55(2)	54(3)
Na ₂ O	n.d.	n.d.	0.11(12)	0.06(9)	n.d.	0.008(22)	n.d.	n.d.	n.d.	n.d.
K ₂ O	n.d.	n.d.	0.3(4)	0.2(4)	n.d.	n.d.	n.d.	n.d.	n.d.	n.d.
P ₂ O ₅	1.2(3)	1.00(7)	1.5(3)	1.3(2)	1.08(7)	1.02(3)	1.04(5)	1.05(5)	1.02(6)	1.02(5)
SO ₂	0.008(18)	0.001(8)	0.22(9)	0.23(4)	0.001(6)	0.05(9)	0.08(12)	n.d.	0.03(8)	n.d.
Cl	0.005(10)	n.d.	0.14(10)	0.22(13)	n.d.	0.014(19)	n.d.	n.d.	0.004(11)	0.013(23)
As ₂ O ₃	n.d.	n.d.	n.d.	n.d.	n.d.	n.d.	n.d.	n.d.	n.d.	n.d.
SrO	n.d.	n.d.	n.d.	n.d.	n.d.	n.d.	n.d.	n.d.	n.d.	n.d.
BaO	n.d.	n.d.	n.d.	n.d.	n.d.	n.d.	n.d.	n.d.	n.d.	n.d.
F	n.d.	1(3)	1(3)	1(2)	0.1(4)	n.d.	0.05(13)	0.11(21)	0.12(14)	n.d.
Sum _(init.)	60.7(8)	57(3)	56(5)	52(2)	57(1)	56(2)	56(1)	57(2)	56(2)	56(3)
O=F+Cl	0.001(2)	0.5(13)	0.4(10)	0.3(9)	0.04(16)	0.003(4)	0.02(5)	0.05(9)	0.05(6)	0.003(5)
Sum _(calc.)	60.7(8)	56(2)	56(4)	51(3)	57(1)	56(2)	56(1)	57(1)	56(2)	56(2)
Mg/Ca	0.012(2)	0.016(6)	0.016(13)	0.016(26)	0.017(5)	0.018(17)	0.011(1)	0.0040(7)	0.006(2)	0.007(2)
CaO/Sum	0.961(1)	0.95(3)	0.78(15)	0.82(18)	0.959(8)	0.958(17)	0.966(9)	0.975(3)	0.973(3)	0.973(2)
P ₂ O ₅ /Sum	0.021(6)	0.018(1)	0.028(7)	0.025(5)	0.019(1)	0.0182(7)	0.019(1)	0.0185(8)	0.0182(7)	0.0183(6)

B.b. Supplementary material (<https://doi.org/10.5194/ejm-33-189-2021-supplement>)

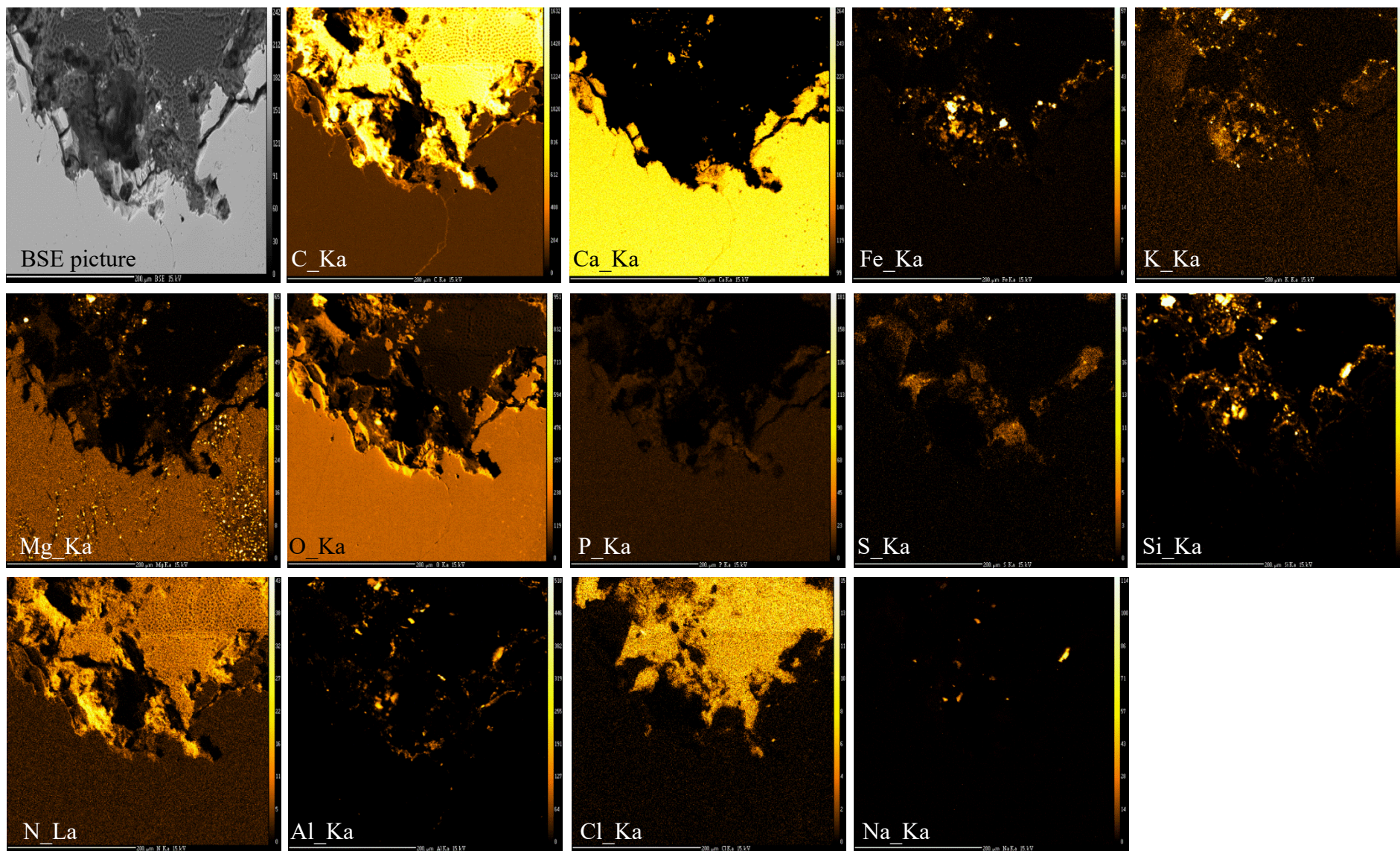


Figure S1: Backscattered electron (BSE) image and element maps of a polished cross-section of sample MaD1B (Hamburg) beneath an engraved letter.

UNDERSTANDING WRITTEN ARTEFACTS ON ROCK-BASE SUPPORTS AT THE ATOMIC-SCALE LEVEL: WEATHERING AND CRYSTAL CHEMISTRY OF THE ROCK-FORMING MINERALS

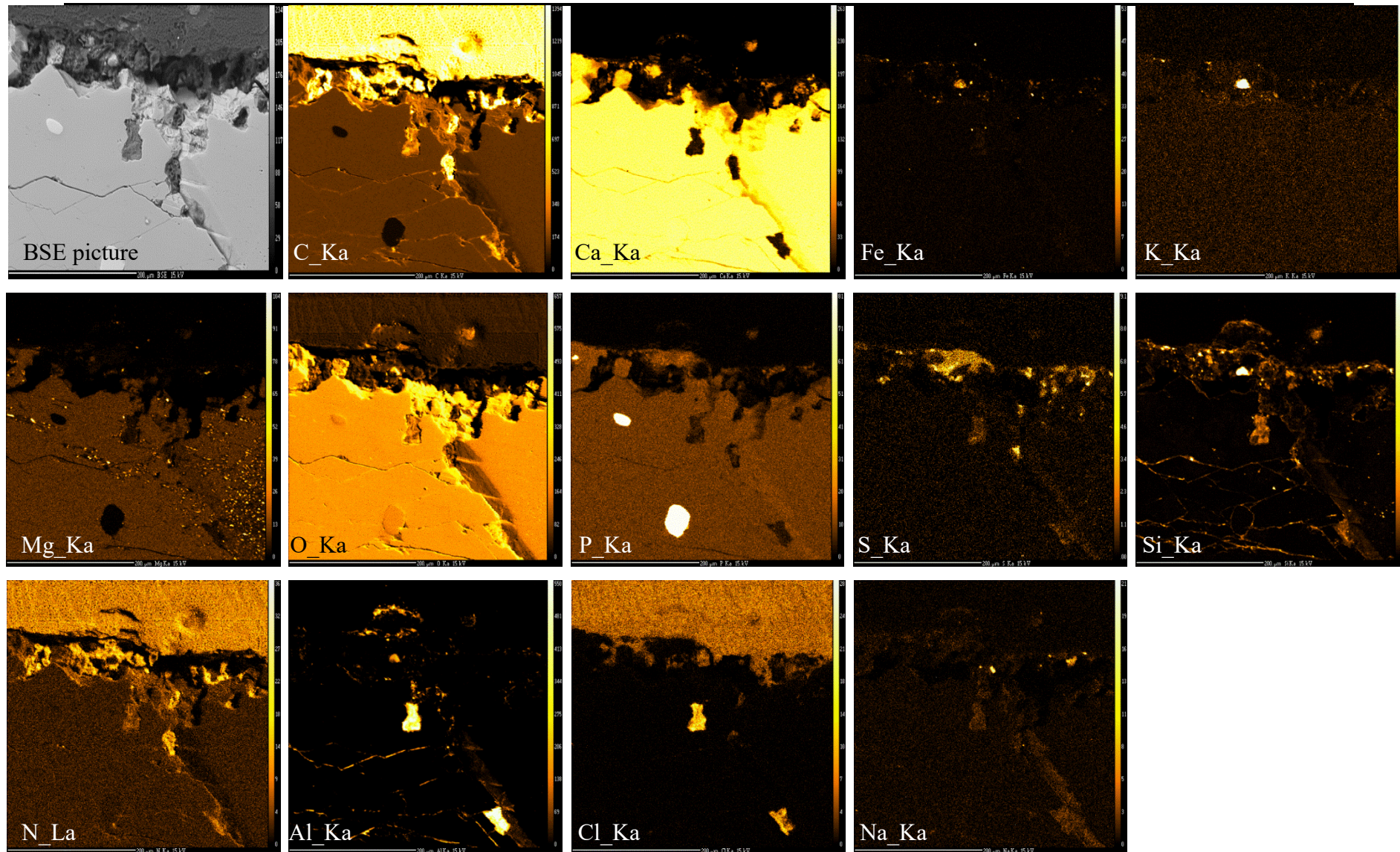


Figure S2: Backscattered electron (BSE) image and element maps of a polished cross-section of sample MaD1B (Hamburg) beneath a non-inscribed area.

UNDERSTANDING WRITTEN ARTEFACTS ON ROCK-BASE SUPPORTS AT THE ATOMIC-SCALE LEVEL: WEATHERING AND CRYSTAL CHEMISTRY OF THE ROCK-FORMING MINERALS

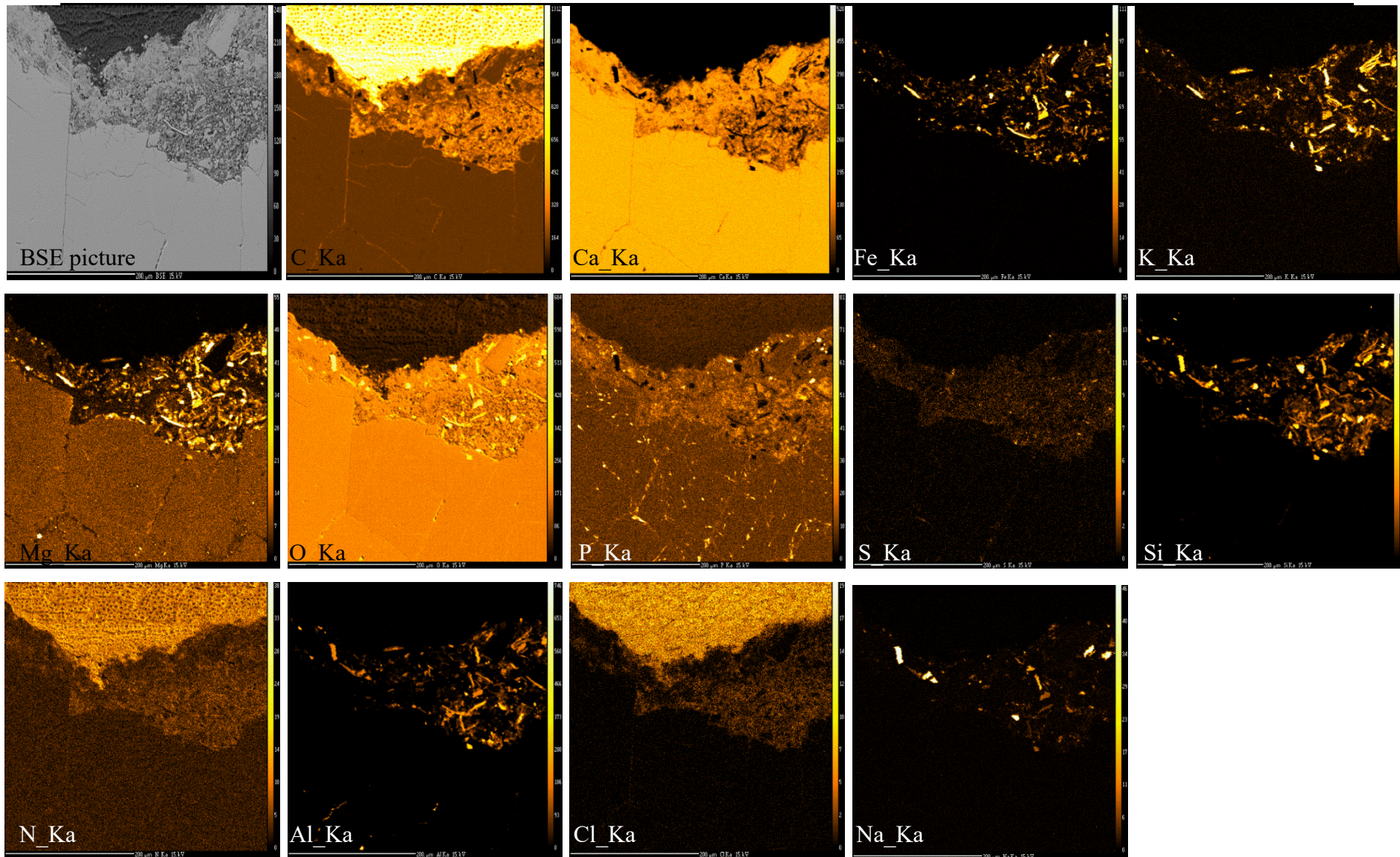


Figure S3: Backscattered electron (BSE) image and element maps of a polished cross section of sample AM_C1 (Asia Minor) beneath an inscription.

UNDERSTANDING WRITTEN ARTEFACTS ON ROCK-BASE SUPPORTS AT THE ATOMIC-SCALE LEVEL: WEATHERING AND CRYSTAL CHEMISTRY OF THE ROCK-FORMING MINERALS

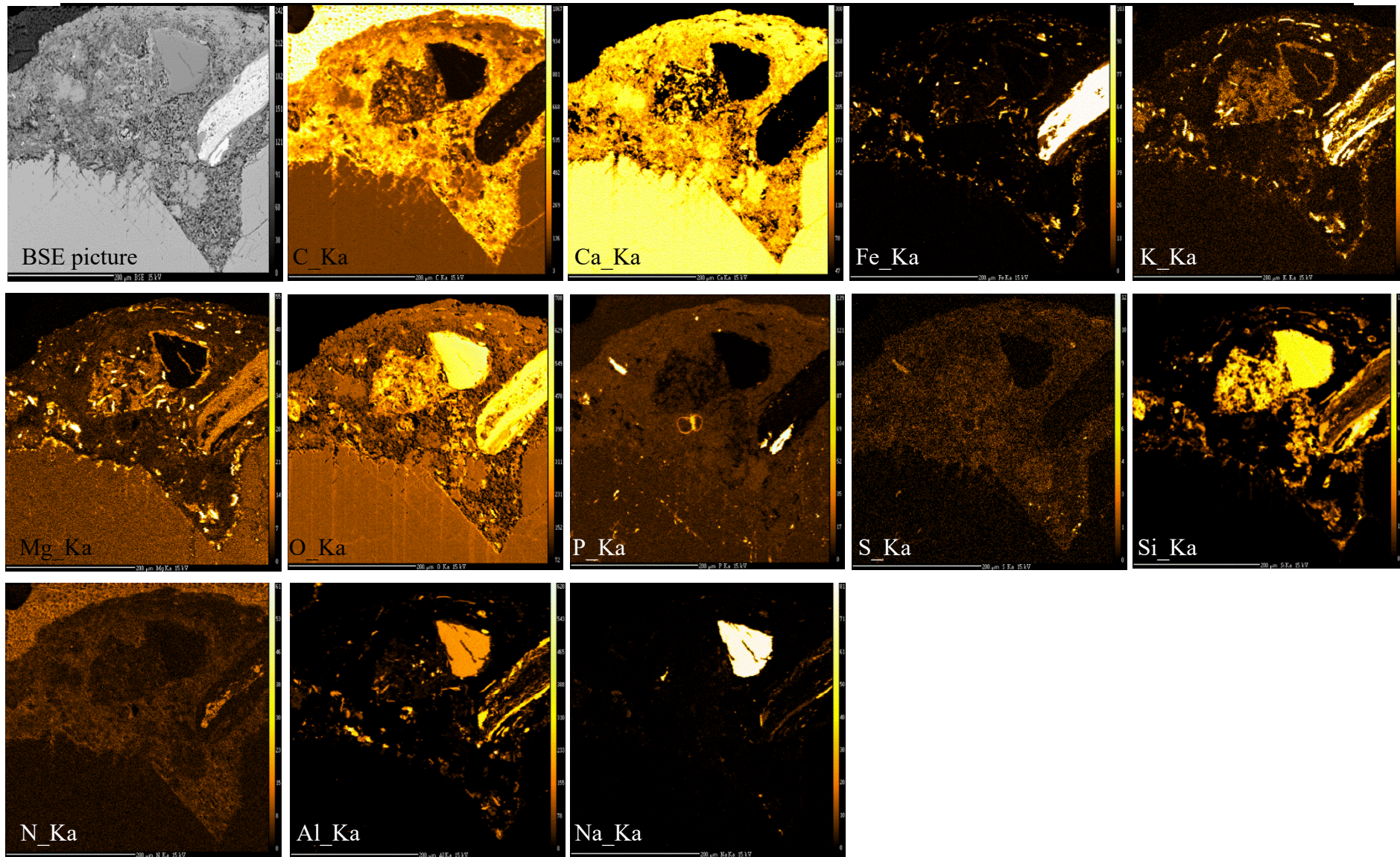


Figure S4: Backscattered electron (BSE) image and element maps of a polished cross section of sample AM_C1 (Asia Minor) away from an inscription.

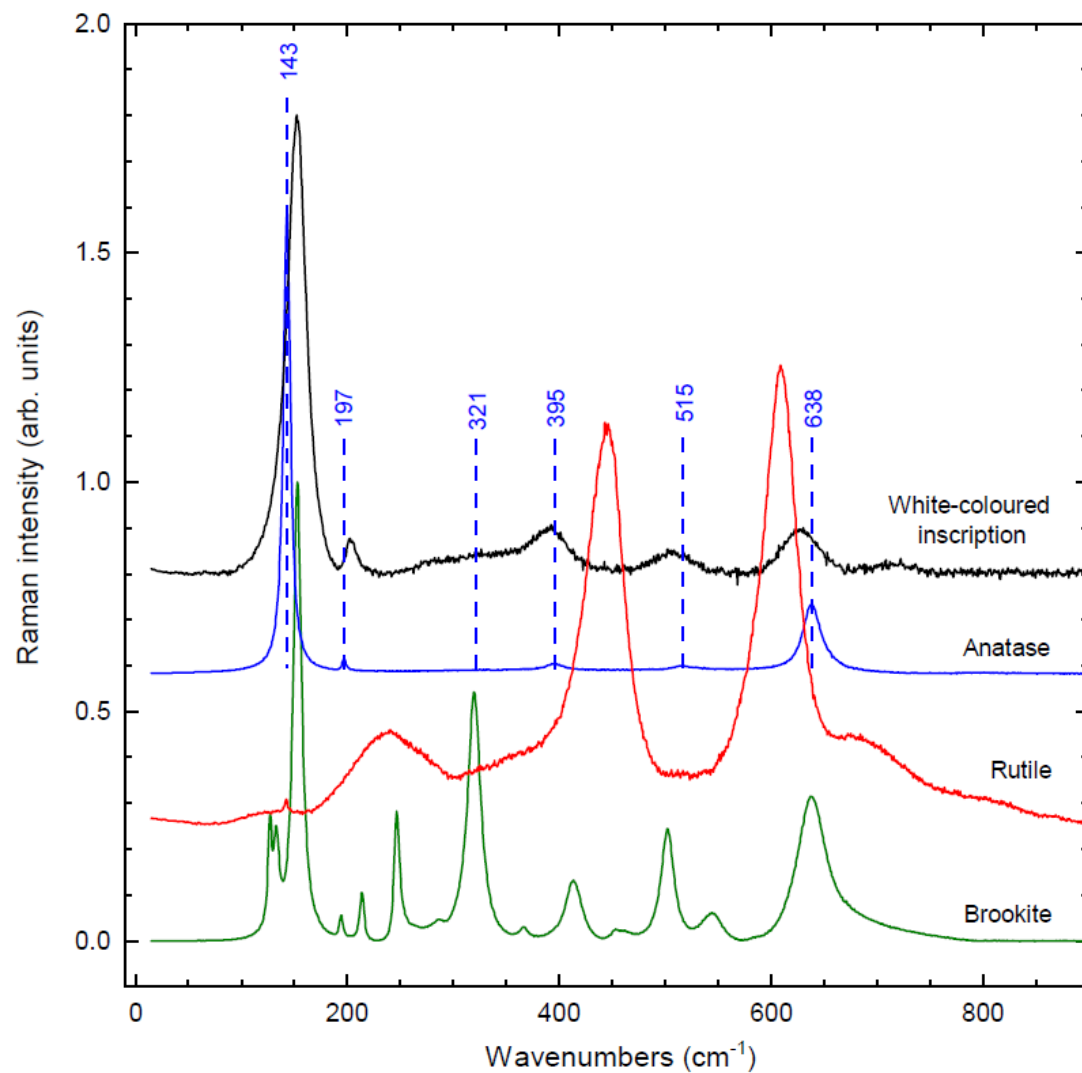


Figure S5: Raman spectra of the three TiO_2 polymorphs: anatase, rutile and brookite, along with the Raman spectrum of the superficial layer of the white-coloured engraved letter on coarse-grained gravestones from Ohlsdorf. For clarity, the spectra were normalized to the height of the strongest peak and vertically offset. The blue dashed lines represent the six characteristic Raman peaks of well-crystallized anatase.

C. Publication 2

C.a. Non-destructive determination of the biotite crystal chemistry using Raman spectroscopy: how far we can go?

Non-destructive determination of the biotite crystal chemistry using Raman spectroscopy: how far we can go?

Stylianos Aspiotis^{1,*}, Jochen Schlueter², Günther J. Redhammer³, Borianna Mihailova¹

¹Fachbereich Erdsystemwissenschaften, Universität Hamburg, Grindelallee 48, 20146 Hamburg, email: stylianos.aspiotis@uni-hamburg.de, email: borianna.mihailova@uni-hamburg.de

²Museum der Natur Hamburg-Mineralogie, Leibniz-Institut zur Analyse des Biodiversitätswandels (LIB), Grindelallee 48, 20146 Hamburg, email: jochen.schlueter@uni-hamburg.de

³Fachbereich Chemie und Physik der Materialien, Paris-Lodron Universität Salzburg, 5020 Salzburg, Austria, email: guenther.redhammer@plus.ac.at

*Correspondence to: Stylianos Aspiotis (stylianos.aspiotis@uni-hamburg.de)

Keywords: biotite, Raman spectroscopy, electron microprobe analysis, crystal chemistry, cultural heritage

Abstract

Raman spectroscopy combined with electron microprobe analysis as well as Mössbauer spectroscopy was applied to a series of 18 samples along the phlogopite ($\text{KMg}_3\text{AlSi}_3\text{O}_{10}(\text{OH})_2$) - annite ($\text{KFe}^{2+}_3\text{AlSi}_3\text{O}_{10}(\text{OH})_2$) join to establish a truly non-destructive method for crystallochemical characterization of biotite ($\text{A}_1\text{M}_3\text{T}_4\text{O}_{10}\text{X}_2$, $\text{M}_3 = \text{M1M2M2}$). The Raman scattering arising from the framework ($15\text{-}1215\text{ cm}^{-1}$) and OH-stretching phonon modes ($3000\text{-}3900\text{ cm}^{-1}$) was used to build up correlation trends between the Raman spectral features and crystal chemistry of biotite. We show that: (a) the contents of $^{\text{M}}\text{Mg}$, $^{\text{M}}\text{Fe}^{2+}$, and $^{\text{M}}\text{Fe}^{3+}$ contents can be quantified with a relative error of $\sim 6\%$, $\sim 6\%$, and $\sim 8\%$, respectively, by combining the integrated intensities of the OH-stretching peaks assigned to various M1M2M2 local configurations with the wavenumber of the MO_6 vibrational mode near 190 cm^{-1} ; (b) the $^{\text{M}}\text{Ti}$ content can be estimated from the peak position and FWHM of the second strongest TO_4 -ring mode at $\sim 680\text{ cm}^{-1}$, with a precision of 22% ; (c) the content of $^{\text{T}}\text{Si}$ can be estimated from the position of the second peak related to TO_4 -ring vibrations near 650 cm^{-1} ; (d) for phlogopite the $^{\text{T}}\text{Al}$ content can indirectly be calculated by knowing the amount of $^{\text{T}}\text{Si}$, whereas for annite it is hindered by plausible presence of $^{\text{T}}\text{Fe}^{3+}$; (e) the $^{\text{A}}\text{K}$ content can be quantified by the position of the peak generated by T-O_b-T bond stretching-and-bending vibration at $\sim 730\text{ cm}^{-1}$; (f) interlayer-deficient biotites and F-rich phlogopite can be identified via their unique OH-stretching Raman peaks around 3570 cm^{-1} and 3695 cm^{-1} , respectively. Our results show a potential tool for non-destructive quantitative estimations of the major (Mg, Fe, Si, Al, K) and minor (Ti) elements of the crystal chemistry of the biotite mineral group by using a non-destructive technique such as Raman spectroscopy, although its sensitivity is generally lower than that of electron microprobe analysis and therefore cannot detect trace elements. This is fundamental within the framework of cultural heritage where samples cannot be powdered or disassembled.

1 Introduction

Phyllosilicates can be found in a variety of cultural heritage objects such as clay tablets (e.g. Uchida et al., 2015), seals (Zazoff, 1983), earth pigments (e.g. Hradil et al., 2011; Corradini et al., 2021), blotting sand (e.g. Milke, 2012), archaeological decoration-related ceramics (e.g. Bersani and Lottici, 2016; El Halim et al., 2018), inscribed gems (e.g. Wang et al., 2013; Bersani and Lottici, 2016; Mihailova et al., 2021, and references therein), and in general as weathering products on the surface of common rock-forming silicate minerals (e.g. Velbel, 1993). To achieve a detailed insight into the locality and provenance of such cultural heritage objects (e.g. Bersani and Lottici, 2016; Mihailova et al., 2021), the determination of the mineral/phase composition as well as of the crystal chemistry within each single mineral constituent is necessary.

Commonly, the crystallochemical characterization of minerals is carried out through wavelength-dispersive electron microprobe analysis (WD-EMPA) and X-ray diffraction (XRD). However, such analytical methods require special sample preparation, which is highly undesirable or even prohibitive from the viewpoint of cultural heritage, due to the uniqueness of the examined sample. X-ray fluorescence (XRF) reflection is a well-known method for non-destructive chemical characterization of samples, but the final output is just the average chemical composition of the studied object expressed in oxide weight percent (wt. %), without any information about the chemistry of the individual mineral phases inside the cultural-heritage object. Besides, the detection of light element-containing mineral species, for instance H-, C-, and B-bearing, is not viable by XRF. Consequently, alternative, non-invasive, preparation-free methods such as Raman spectroscopy that can solve such challenges are becoming increasingly popular among the scientific community. The biggest advantage of Raman spectroscopy over other non-destructive analytical methods is that it can distinguish between different mineral phases within the same rock. At the same time, the exact elemental distribution within each structure type can be determined, as vibrational phonon modes are sensitive to both structure and chemistry (e.g. Bendel and Schmidt, 2008; Prencipe et al., 2012; Watenphul et al., 2016b; Waesermann et al., 2020). Furthermore, the overall roughness of the surface does not interfere with analysis, because the use of a microscope allows for focusing down to 1-2 μm .

Towards a truly non-destructive crystallochemical characterization of rock-based written artefacts containing phyllosilicates, we have decided to study a series of natural biotite samples by WD-EMPA and Raman spectroscopy, because this type of layered silicates can form a complete solid solution between the magnesian endmember phlogopite ($\text{KMg}_3\text{AlSi}_3\text{O}_{10}(\text{OH})_2$) and ferrous endmember annite ($\text{KFe}^{2+}_3\text{AlSi}_3\text{O}_{10}(\text{OH})_2$) and thus can serve as model phyllosilicate group with interlayer cations.

Biotite is a trioctahedral mica with the general formula $^{\text{A}}\text{K}^{\text{M}}(\text{Mg}_{3-x}\text{Fe}_x^{2+})^{\text{T}}(\text{AlSi}_3)\text{O}_{10}^{\text{X}}(\text{OH},\text{F})_2$, where the A-site can accommodate additional minor or trace quantities of Na^+ , \square (vacancy), Ca^{2+} and Ba^{2+} ; M refers to the octahedrally coordinated cationic site, where minor amounts of Fe^{3+} , Al^{3+} , Ti^{4+} , and Mn^{2+} , and trace amounts of Cr^{3+} , Zn^{2+} , Li^+ and \square can be found; T refers to the tetrahedrally coordinated cationic site, which can also incorporate Fe^{3+} as a minor element; and X denotes the anionic site, which can be also occupied by minor or trace quantities of Cl^- and O^{2-} . Biotite crystallizes in monoclinic $C2/m$ symmetry and its structure consists of an octahedral sheet (O_s) sandwiched between two tetrahedral sheets (T_s). The T_s - O_s - T_s layers are intercalated by A-site monovalent cations (see Fig. 1), resulting in the T_s - O_s - T_s -A stacking sequence typical of biotites. Each tetrahedron shares three O atoms (bridging O atoms; O_b) with adjacent tetrahedra, thus forming a quasi-two-dimensional system of six-membered rings. The tetrahedral non-bridging O (O_{nb}) is shared with three octahedrally coordinated

M cations, which are distributed between two crystallographic sites, *M1* and *M2*, and each *M1M2M2* triplet is bonded to two X-site anions. Based on single-crystal XRD analysis, it has been established that *M2* is the preferred site for Ti^{4+} and Fe^{3+} , whilst divalent M cations as well as Al^{3+} are randomly partitioned on both *M1*- and *M2*-sites (e.g. Redhammer et al., 2000; Scordari et al., 2006; Lacalamita et al., 2011). Finally, A-site cations are coupled with six O_b of the tetrahedral sheets.

So far, the substitutional mechanisms of biotites with various chemical compositions have been thoroughly studied by single-crystal XRD, EMPA and Mössbauer spectroscopy (e.g. Brigatti et al., 2000, Redhammer et al., 2002; Scordari et al., 2006; Lacalamita et al., 2011; Schingaro et al., 2013). In addition, Fourier-transform infrared (FTIR) and Raman spectral features of biotites together with peak assignment of the framework vibrational modes ($15\text{-}1215\text{ cm}^{-1}$) and OH bond-stretching modes ($3550\text{-}3750\text{ cm}^{-1}$) have been reported over the last three decades (e.g. McKeown et al., 1999; Tutti and Lazor, 2008; Wang et al., 2015; Singha and Singh, 2016). Much attention has been given to the FTIR analysis of the OH-stretching peaks and their relation to different chemical configurations of *M1M2M2* triplet sharing $^X(\text{OH})^-$, such as MgMgMg-OH^- at 3709 cm^{-1} , $\text{MgMgFe}^{2+}\text{-OH}^-$ at $\sim 3695\text{ cm}^{-1}$, $\text{MgMgFe}^{3+}\text{-OH}^-$ near $3660\text{-}3670\text{ cm}^{-1}$, $\text{MgFe}^{2+}\text{Fe}^{2+}\text{-OH}^-$ near $3666\text{-}3670\text{ cm}^{-1}$, and $\text{Fe}^{2+}\text{Fe}^{2+}\text{Fe}^{2+}\text{-OH}^-$ near $3640\text{-}3665\text{ cm}^{-1}$ (e.g. Redhammer et al., 2000; Scordari et al., 2012; Schingaro et al., 2013, and references therein). Recently, Wang et al. (2015) suggested a linear dependence of the positions of specific Raman peaks in the spectral ranges $750\text{-}780$ and $3500\text{-}3800\text{ cm}^{-1}$ on the $\text{Fe}^{2+}/(\text{Mg}+\text{Fe}^{2+})$ ratio, although, they have neither separated ^TFe and ^MFe nor discriminated Fe^{2+} from Fe^{3+} . Moreover, Tlili et al. (1989) postulated that the Raman peak of di- and trioctahedral micas at $\sim 195\text{ cm}^{-1}$ is sensitive to ^MAl and ^TAl content, since it shifts towards higher wavenumbers with increasing both tetrahedrally and octahedrally coordinated Al content, however the number of biotite samples (a total of 4) used in this study was insufficient to quantify the trend along the phlogopite-annite join.

In the present paper, we report the results of comprehensive Raman spectroscopic analyses combined with EMP and Mössbauer spectroscopy on 18 biotites with various chemical compositions, covering the whole biotite solid-solution series, aiming at establishing quantitative relationships between Raman signals (peak positions, integrated intensities and full widths at half maximum; FWHMs) and the crystallochemical composition of the biotite-group minerals. The goals were (i) to verify whether the Raman scattering arising from the framework and OH bond-stretching vibrations can assist in identifying biotite-group minerals through an entirely non-destructive analytical technique, (ii) to clarify the effect of grain orientation on the Raman signals, and (iii) to understand the behavior of the major as well as minor elements (for instance Ti) within each crystallographic site as a function of the Raman signals, since they are significant crystallochemical markers that can indicate locality; a critical aspect in the field of cultural heritage.

2 Materials and methods

2.1 Samples

The biotite minerals studied here are from the mineral collection of the Mineralogical Museum, University of Hamburg. Details about their provenance, chemical formulae, and names according to the IMA nomenclature (Rieder et al., 1998) are given in Table 1.

2.2 Analytical methods

Wavelength-dispersive electron microprobe analysis (WD-EMPA)

EMP analyses of biotite were performed with a Cameca SX-100 SEM (Scanning Electron Microscope) system with a wavelength-dispersive detector by using the following operating conditions: 15kV electron accelerating voltage, 20 nA beam current and a ~10 μm beam-spot size on the sample surface. The employed standards were: LiF for F, albite for Na, MgO for Mg, corundum for Al, andradite for Si, Ca and Fe, vanadinite for Cl, orthoclase for K, MnTiO₃ for Ti and Mn, NiO for Ni, olivenite for Cu, Pb-containing glass for Zn, SrTiO₃ for Sr, Ba-containing for Ba and Cr₂O₃ for Cr. The acquisition times were 20 s for Mg, Al, Si, K, Ca, and Fe; 30 s for Na, Cl, and Ti; 60s for Mn, Ni, Cu, Zn, Sr, Ba, and Cr; and 120s for F. EMP data were acquired on 50-100 separate spots on each sample and then averaged to yield the chemical compositions and statistical standard deviations (σ) presented in Table S1. The content of hydroxyl groups, as well of tetrahedrally and octahedrally coordinated Fe³⁺ (^TFe³⁺ and ^MFe³⁺, respectively) was calculated using the charge-balance approach of Li et al. (2020), who developed a machine learning method based on principal components regression (PCR). This method was built up on a dataset of more than 150 well-characterized biotite reference samples whose crystallochemical data have previously been refined. Biotite samples have randomly been categorized into two groups, namely the training and the test set, where the latter one has been used to testify the performance of the model and to establish a linear regression coefficient matrix. Based on the derived matrix the atomic proportions of elements, including ^TFe³⁺, ^MFe²⁺, ^MFe³⁺, ^XOH, and ^XO²⁻, can be precisely calculated with $R^2 > 0.95$ for the major elements. We have assumed that the analysed biotite samples are lithium-free, which did not affect the quality of the calculated chemical formulae, as pointed out by Li et al. (2020). Elements, whose standard deviation was greater than the average content, were not included in the calculated chemical formulae. Moreover, biotite formulae were calculated by assuming that the valence state of Ti is 4+, after Scordari et al. (2013).

Mössbauer spectroscopy

Selected biotite samples were further subjected to ⁵⁷Fe Mössbauer spectroscopy to verify the fraction of Fe³⁺ cations and their distribution over the *T* and *M* sites, using the set-up available at the University of Salzburg, Austria. Data were acquired at room temperature using an apparatus in a horizontal arrangement (⁵⁷Fe Co/Rh single-line thin source, constant acceleration mode with symmetric triangular velocity shape, multi-channel analyser with 1024 channels, and regular velocity calibration against metallic Fe). Absorbers were prepared with a nominal density of about 5mg Fe/cm² with the mica sample being filled into Cu-rings, 10 mm inner diameter and 2 mm in depth and fixed with epoxy resin. The spectra were recorded with the absorber being oriented at the so-called magic angle (54°) to the source to avoid texture effects. Data evaluation was done with the RECOIL program suite, using the Voigt based hyperfine distribution approach, for details on data evaluation see Redhammer et al. (2005).

Raman spectroscopy

Raman spectra were collected with a Horiba Jobin-Yvon T64000 triple-monochromator system coupled with a Symphony LN₂-cooled CCD detector and an Olympus BH41 confocal microscope with a 50× long working distance objective. Green line ($\lambda = 514.532$ nm) of a Coherent Innova 90C FreD Ar⁺ laser was used to excite the Raman scattering. The spectral resolution achieved with the green laser was ~2 cm⁻¹, while the instrumental peak position accuracy was ~0.35 cm⁻¹. The Raman

spectrometer was calibrated using the 520.5 cm⁻¹ line of a silicon standard wafer. The laser-spot diameter on the sample surface was ~2 μm, while the laser power on the sample surface was 7.9 mW. The spectra were collected in the spectral ranges 15-1215 and 3000-3900 cm⁻¹, with exposure times varying between 20 and 60 s and averaging 10 to 30 repeated acquisitions to improve the signal-to-noise ratio. The measured Raman spectra were baseline corrected with a polynomial function, temperature reduced to account for the Bose–Einstein distribution of phonons, and fitted with pseudo-Voigt peak-shape functions $PV = \mu L + (1-\mu)G$ (L and G stand for Lorentz and Gauss peak-shape functions, respectively, while μ is a variable weight coefficient) to define the peak positions ω , FWHMs, and integrated intensities I . The usage of the OriginPro 2019 software package facilitated the Raman data evaluation.

In general, Raman peak intensities depend on the crystal orientation as well as on the mutual orientation of the polarization of the incident (\mathbf{E}_i) and scattered light (\mathbf{E}_s). Considering that in trioctahedral micas such as biotites the OH groups are perpendicular to the cleavage plane (Libowitzky and Beran, 2004), i.e. the crystallographic (001) plane, parallel-polarized ($\mathbf{E}_i \parallel \mathbf{E}_s$) and cross-polarized ($\mathbf{E}_i \perp \mathbf{E}_s$) Raman spectra were collected in backscattered geometry from two different orientations of the biotite crystals, with \mathbf{E}_i parallel (Fig. 1a) and perpendicular to the cleavage plane (Fig. 1b). This results in four scattering geometries (given in Porto's notation): horizontal parallel-polarized $\bar{z}(yy)z$, horizontal cross-polarized $\bar{z}(xy)z$, vertical parallel-polarized $\bar{y}(zz)y$, and vertical cross-polarized $\bar{y}(xz)y$ geometries, with z perpendicular to the (001) plane and $x \perp y \perp z$.

3 Results

3.1 Chemical composition from wavelength-dispersive EMPA and Mössbauer spectroscopy

The chemical composition in oxide wt.% of the studied biotites are reported in supplementary Table S1. The relatively low standard deviations reveal an overall homogenous distribution of major and minor elements among each studied biotite; i.e. the crystals are not chemically zoned. The EMPA results were initially checked for too low or too high oxide totals in wt.%, which should typically vary between 93.5 and 98.5 wt%, as the H₂O content varies between 1.5-4.5 wt.% (e.g. Brigatti et al., 2000, 2001; Righter et al., 2002; Laurora et al., 2007; Scordari et al., 2012; Brigatti et al., 2015). Sample B3, seemingly a tetra-ferri-containing (OH)-rich fluorophlogopite, has oxide totals_{calc} of 85.7(2.4) wt.%, indicating surface defects/roughness, which in turn compromises the correct composition determined via EMPA. Therefore, the dataset of sample B3 was not taken into consideration while constructing calibration curves. On the other hand, high total oxides equal to 100 wt.%, can be explained by high F content such as in fluorophlogopite (e.g. Gianfagna et al., 2007; Scordari et al., 2013; Lacalamita et al., 2020). The fraction of trivalent iron and its distribution over the M and T sites for the samples B4, B13, B14, B17, B19, and B21 was derived from the Mössbauer spectra (see supplementary Table S2 and Fig. S1).

Following the procedures of the Excel spreadsheet by Li et al. (2020), the biotite chemical formulas were calculated in atoms per formula unit (apfu) (Table 1). As can be seen, the compositions of the studied biotites expand over the whole biotite solid-solution series with samples B1 (sodian F-rich phlogopite) and B21 (tetra-ferri and Ti-containing fluorannite) having the highest and lowest ^MMg content, respectively.

Mineral names are given following the analytical procedures described by Rieder et al. (1998) and provided in Table 1. Sample B18 was named magnesian interlayer-deficient annite rather than interlayer-deficient mica, as the cation partitioning

at the *M*-site resembles that of a typical magnesium-rich annite (e.g. Brigatti et al., 2015), while the K content lies between 0.6 and 0.85 apfu.

3.2 Raman scattering analysis

Effect of tetrahedral-octahedral layer stacking sequence in phyllosilicates

Various phyllosilicate mineral groups in a rock sample or a cultural-heritage object can straightforwardly be distinguished, based on their Raman spectra (Fig. 2). Indeed, compositional variations, stacking sequence of the tetrahedral and octahedral sheets as well as the presence or absence of interlayer species affect significantly the Raman spectra. The major differences in the Raman spectra of the main layered silicates (Fig. 2) are in the ranges 100-500 cm⁻¹, dominated by MO₆ vibrations, around 600-800 cm⁻¹, generated by TO₄-ring modes (i.e. T-O_b-T modes), as well as in the range 3500-3800 cm⁻¹ generated by OH-stretching vibrational modes (Tlili et al., 1989; McKeown et al., 1999; Lacalamita et al., 2020) and can be used to fingerprint the phyllosilicate mineral group. Particularly, the OH-stretching region is characterized by multiple Raman peaks in the case of 1:1 layer silicates [antigorite (Mg,Fe)₃Si₂O₅(OH)₄ and dickite Al₂Si₂O₅(OH)₄], whereas in 2:1 layer silicates with empty interlayer space [talc and pyrophyllite; Mg₃Si₄O₁₀(OH)₂ and Al₂Si₄O₁₀(OH)₂, respectively], there is only one sharp peak. If the interlayer space is filled by monovalent cations, as in the case of muscovite, biotite or illite (K_{0.65}(Al,Mg,Fe)₂(Si,Al)₄O₁₀(OH)₂), or by H₂O molecules along with mono-/divalent cations, as in the case vermiculite ((Mg,Fe³⁺,Al³⁺)₃(Al,Si)₄O₁₀(OH)₂·4H₂O), the OH stretching produces broad Raman peaks.

Group-theory considerations

According to group-theory analysis, the most common *C2/m* polytype of biotite shows a total of 63 optical phonon modes at the Γ point (Kroumova et al., 2003). Among them, 33 are IR active and 30 Raman active (see Table 2). The Raman active modes of biotite are of A_g and B_g symmetries and they have the following Raman tensor components:

$$A_g: \begin{pmatrix} a_{xx} & & a_{xz} \\ & a_{yy} & \\ a_{xz} & & a_{zz} \end{pmatrix} \text{ and } B_g: \begin{pmatrix} & a_{xy} & \\ a_{xy} & & a_{yz} \\ & a_{yz} & \end{pmatrix}.$$

Consequently, the parallel-polarized Raman spectra of oriented crystals will be generated only from the A_g modes, whereas depending on the orientation, both A_g and B_g modes can contribute to the cross-polarized spectra. In our case, the vertical parallel-polarized Raman spectra $\bar{y}(zz)y$ are determined from the *zz* component of the polarizability tensor α of the A_g mode, A_g(*a_{zz}*), while the vertical cross-polarized spectra $\bar{y}(xz)y$ are dominated by the A_g(*a_{xz}*). Accordingly, the horizontal parallel-polarized spectra $\bar{z}(yy)z$ are characterized by the A_g(*a_{yy}*) component, whilst the horizontal cross-polarized spectra $\bar{z}(xy)z$ by the B_g(*a_{xy}*) component. Given that the orientation of the binary *b* axis with respect to the laboratory coordinate axes (*x,y*) is usually unknown, A_g(*a_{xx}*) and B_g(*a_{zy}*) may also contribute to the horizontal parallel-polarized and vertical cross-polarized spectra, respectively.

Table 2 reveals that H atoms occupy the 4i Wyckoff position and generate 2A_g+B_g Raman active modes. Considerations of the directions of the atomic vector displacements via the Bilbao Crystallographic server (Kroumova et al., 2003) reveal that one A_g mode corresponds to the O-H bond stretching vibration perpendicular to the (001) plane, while one A_g and the B_g mode

are related to the O-H bond librational modes, with H⁺ motions within the (a,b) plane and causing a change in the M-O-H bond angle. Therefore, the presence of more than one Raman peaks in the OH-stretching region implies a chemical deviation from the endmember composition, due to different types of octahedrally coordinated cations bonded to OH groups. Such behavior has already been observed in other hydrous minerals like amphiboles and tourmalines (Leissner et al., 2015; Watenphul et al., 2016a; Hawthorne, 2016).

Effect of crystal orientation

As the structure of biotite-group minerals is strongly anisotropic, it is obvious that the Raman scattering can chiefly depend on the crystal orientation with regard to the polarization of the incident and scattered light. However, since *C2/m* is a nonpolar crystal class, the orientation of the biotite crystals will only influence the relative intensities, but not the Raman peak positions. Biotite grains, which are exposed on the sample surface and can be non-destructively probed by Raman spectroscopy, can be randomly oriented. Since the relative intensities of the Raman peaks depend on the crystal orientation with respect to the polarization of the incident and scattered light, Raman spectra collected from biotite grains within the same rock/cultural-heritage specimen may appear inconsistent at a first glance. Moreover, some of the Raman peaks may be suppressed in specific experimental geometry. Therefore, to clarify the effect of the grain orientation on the Raman spectra and identify Raman signals that can be resolved independently of the grain orientation, we have systematically measured representative biotite single crystals in different scattering geometries. Figure 3 presents the Raman spectra of a phlogopite measured in the four different scattering geometries specified above. It is apparent that parallel-polarized spectra are much stronger than the cross-polarized ones and hence the latter do not provide any additional information that is not included in the former. Therefore, A_g modes should dominate the spectra regardless of the crystal orientation. For the framework vibrations the $\bar{y}(zz)y$ spectrum differs considerably from the $\bar{z}(yy)z$, in accordance with the group-theory prediction ($a_{zz} \neq a_{yy}$). At the same time, although a_{xx} and a_{yy} are allowed to be different by symmetry constraints, in horizontal orientation $\bar{z}(yy)z$ Raman spectra remained practically the same upon rotation of the biotite samples around the laser beam direction, indicating that the a_{xx} and a_{yy} Raman tensor components are almost equal. The OH-stretching modes contribute only to the parallel-polarized spectra, generating a multi-component Raman band. The overall OH-stretching Raman scattering is stronger in $\bar{y}(zz)y$ than in $\bar{z}(yy)z$, but the relative intensities of band components are the same in both scattering geometries. Thus, regardless of selected orientation and induced photoluminescence, the strongest Raman peaks of biotite samples can be identified at wavenumbers close to 190, 650, 680, 730, 780, 1020 cm⁻¹ and between 3500-3800 cm⁻¹ and used for crystallochemical analysis.

Raman peak assignment and effect of chemistry

Figure 4 shows the characteristic Raman spectra of selected biotite samples with different Mg contents at the *M*-site. One can divide the Raman scattering into four spectral ranges according to the dominant atomic displacements: range I (15-600 cm⁻¹) dominated by octahedral vibrations; range II (600-800 cm⁻¹) dominated by TO₄-ring modes comprising vibrations of T-O_b-T linkages; range III (800-1215 cm⁻¹) generated by TO₄ stretching modes; and range IV (3500-3800 cm⁻¹) arising from OH-stretching modes.

The strongest Raman feature of spectral range I in both parallel-polarized spectra (Fig. 4) occurs near 190 cm⁻¹ for phlogopite and it shifts considerably towards lower wavenumbers for annite with ^MMg < 0.70 apfu (Figs. 5a and 6a). As in general $\omega \sim \sqrt{\frac{K}{\mu}}$ (K is the force constant and μ is the reduced mass of atoms participating in the mode) and $m_{\text{Fe}} > m_{\text{Mg}}$ while $K(\text{Fe}^{2+}\text{-O}) > K(\text{Mg-O})$, this trend indicates one-mode behavior of the mode near 190 cm⁻¹, due to the change in mass of the M cations (Chang and Mitra, 1971). In this case, only one peak can be observed corresponding to the mixed (Mg_{3-x}Fe_x) concentration at the M-site and whose ω lineally depends on the concentration x . Our experimental observations are in accordance with previous studies indicating that MO₆ vibrations contribute considerably to the Raman scattering below 600 cm⁻¹ (Loh, 1973; Tlili et al., 1989; McKeown et al., 1999; Tutti and Lazor, 2008). Moreover, the strong Raman scattering near 150 cm⁻¹ observed in monoclinic amphiboles shows the same trend of ω vs. ^MMg content (Waesermann et al. 2020), implying that this is a general feature of complex silicates containing strips of linked tetrahedral and octahedral sheets. Biotites are also similar to amphiboles (Waesermann et al. 2020) by the appearance of additional Raman scattering between 500-550 cm⁻¹ when ^MFe³⁺ is present (see $\bar{z}(yy)z$ spectra in Fig 4 and Table 1).

The spectral profile of range II changes in a rather complex way from one sample to another (Figs. 4 and S2) and can be fitted with up to four components, near 650, 680, 730 and 780 cm⁻¹. The Raman-active phonon modes near 650 and 680 cm⁻¹ produce strong peaks in both $\bar{z}(yy)z$ and $\bar{y}(zz)y$ geometries, but only the wavenumber of the former mode turned to be exclusively sensitive to T -site occupancy (see Fig. 7a). In fact, this is in accordance with the peak assignment by Tlili et al. (1989) and Lacalamita et al. (2020), attributing the peaks near 650 and 680 cm⁻¹ to Si-O_b-Al and Si-O_b-Si bond vibrations, respectively. Our analysis revealed that both ω_{680} and FWHM₆₈₀ are sensitive to ^MTi content (see Figs. 7c and 7e). Given that Ti occupies predominantly the $M2$ site, this result is in agreement with previous studies suggesting that the chemistry of the $M2$ site can affect the T-O_b-T vibrations (e.g. McKeown et al., 1999; Wang et al., 2015; Lacalamita et al., 2020). In addition, the Raman signal near 730 cm⁻¹, well-resolved in $\bar{z}(yy)z$ and $\bar{y}(zz)y$ spectra (see Figs. 3 and 4), tends to shift to higher wavenumbers in the presence of A -site vacancies (see Fig. 8a).

We have expected the TO₄ stretching modes in range III to be sensitive to the octahedral site occupancy, as in the case of Mg-Fe-Mn amphiboles (Waesermann et al., 2020); however, we were not able to establish a rational dependence of the spectral parameters of these modes on the chemistry neither at the M -site nor at T -site.

The reported observations for the framework phonon modes should be combined with the Raman scattering results arising from OH stretching modes to gain a detailed description of the entire biotite Raman spectrum and to comprehend its dependence on the site occupancy. As expected, range IV exhibits more than one peak generated by OH-stretching vibrations due to two-mode behavior, typical of complex hydrous silicates (Leissner et al., 2015; Watenphul et al., 2016a; Hawthorne, 2016). In such a case, more Raman peaks than those predicted by group-theory analysis can appear in the spectra, whose fractional intensities correlate with the composition x . This two-mode behavior of the O-H stretching phonon modes is caused by the perturbation of the $K(\text{O-H})$ force constant by the averaged M-O interactions in the surrounding triplet of MO₆ octahedra sharing oxygen atom with the X -site hydroxyl group, $\langle \delta K(M-O) \rangle$. Thus the OH-stretching wavenumber will be $\omega_{\text{OH}} \sim \sqrt{\frac{K(\text{O-H}) - \langle \delta K(M-O) \rangle}{\mu}}$, resulting in different Raman/IR peaks for different $M1M2M2$ chemical configurations (paper on Raman; e.g. Lacalamita et al., 2020, paper on IR; Redhammer et al., 2000). It should be emphasized that according to group theory two H⁺ in the primitive

unit cell participate into the OH-stretching A_g mode. At the same time, two $X(OH)^-$ in the chemical formula correspond to three octahedrally coordinated M-cations ($M1M2M2$). Hence, $\langle \delta K(M - O) \rangle$ is related precisely to those three octahedra and consequently the intensities of the OH stretching peaks arising from different $M1M2M2$ triplets can be used for the correct quantification of the chemical composition of the octahedral sheets in biotite.

Table 3 presents the assignment of the multi-component Raman scattering in the OH-stretching region of the analysed biotites to specific M -site local arrangements, following the categorization by Vedder (1964) based on the valence state of the $M1M2M2$ triplet surrounding the OH groups and the possibility of a vacancy at the M -site: (i) the N-type bands (normal; $M^{2+}M^{2+}M^{2+}$) where the hydroxyl groups are surrounded by three divalent cations, (ii) the I-type bands (impurity; $M^{2+}M^{2+}M^{3+}$), where the stretching modes are caused by hydroxyl groups surrounded by one trivalent and two divalent M -site cations, and (iii) the V-type bands (vacancy; $M^{2+}M^{2+\square} / M^{2+}M^{3+\square} / M^{3+}M^{3+\square}$), where the local atomic arrangement of the OH bonding includes a vacancy and two occupied octahedral sites.

In accordance with the two-mode behavior approach, the strongest OH-stretching peak corresponds to the most abundant $M1M2M2$ chemical configuration. Since biotite represents a solid-solution between phlogopite and annite, where Mg and Fe^{2+} are the dominant octahedrally coordinated cations, for each biotite sample the most intense OH-stretching peak should correspond to the most probable $M^{2+}M^{2+}M^{2+}$ chemical species. Hence, weaker OH-stretching peaks will correspond to less probable $M1M2M2$ local configurations. Consequently, peaks related to MgMgMg-OH $^-$ -K-X local configurations are observed for all of the studied phlogopite samples (B1, B2, B3, B5, B6, B7, B8, B10, B17, and B20) with the exception of sample B12, which shows an intermediate composition in the octahedral layer (see Table 1). However, the peak position slightly varies depending on the X-site anion adjacent to AK . Furthermore, the majority of the phlogopite samples exhibits OH-stretching modes in the range 3660-3670 cm^{-1} corresponding to MgMgFe $^{3+}$ and MgMgAl, whose OH groups are involved in a OH $^-$ -K-OH $^-$ local environment (Tlili et al., 1989; Scordari et al., 2006; Lacalmita et al., 2011; Scordari et al., 2012; Schingaro et al., 2013). It is worth noting that the gradual substitution of Mg by Al at the M -site, emerging from the Al-Tschermak substitution mechanism, will downshift the peak position of the initial MgMgMg-OH $^-$ -K-OH $^-$ local configuration by ~ 30 -35 cm^{-1} , i.e. from ~ 3705 -3715 to 3670-3675 cm^{-1} . This assumption corroborates the conclusions by Hawthorne et al. (2000), Scordari et al. (2012) and Watenphul et al. (2016a), who showed that a similar Raman peak shift towards lower frequencies has been monitored for the OH-stretching peaks in tremolites and phlogopite as well as for the W -site OH stretching in tourmalines.

At the same time, most of the examined annite samples (B4, B13, B14, B16, B18, B19, and B21) display the strongest OH-stretching N-type Raman peak between 3650 and 3660 cm^{-1} (Figs. S2 and S3, Table 3), corresponding to $Fe^{2+}Fe^{2+}Fe^{2+}$ -OH $^-$ -K-X (Redhammer et al., 2000). For sample B16, an aluminian F-rich annite, the Raman peak at ~ 3596 cm^{-1} is assigned to a $Fe^{2+}Al^{\square}$ -OH $^-$ local configuration (Redhammer et al., 2000) rather than to MgMg $^{\square}$ -OH $^-$, by taking into account the following aspects; (i) the peak centered at ~ 3596 cm^{-1} is the strongest feature of the $\bar{z}(yy)z$ Raman spectrum of sample B16 (Fig. S2) indicating that it should be assigned to the most abundant cations at the M -site and (ii) the cationic distribution of the M -site with $^MFe^{2+} = 1.54$ apfu, $^MAl = 0.88$ apfu and $^MMg = 0.10$ apfu.

4 Discussion

4.1 Major elements in the octahedral sheets

Quantification of ${}^M\text{Mg}$ content in apfu can be achieved by the Raman signals of two different vibrational groups (Fig. 5). The best candidate from the framework vibrational modes are the MO_6 vibrations at $\sim 190 \text{ cm}^{-1}$, whose peak position and FWHM are plotted against M -site Mg concentration (Fig. 5a). Data points of both plots were fitted with the exponential functions $\omega_{190} = (197.1 \pm 0.3) - 40.57e^{-1.213}{}^M\text{Mg}$ and $\text{FWHM}_{190} = (6.8 \pm 2.6) + (77.1 \pm 16.8)e^{(-1.2 \pm 0.3)M\text{Mg}}$, respectively. Then, using the inverse functions ${}^M\text{Mg}(\omega_{190}) = \frac{\ln 40.57}{1.213} - \frac{\ln[197.1 - \omega_{190}]}{1.213}$ and ${}^M\text{Mg}(\text{FWHM}_{190}) = \frac{\ln 77.1}{1.2} + \frac{\ln[\text{FWHM}_{190} - 6.8]}{1.2}$, one can calculate the content of ${}^M\text{Mg}$ from the Raman data (${}^M\text{Mg}_{\text{Raman}}$). It is worth noting that sample B16, an aluminian F-rich annite, strongly deviates from both exponential trends in Fig. 5a; which we attribute to the high amount of octahedrally coordinated Al > 0.8 apfu and highest among the studied biotites; consequently an alternative should be found to quantify ${}^M\text{Mg}$ in such ${}^M\text{Al}$ -rich biotites. Moreover, ${}^M\text{Mg}_{\text{Raman}}$ plotted against ${}^M\text{Mg}_{\text{EMP}}$ (Fig. 5b) reveals relatively large deviation from the one-to-one correlation line for phlogopite (${}^M\text{Mg} > 1.5$ apfu). Hence, the introduction of a second vibrational group sensitive to M -site occupancy by Mg is mandatory to solve this issue.

As pointed out above, the M -site chemistry has a strong effect on the OH bond-stretching modes, in a way very similar to that for amphiboles (Leissner et al, 2015; paper on IR; e.g. Hawthorne, 2016). The correct assignment of the OH-stretching peaks to different chemical $M1M2M2$ species is however, a key factor for the proper utilization of the two-mode-behavior approach, since the peak position of the strongest OH Raman peak will reveal the dominant cations occupying the octahedral layer. We have attributed the observed OH-stretching peaks based on multiple studies by others (see Table 3, Fig. 5c). Then the content of ${}^M\text{Mg}$ was calculated by averaging the sum of the integrated I of each parallel-polarized orientation [$\bar{z}(yy)z$ and $\bar{y}(zz)y$] generated by Mg-containing $M1M2M2$ configurations, multiplied by the number of Mg cations in the corresponding

$$\text{triplet: } {}^M\text{Mg}_{\text{Raman (horizontal), (vertical)}} = \frac{3I_{\text{MgMgMg-OH-K-OH}} + 3I_{\text{MgMgMg-OH-K-F}} + 2I_{\text{MgMgFe}^{2+}} + 3I_{\text{MgMgMg-OH-K-O}^{2-}} + I_{\text{MgFe}^{2+}\text{Fe}^{2+}} + 2I_{\text{MgMgFe}^{3+}} + 2I_{\text{MgMgAl}} + 2I_{\text{MgMg}\square}}{I_{\text{OH (total)}}}, \text{ where } I_{\text{OH (total)}} \text{ the}$$

sum of the integrated intensities of all OH-stretching modes in both $\bar{z}(yy)z$ and $\bar{y}(zz)y$ Raman spectra; in the case of a single-crystal grain with unknown orientation or polycrystalline sample, $I_{\text{OH (total)}}$ can be simply the intensity summed up over all OH-stretching Raman peaks. The ${}^M\text{Mg}_{\text{Raman (aver.)}}$ values plotted against those calculated from the EMP analysis (${}^M\text{Mg}_{\text{EMP}}$) exhibit an excellent one-to-one correlation (Fig. 5d).

It is worth commenting more in detail the OH-stretching peak assignment of B18 (magnesian ${}^A\text{K}$ -deficient annite). The Raman peak at 3570 cm^{-1} observed in the spectrum of B18 was assigned to $\text{Fe}^{2+}\text{Fe}^{2+}\text{Fe}^{3+}\text{-OH}^- \text{-}{}^A\square\text{-OH}^-$ rather than to $\text{Fe}^{3+}\text{Al}\square\text{-OH}^- \text{-K-OH}^-$, which generates an infrared absorption peak in close proximity in energy (Redhammer et al., 2000), based on the following decisive criteria: (i) this is the strongest Raman signal in the OH-stretching range and therefore it can be hardly attributed to defects in the octahedral layer. (ii) B18 is the only interlayer-deficient biotite among all the samples studied here, with a considerable amount of A -site vacancies ${}^A(\text{K}_{0.63}\square_{0.37})$; (iii) B18 is ${}^M\text{Al}$ -poor annite, i.e. Fe^{2+} and Fe^{3+} are the most abundant octahedrally coordinated cations; (iv) previous Raman and infrared studies on amphiboles (Leissner et al., 2015; Hawthorne, 2016) indicated that an OH-stretching peak generated by a given triplet of MO_6 octahedra next to A -site vacancy is downshifted in wavenumber by approximately $50\text{-}60 \text{ cm}^{-1}$ with respect to the OH-stretching peak generated by the same MO_6 -triplet but next to a filled A -site, which favors $\text{Fe}^{2+}\text{Fe}^{2+}\text{Fe}^{3+}$ over $\text{Fe}^{2+}\text{Fe}^{2+}\text{Fe}^{2+}$ configuration (compare the corresponding

peak positions related to ${}^A\text{K}$ in Table 3). It should be mentioned that a perfect match of sample B18 with the one-to-one line of figure 5d can be achieved by taking into consideration the influence of ${}^T\text{Al}$ on the ω of the $M1M2M2$ triplets in the $\bar{z}(yy)z$ scattering geometry, since B18 has the highest content of tetrahedrally coordinated Al in the sample suite studied here (${}^T\text{Al} = 1.51$ apfu). Previous research on the ${}^T\text{Al}$ effect in synthetic amphiboles with vacant A-sites (Hawthorne et al., 2000) and along the annite - siderophyllite ($\text{K}(\text{Fe}^{2+}, \text{Al})(\text{Si}_2\text{Al}_2)\text{O}_{10}(\text{OH})_2$) join with fully occupied A-sites (Redhammer et al., 2000) indicated that progressive substitution of ${}^T\text{Si}$ by ${}^T\text{Al}$ resulted in a downshift of the OH-stretching bands by 15-20 cm^{-1} . This accounts principally for the N- and I-type OH Raman peaks in the case of ${}^T\text{Al}$ -rich annite. Thus, the peaks at 3677 and 3655 cm^{-1} of the horizontal parallel-polarized spectrum of B18 should rather be assigned to $\text{MgMgFe}^{2+}\text{-OH}^-$ and $\text{MgFe}^{2+}\text{Fe}^{2+}\text{-OH}^-$ local arrangements, respectively. Therefore, an ${}^M\text{Mg}_{\text{Raman (aver.)}}$ value of 0.73 apfu can be obtained, which is almost identical to 0.70 apfu of the EMP analysis. Nevertheless, the crosschecking of the calculations gained from Figs. 5b and 5d, will reduce the uncertainties and give an unequivocal determination of ${}^M\text{Mg}$ content of sample B18.

Nominally biotite is an ${}^M(\text{Mg}, \text{Fe}^{2+})$ solid solutions and therefore ω_{190} as a function of the ${}^M\text{Fe}^{2+}$ content shows a reverse trend (see Fig. 6a) compared to that against ${}^M\text{Mg}$ content (Fig. 5a). Consequently, ${}^M\text{Fe}^{2+}$ content can be estimated using the equation $\omega_{190} = (196.6 \pm 0.3) - 0.891e^{(1.71 \pm 0.20)M\text{Fe}^{2+}}$. However, similarly to the case of ${}^M\text{Mg}$ (Fig. 5b), there is an unsatisfactory deviation of the phlogopite data set from the one-to-one-correlation (see Fig. S4). Since the ${}^M\text{Mg}$ content could be quantified more precisely by the integrated I of OH-bond stretching, the same strategy was followed to quantify ${}^M\text{Fe}^{2+}$, using

the equation ${}^M\text{Fe}^{2+}_{\text{Raman (horizontal), (vertical)}} = \frac{I_{\text{MgMgFe}^{2+}} + 2I_{\text{MgFe}^{2+}\text{Fe}^{2+}} + 3I_{\text{Fe}^{2+}\text{Fe}^{2+}\text{Fe}^{2+}} + 2I_{\text{Fe}^{2+}\text{Fe}^{2+}\text{Fe}^{3+}} + I_{\text{Fe}^{2+}\text{Al}\square}}{I_{\text{OH (total)}}$, where $I_{\text{OH (total)}}$ the

sum of the integrated intensities of all OH-stretching modes of the horizontal and vertical parallel-polarized spectra, respectively. Figure 6b shows the correlation of ${}^M\text{Fe}^{2+}_{\text{Raman (aver.)}}$ with ${}^M\text{Fe}^{2+}$ concentration determined by EMPA, where the data points for Mg-rich biotites with ${}^M\text{Fe}^{2+} < 0.8$ apfu follow an one-to-one correlation line and for Fe-rich biotites (with ${}^M\text{Fe}^{2+} > 0.8$ apfu) a linear trend that can be expressed by the relation ${}^M\text{Fe}^{2+}_{\text{Raman (aver.)}} = (0.32 \pm 0.11) + (1.21 \pm 0.07) * {}^M\text{Fe}^{2+}_{\text{EMPA}}$.

It should be underlined that the presence of ${}^M\text{Fe}^{3+}$ also affects the peak position of the MO_6 vibrations at ~ 190 cm^{-1} , which increases exponentially with increasing ${}^M(\text{Fe}^{2+} + \text{Fe}^{3+})$ content and can be calculated by $\omega_{190} = 197.5 - (0.67 \pm 0.27)e^{(1.76 \pm 0.25)M(\text{Fe}^{2+} + \text{Fe}^{3+})}$ (Fig. 6a). Besides that, the integrated intensities of the OH vibrational modes, where Fe^{3+} is involved in the assigned local environment and are mainly emerging from the MgMgFe^{3+} and $\text{Fe}^{2+}\text{Fe}^{2+}\text{Fe}^{3+}$ triplets for phlogopite and annite, respectively, can be used to quantify the total amount of octahedrally coordinated Fe and then plotted against ${}^M(\text{Fe}^{2+} + \text{Fe}^{3+})_{\text{EMPA}}$ (Fig. 6c). Similarly to the trends in Fig. 6b, good one-to-one correlation can be achieved for phlogopite with ${}^M(\text{Fe}^{2+} + \text{Fe}^{3+}) < 0.8$ apfu, whilst for samples exceeding this value, ${}^M(\text{Fe}^{2+} + \text{Fe}^{3+})$ content can be obtained from ${}^M(\text{Fe}^{2+} + \text{Fe}^{3+})_{\text{Raman (aver.)}} = (-0.38 \pm 0.17) + (1.47 \pm 0.08) * {}^M(\text{Fe}^{2+} + \text{Fe}^{3+})_{\text{EMPA}}$.

The fact that ${}^M\text{Fe}^{2+}$ and ${}^M(\text{Fe}^{2+} + \text{Fe}^{3+})$ are overestimated by Raman spectroscopy, while ${}^M\text{Mg}$ is not, suggests that additional non-magnesium, non-iron elements contribute to the spectral range dominated by OH-stretching modes related to ferrous/ferric $M1M2M2$ configurations. This is also evident by the overall broad bands (FWHM $\sim 27\text{-}40$ cm^{-1}) in the range 3650-3660 cm^{-1} in the $\bar{z}(yy)z$ Raman spectra of annite samples (B13, B14, B16, B18, and B19), indicating a superposition of multiple different octahedrally-coordinated cationic combinations such as $\text{Fe}^{2+}\text{Fe}^{2+}\text{Fe}^{3+}$, $\text{Fe}^{2+}\text{Fe}^{2+}\text{Al}$, and $\text{AlAl}\square$ - (e.g. Redhammer et al., 2000; Libowitzky and Beran, 2004; Scordari et al., 2008; Schingaro et al., 2013). Hence, subtle amounts of minor elements such as

Al, Ti, and Mn, entering the *M*-site, whose vibrational modes cannot be separated from the ascribed ones, lead to the deviation of the annite dataset from the one-to-one correlation lines of Figs. 6b and 6c. This can be seen by plotting the contents of the non-(Mg,Fe) octahedrally coordinated cations calculated from the Raman and EMP analyses (Fig. 6d), where an one-to-one match with discrepancies within the relative errors is observed for all samples. The only exception is sample B16, characterized by an unusual high content of non-(Mg, Fe) cations of almost 47% of the *M*-site occupancy. By subtracting the excess of ${}^M\text{Fe}^{2+}$ [$y_2(x)$ in Fig. 6b] from the total amount of octahedrally coordinated [$y_2(x)$ in Fig. 6c], one can estimate ${}^M\text{Fe}_{\text{Raman (aver.)}}^{3+} = (-0.70 \pm 0.20) + (0.26 \pm 0.11) * {}^M\text{Fe}_{\text{EMP}}^{3+}$, which is significant in Earth sciences, as it is indicative of oxidation processes. We could not find a satisfactory trend to directly quantify ${}^M\text{Fe}^{3+}$, e.g. via ω and integrated *I* of the Raman scattering in the range 500-550 cm^{-1} , which is noticeable spectral indicators for the presence of octahedrally coordinated Fe^{3+} in Na amphiboles (Waesermann et al. 2020).

4.2. Major elements in the tetrahedral sheets

Among the framework phonon modes the TO_4 -ring modes near 650 cm^{-1} and 680 cm^{-1} (i.e. T- O_b -T bending) appear to be most sensitive to the *T*-site occupancy (see Fig. 7a). However, the position of the Raman peak near 680 cm^{-1} (Si- O_b -Si) turned to be also sensitive to the content of ${}^M\text{Ti}$ (see the discussion below), whereas the position of the peak near 650 cm^{-1} (Si- O_b -Al) is indifferent to the *M*-site occupancy. Therefore, we propose to use the wavenumber of the TO_4 -ring mode near 650 cm^{-1} to estimate the amount of ${}^T\text{Si}$. The evolution of ω_{650} with respect to ${}^T\text{Si}$ can be fitted with a Boltzmann-type function $\omega_{650} = 673.5 + (638.5 - 673.5) / (1 + e^{\frac{{}^T\text{Si}-2.92}{0.078}})$, and then the ${}^T\text{Si}$ amount can be quantified by the inverse function ${}^T\text{Si} = 0.078 * [\ln(\omega_{650} - 638.5) - \ln(673.5 - \omega_{650})] + 2.92$ (see Fig. 7a). Only sample B3 slightly deviates from fitting trend, an effect that can be connected to the incorporation of Fe^{3+} at the *T*-site. Despite that, the plot of ${}^T\text{Si}$ amount derived from the Raman data against ${}^T\text{Si}_{\text{EMP}}$ provides an excellent one-to-one correlation for all values between 2.6 and 3.2 apfu with a relative uncertainty of $\sim 3\%$ (Fig. 7b). Due to the sigmoidal shape of the ${}^T\text{Si}(\omega_{650})$ -curve the uncertainty in determining ${}^T\text{Si}$ considerably increases for values below 2.6 apfu.

The common tetrahedrally coordinated elements in biotite are Si, Al and trivalent Fe, but ${}^T\text{Fe}^{3+}$ is usually found in annite rather than in phlogopite. Therefore, for phlogopite the amount of tetrahedrally coordinated Al cations can be also determined ω_{650} as ${}^T\text{Al} = 4 - {}^T\text{Si}(\omega_{650})$ apfu. This can help in general to cross-check the correctness of OH-stretching assignment, which is significant for the refinement of the *M*-site occupancy, because studies on the annite - siderophyllite ($\text{K}(\text{Fe}_2^{2+}, \text{Al})(\text{Si}_2\text{Al}_2)\text{O}_{10}(\text{OH})_2$) join (Redhammer et al., 2000) as well as on amphiboles with vacant A-sites (Hawthorne et al. 2000) revealed that the progressive substitution of ${}^T\text{Al}$ for ${}^T\text{Si}$ results in a downshift of the OH-stretching mode by 15-20 cm^{-1} .

4.3. Presence of *M*-site Ti

Interestingly, the position and FWHM of the TO_4 -ring mode at $\sim 680 \text{ cm}^{-1}$, involving Si- O_b -Si bond bending vibrations exhibit a linear correlation with the ${}^M\text{Ti}$ (Fig. 7c and 7e, respectively), without showing any dependence on the major *M*-site elements. This is probably related to the fact that tetravalent Ti interacts stronger with the TO_4 apical oxygen atoms, resulting

in subtle change of the TO_4 ring tilt geometry and thus influencing the T-O-T bending vibrations. The linear fits to the corresponding data points yielded $\omega_{680} = (684.7 \pm 0.4) - 43.5^{\text{M}Ti}$ and $\text{FWHM}_{680} = (18.7 \pm 1.3) + 150.5^{\text{M}Ti}$. As can be seen in Figs. 7d and 7f several data points for annite (samples B4, B12, B13, and B18) derived from $^{\text{M}Ti}(\omega_{680})$ deviate from the one-to-one trend, whereas the dispersion is considerably less for the data derived from $^{\text{M}Ti}(\text{FWHM}_{680})$. Thus, using the relation $^{\text{M}Ti} = [\text{FWHM}_{680} - (18.7 \pm 1.3)]/150.5$, one can determine $^{\text{M}Ti}$ with a relative uncertainty of $\sim 20\%$. The only deviating point in the trend showed in Fig. 7f is sample B4, in whose spectrum the two peaks near 650 and 680 cm^{-1} could not be resolved and appeared as a single very broad Raman peak centered at $\sim 670 \text{ cm}^{-1}$ with $\text{FWHM}_{680} = 105.3 \text{ cm}^{-1}$ (Fig. 7e). It should be mentioned that in Ti-rich biotites ($^{\text{M}Ti} > 0.2$ apfu) contributions from OH-stretching of X-site hydroxyl groups shared between Ti-containing $M1M2M2$ triplets can be expected (e.g. Scordari et al., 2006). However, to keep local charge balance, commonly the anionic X sites next to $^{\text{M}Ti}$ is occupied by O^{2-} forming local chemical arrangement of type $\text{K-O}^{2-}\text{-M}^{2+}\text{M}^{2+}\text{Ti}^{4+}\text{-O}^{2-}\text{-K}$, that is no OH peaks should be observed. Possible Raman active modes of the OH-stretching vibrations, including Ti in the assigned triplets to comply with the requirements for local charge balance can be: $\text{K-OH-M}^{2+}\text{Ti}^{4+}\text{-OH-K}$, $\text{K-O}^{2-}\text{-M}^{2+}\text{M}^{2+}\text{Ti}^{4+}\text{-OH-}^{\Delta}\square$ or less probably $^{\Delta}\square\text{-O}^{2-}\text{-M}^{2+}\text{M}^{2+}\text{Ti}^{4+}\text{-OH-K}$. Such considerations are supported by the main substitution mechanisms involving Ti after Li et al. (2020). However, we could not resolve such additional OH-stretching peaks in our Ti-rich samples, namely phlogopite B6, B8, and B20 and annite B4, B14, and B21.

4.4. Interlayer cations

In contrast to earlier findings by Wang et al. (2015), a direct connection of linearly increasing $\text{Fe}^{2+}/(\text{Mg}+\text{Fe}^{2+})$ ratio with decreasing ω of the Raman peaks at $715\text{-}755$ (ω_{730}) and $760\text{-}780 \text{ cm}^{-1}$ (ω_{780}) could not be observed. Though, the peak position of the ring mode vibrations at $\sim 730 \text{ cm}^{-1}$ in the $\bar{y}(zz)y$ Raman spectra tends to be sensitive to the occupancy of the interlayer space and shifts linearly to higher wavenumbers in the presence of A-site vacancies with a gradient change at $^{\text{M}Mg}$ contents of 1.5 apfu. This tendency reflects to some extent the evolution of $^{\text{A}K}$ content with increasing ω_{730} values. Accordingly, $^{\text{A}K}$ content was only plotted against ω_{730} (Fig. 8a), as ω_{780} could not mirror the amount of A-site cations, in particular of K. For biotites belonging to the phlogopite series $^{\text{A}K}$ content can be determined by using the equation $\omega_1 = (1529 \pm 37) - (918 \pm 45)^{\text{A}K}$, while that of annite can be expressed by the relation $\omega_2 = 862 - 157^{\text{A}K}$. The Raman scattering analysis provides precise calculation of the amount of $^{\text{A}K}$ for the phlogopite dataset with a relative error of $\sim 3\%$, but the uncertainty obtained from the inverse trend of ω_1 is too large to quantify $^{\text{A}K}$ content of annite (Fig. 8b). Sample B6 deviates from the ω_2 linear trend and is characterized by $^{\text{M}Fe^{3+}}$ contents of ~ 0.30 apfu. Though, it cannot be stated whether the elevated $^{\text{M}Fe^{3+}}$ contents in the crystal structure of phlogopite shift the corresponding peak towards higher wavenumbers, since in the sample B5, an octaferrian phlogopite with similar amount of $^{\text{M}Fe^{3+}}$, we could not identify a peak between 715 and 755 cm^{-1} .

4.5. Limitations of the method

Raman spectroscopy as any other analytical technique has its limitations and undoubtedly, it cannot achieve the detection limit of EMPA ($\sim 100\text{-}200$ ppm) and trace elements cannot be detected by Raman spectroscopy. Besides, the uncertainties in the quantification of major and minor elements by Raman spectroscopy are affected by the quality of the measured spectra, i.e.

by the signal-to-noise ratio and spectral resolution. Nevertheless, here we demonstrate that the relative uncertainties of ${}^T\text{Si}$, ${}^A\text{K}$, ${}^M\text{Mg}$, ${}^M\text{Fe}^{2+}$, and ${}^M\text{Fe}^{3+}$ amounts in apfu, as derived from Raman scattering data, are 3, 3, 6, 6, and 8%, respectively, whereas the uncertainties in the chemical formulae calculated from EMP data are ~1-2%. Moreover, the determination of Fe^{3+} only on the basis of EMPA is not straightforward. Minor elements such as ${}^M\text{Ti}$ can be estimated by Raman spectroscopy with a relatively large uncertainty of 20% against 6% by EMPA.

5 Conclusions

The results of our combined Raman spectroscopic and WD-EMP as well as Mössbauer analyses clearly reveal that the major cations occupying the octahedral, tetrahedral and interlayer sites of biotites can be determined with acceptable relative errors. Minor elements at the *M*-site such as Ti, which are critical crystallochemical markers indicative of specimen locality, can be quantified as well. According to the overall spectral profile, one can easily distinguish between phlogopite and annite, as the strongest MO_6 -peak (region I; Fig. 4) appears at ~ 195 and 165 cm^{-1} , respectively, while the strongest OH-stretching peak (region IV; Fig. 4) at 3710 cm^{-1} and 3650 cm^{-1} , respectively. Furthermore, the established calibration curves between the Raman signals and the chemical composition of the analysed biotites provide a preparation-free, fast, and easy-to-handle tool for the crystallochemical characterization of those phyllosilicates. Guidelines for non-specialists to non-destructively determine the crystallochemical composition of biotites are listed as follows:

- 1) By following the recommended OH-stretching peak assignment to different local cationic arrangements (Table 3), ${}^M\text{Mg}_{\text{Raman (aver.)}}$, ${}^M\text{Fe}^{2+}_{\text{Raman (aver.)}}$, and ${}^M(\text{Fe}^{2+}+\text{Fe}^{3+})_{\text{Raman (aver.)}}$ can be calculated.
- 2) Deviations from the one-to-one correlation lines, in the case of estimating the ${}^M\text{Fe}^{2+}$ and ${}^M\text{Fe}^{3+}$ amounts, demonstrate incorporation of non-(Mg, Fe) cations in the octahedral layer (Fig. 6d).
- 3) The amount of *M*-site Mg, Fe^{2+} , and Fe^{3+} can be cross-checked by the position of the strong Raman peak near 190 cm^{-1} , arising from the MO_6 vibrations; in the case of ${}^M\text{Mg}$, FWHM_{190} can be used as well.
- 4) ${}^M\text{Ti}$ content can be quantified by the peak position and FWHM of the TO_4 -ring mode at ~680 cm^{-1} . Due to smaller relative errors, it is recommended to use the ${}^M\text{Ti}(\text{FWHM}_{680})$ trend, if two peaks near 650 and 680 cm^{-1} can be resolved.
- 5) The presence of ${}^M\text{Al} > 0.8$ apfu in annite can be detected by cross-checking the ${}^M\text{Mg}$ contents derived from ω_{190} and of the integrated intensities of the OH-stretching peaks.
- 6) The amount of ${}^T\text{Si}$ can be monitored using the peak position of the TO_4 -ring modes at ~650 cm^{-1} . ${}^T\text{Al}$ content of phlogopite can indirectly be extracted by ${}^T\text{Al} = 4 - {}^T\text{Si}$.
- 7) Potassium deficiency in phlogopite larger than 0.12 apfu can be quantified from the position of the peak at ~730 cm^{-1} . Interlayer-deficient annite can be recognized by the position of the strongest OH-stretching mode, appearing at 3570 instead of ~3650 cm^{-1} .

Overall, our study shows that Raman spectroscopy is a reliable experimental method for the crystallochemical characterization also for biotites along with other complex hydrous silicates, though still not so precise as EMPA. However, the truly non-destructive nature of Raman spectroscopy makes it an extremely useful tool for characterizing cultural-heritage objects and the trends provided here demonstrate that it can be used even for quantitative analyses. Moreover, one can directly analyze mineral grains in thin sections as prepared for polarization microscopy. It is highly anticipated that a similar analytical

approach to other groups of phyllosilicates, including those that can be found in cultural-heritage artefacts, could facilitate the non-invasive determination of their crystallochemical composition.

Data availability

Data derived from this research are presented in the manuscript supplementary material. Additional data are available upon request from the corresponding author.

Author contributions

BM and JS initiated the project. SA carried out the Raman experiments as well as the Raman and EMP data evaluation and analyses. GR performed the Mössbauer spectroscopic analysis. SA prepared the manuscript with contributions from BM and JS. All authors discussed and interpreted the results.

Competing interests

The authors declare that they have no conflict of interest.

Acknowledgements

The research for this study was funded by the Deutsche Forschungsgemeinschaft (DFG, German Research Foundation) under Germany's Excellence Strategy – EXC 2176 'Understanding Written Artefacts: Material, Interaction and Transmission in Manuscript Cultures', project no. 390893796. The research was conducted within the scope of the Centre for the Study of Manuscript Cultures (CSMC) at Universität Hamburg. We thank Stefanie Heidrich and Peter Stutz, Universität Hamburg, to help with WD-EMPA measurements and sample preparation. We are very grateful to the Mineralogical Museum, at Universität Hamburg for kindly providing the whole of the biotite crystals.

References

- Bendel, V. and Schmidt, B.C.: Raman spectroscopic characterisation of disordered alkali feldspars along the join KAlSi_3O_8 - $\text{NaAlSi}_3\text{O}_8$: application to natural sanidine and anorthoclase. *Eur. J. Mineral.*, 20, 1055-1065, 2008.
- Bersani, D. and Lottici, P.P.: Raman spectroscopy of minerals and mineral pigments in archaeometry. *J. Raman Spectrosc.*, 47, 499-530, 2016.
- Brigatti, M.F., Frigieri, P., Ghezzi, C., and Poppi L.: Crystal chemistry of Al-rich biotites coexisting with muscovites in peraluminous granites. *Am. Mineral.*, 85, 436-448, 2000.
- Brigatti, M.F., Kile, D.E., and Poppi, M.: Crystal structure and crystal chemistry of Lithium-bearing muscovite-2M₁. *Canad. Mineral.*, 39, 1171-1180, 2001.
- Brigatti, M.F., Affronte, M., Elmi, C., Malferrari, D., and Laurora, A.: Trioctahedral Fe-rich micas: Relationships between magnetic behavior and crystal chemistry. *Am. Mineral.*, 100, 2231-2241, 2015.
- Chang, I.F. and Mitra, S.S.: Long wavelength optical phonons in mixed crystals. *Adv. Phys.*, 20, 359-404, 1971.

- Corradini, M., de Ferri, L., and Pojana, G.: Spectroscopic characterization of commercial pigments for pictorial retouching. *J. Raman Spectrosc.*, 52, 35-58, 2021.
- El Halim, M., Daoudi, L., El Ouahabi, M., Rousseau, V., Cools, C., and Fagel, N.: Mineralogical and geochemical characterization of archaeological ceramics from the 16th century El Badi Palace, Morocco. *Clay Miner.*, 53, 459-470, 2018.
- Gianfagna, A., Scordari, F., Mazziotti-Tagliani, S., Ventruti, G., and Ottolini, L.: Fluorophlogopite from Biancavilla (Mt. Etna, Sicily, Italy): Crystal structure and crystal chemistry of a new F-dominant analog of phlogopite. *Am. Mineral.*, 92, 1601-1609, 2007.
- Hawthorne, F.C., Welch, M.D., Della Ventura, G., Liu, S., Robert, J.-L., and Jenkins, D.M.: Short-range order in synthetic aluminous tremolites. An infrared and triple-quantum MAS NMR study. *Am. Mineral.*, 85, 1716-1724, 2000.
- Hawthorne, F.C.: Short-range atomic arrangements in minerals. I: The minerals of the amphibole, tourmaline and pyroxene supergroups. *Eur. J. Mineral.*, 28, 513-536, 2016.
- Hradil, D., Píšková, A., Hradilová, J., Bezdička, P., Lehrberger, G., and Gerzer, S.: Mineralogy of Bohemian green earth pigment and its microanalytical evidence in historical paintings. *Archaeometry*, 53, 563-586, 2011.
- Kodama, H., Ross, G.J., Iiyama, J.T., and Robert, J.-L.: Effect of layer charge location on potassium exchange and hydration of micas. *Am. Mineral.*, 59, 491-495, 1974.
- Kroumova, E., Aroyo, M.I., Perez-Mato, J.M., Kirov, A., Capillas, C., Ivantchev, S., and Wondratschek, H.: Bilbao Crystallographic Server: useful databases and tools for phase-transition studies. *Ph. Transit.*, 76, 155-170, 2003.
- Lacalamita, M., Schingaro, E., Scordari, F., Ventruti, G., Fabbrizio, A., and Pedrazzi, G.: Substitution mechanisms and implications for the estimate of water fugacity for Ti-rich phlogopite from Mt. Vulture, Potenza, Italy. *Am. Mineral.*, 96, 1381-1391, 2011.
- Lacalamita, M., Schingaro, E., Mesto, E., Zaccarini, F., and Biagioni, C.: Crystal-chemistry of micas belonging to the yangzhumingite-fluorophlogopite and phlogopite-fluorophlogopite series from the Apuan Alps (northern Tuscany, Italy). *Phys. Chem. Miner.*, 47:54, 2020.
- Laurora, A., Brigatti, M.F., Mottana, A., Malferrari, D., and Caprilli, E.: Crystal chemistry of trioctahedral micas in alkaline and subalkaline rocks: A case study from Mt. Sassetto (Tolfa district, Latium, central Italy). *Am. Mineral.*, 92, 468-480, 2007.
- Leissner, L., Schlüter, J., Horn, I., and Mihailova, B.: Exploring the potential of Raman spectroscopy for crystallochemical analyses of complex hydrous silicates: I. Amphiboles. *Am. Mineral.*, 100, 2682-2694, 2015.
- Li, X., Zhang, C., Behrens, H., and Holtz, F.: Calculating amphibole formula from electron microprobe analysis data using a machine learning method based on principal components regression. *Lithos*, 362-363, 105469, 2020.
- Libowitzky, E. and Beran, A.: IR spectroscopic characterization of hydrous species in minerals, in: *Spectroscopic methods in mineralogy*, edited by Beran, A. and Libowitzky, E., EMU Notes in Mineralogy, Eötvös University Press, Budapest, 227-279, 2004.
- Loh, E.: Optical vibrations in sheet silicates. *J. Phys. C: Solid State Phys.*, 6, 1091-1104, 1973.
- McKeown, D.A., Bell, M.I., and Etz, E.S.: Raman spectra and vibrational analysis of the trioctahedral mica phlogopite. *Am. Mineral.*, 84, 970-976, 1999.

- Mihailova, B., Schlüter, J., and Harter-Uibopuu, K.: Inscribed gems: Material profiling beyond visible examination, in: Exploring written artefacts: Objects, methods and concepts, edited by Quenzer, J.B., De Gruyter, Berlin, Boston, 229-244, 2021.
- Milke, R.: Geomaterials in the manuscript archive: The composition of writing sands and the regional distribution of writing-sand types in SW-Germany and northern Switzerland, 14th to 19th century. *Eur. J. Mineral.*, 24, 759-770, 2012.
- Momma, K. and Izumi, F.: VESTA: a three-dimensional visualization system for electronic and structural analysis. *J. Appl. Crystallogr.*, 41, 653-658, 2008.
- Prencipe, M., Mantovani, L., Tribaudino, M., Bersani, D., and Lottici, P.P.: The Raman spectrum of diopside: a comparison between *ab initio* calculated and experimentally measured frequencies. *Eur. J. Mineral.*, 24, 457-464, 2012.
- Redhammer, G.J., Beran, A., Schneider, J., Amthauer, G., and Lottermoser, W.: Spectroscopic and structural properties of synthetic micas on the annite-siderophyllite binary: Synthesis, crystal structure refinement, Mössbauer, and infrared spectroscopy. *Am. Mineral.*, 85, 449-465, 2000.
- Redhammer, G.J., Amthauer, G., Lottermoser, W., and Roth, G.: Quadrupole splitting distribution of Fe²⁺ in synthetic trioctahedral micas. *Hyperfine Interact.*, 141/142, 345-349, 2002.
- Redhammer, G.J., Amthauer, G., Lottermoser, W., Bernroider, M., Tippelt, G., and Roth, G.: X-ray diffraction and ⁵⁷Fe – Mössbauer spectroscopy of synthetic trioctahedral micas {K}[Me₃<TSi₃>O₁₀(OH)₂, Me = Ni²⁺, Mg²⁺, Co²⁺, Fe²⁺; T = Al³⁺, Fe³⁺. *Mineral. Petrol.*, 85, 89-115, 2005.
- Rieder, M., Cavazzini, G., D'Yakonov, Y.S., Frank-Kamenetskii, V.A., Gottardi, G., Guggenheim, S., Koval, P.V., Müller, G., Neiva, A.M.R., Radoslovich, E.W., Robert, J.-L., Sassi, F.P., Takeda, H., Weiss, Z., and Wones, D.R.: Nomenclature of the micas. *Canad. Mineral.*, 36, 1-10, 1998.
- Righter, K., Dyar, M.D., Delaney, J.S., Vennemann, T.W., Hervig, R.L., and King, P.L.: Correlations of octahedral cations with OH⁻, O²⁻, Cl⁻, and F⁻ in biotite from volcanic rocks and xenoliths. *Am. Mineral.*, 87, 142-153, 2002.
- Schingaro, E., Lacalamita, M., Scordari, F., and Mesto, E.: 3T-phlogopite from Kasenyi kamafugite (SW Uganda): EPMA, XPS, FTIR, and SCXRD study. *Am. Mineral.*, 98, 709-717, 2013.
- Scordari, F., Ventruti, G., Sabato, A., Bellatreccia, F., Della Ventura, G., and Pedrazzi, G.: Ti-rich phlogopite from Mt. Vulture (Potenza, Italy) investigated by a multianalytical approach: Substitutional mechanisms and orientation of the OH dipoles. *Eur. J. Mineral.*, 18, 379-391, 2006.
- Scordari, F., Schingaro, E., Ventruti, G., Lacalamita, M., and Ottolini, L.: Red micas from basal ignimbrites of Mt. Vulture (Italy): Interlayer content appraisal by a multi-methodic approach. *Phys. Chem. Miner.*, 35, 163-174, 2008.
- Scordari, F., Schingaro, E., Lacalamita, M., and Mesto, E.: Crystal chemistry of trioctahedral micas-2M₁ from Bunyaruguru kamafugite (southwest Uganda). *Am. Mineral.*, 97, 430-439, 2012.
- Scordari, F., Schingaro, E., Ventruti, G., Nicotra, E., Viccaro, M., and Mazziotti Tagliani, S.: Fluorophlogopite from Piano delle Concazze (Mt. Etna, Italy): Crystal chemistry and implications for the crystallization conditions. *Am. Mineral.*, 98, 1017-1025, 2013.
- Singha, M. and Singh, L.: Vibrational spectroscopic study of muscovite and biotite layered phyllosilicates, *Indian J. Pure Appl. Phys.*, 54, 116-122, 2016.

- Tlili, A., Smith, D.C., Beny, J.-M., and Boyer, H.: A Raman microprobe study of natural micas. *Mineral. Mag.*, 53, 165-179, 1989.
- Tutti, F. and Lazor, P.: Temperature-induced phase transition in phlogopite revealed by Raman spectroscopy. *J. Phys. Chem. Solids*, 69, 2535-2539, 2008.
- Uchida, E., Niikuma, D., and Watanabe, R.: Regional differences in the chemical composition of cuneiform clay tablets. *Archaeological Discovery*, 3, 179-207, 2015.
- Vedder, W.: Correlations between infrared spectrum and chemical composition of mica. *Am. Mineral.*, 49, 736-768, 1964.
- Velbel, M.A.: Formation of protective surface layers during silicate-mineral weathering under well-leached, oxidizing conditions. *Am. Mineral.*, 78, 405-414, 1993.
- Waesermann, N., Schlüter, J., Malcherek, T., Della Ventura, G., Oberti, R., and Mihailova, B.: Nondestructive determination of the amphibole crystal-chemical formulae by Raman spectroscopy: One step closer. *J. Raman Spectrosc.*, 51, 1530-1548, 2020.
- Wang, A., Freeman, J.J., and Jolliff, B.L.: Understanding the Raman spectral features of phyllosilicates. *J. Raman Spectrosc.*, 46, 829-845, 2015.
- Wang, Y.Y., Gan, F.X., and Zhao, H.X.: Inclusions of black-green serpentine jade determined by Raman spectroscopy. *Vib. Spectrosc.*, 66, 19-23, 2013.
- Watenphul, A., Burgdorf, M., Schlüter, J., Horn, I., Malcherek, T., and Mihailova, B.: Exploring the potential of Raman spectroscopy for crystallochemical analyses of complex hydrous silicates: II. Tourmalines. *Am. Mineral.*, 101, 970-985, 2016a.
- Watenphul, A., Schlüter, J., Bosi, F., Skogby, H., Malcherek, T., and Mihailova, B.: Influence of the octahedral cationic-site occupancies on the framework vibrations of Li-free tourmalines, with implications for estimating temperature and oxygen fugacity in host rocks. *Am. Mineral.*, 101, 2554-2563, 2016b.
- Zazoff, P. (Eds.): *Die antiken Gemmen – Handbuch der Archäologie*, C.H. Beck'sche Verlagsbuchhandlung, Munich, Germany, 1983 (in German).

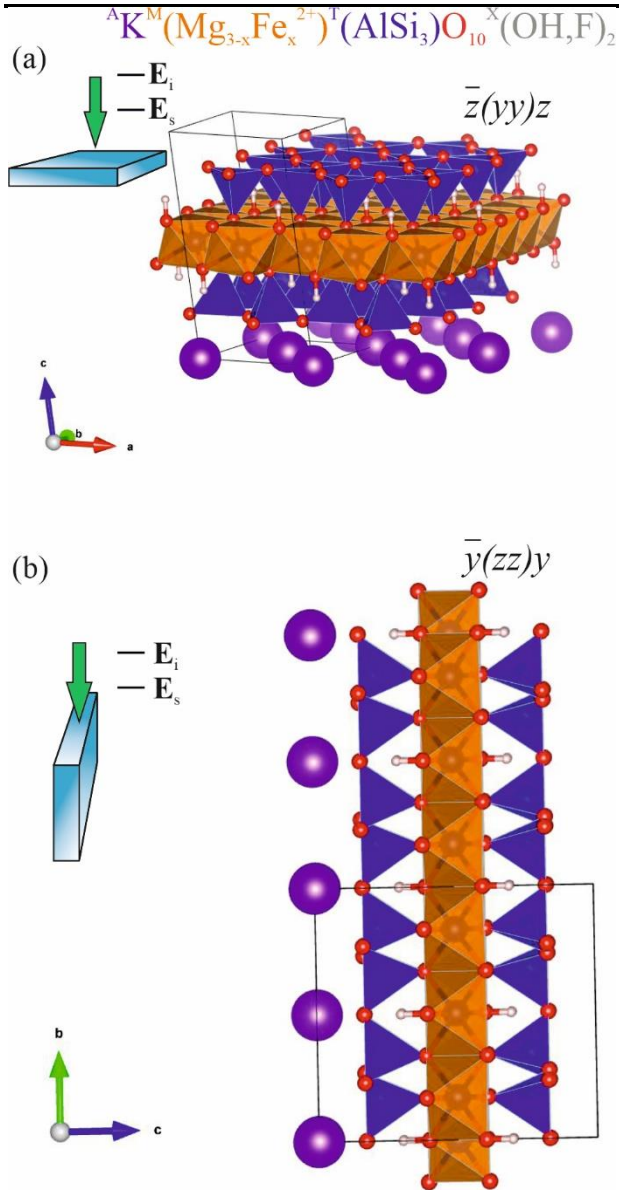


Figure 1: Sketch of the scattering geometries along with fragments of the atomic structure of biotite in the corresponding orientations: (a) horizontal orientation with the cleavage plane \perp to the laser beam direction and \parallel to E_i and (b) vertical orientation of the biotite crystal with the cleavage plane \parallel to laser beam direction and \perp to E_i . TO_4 tetrahedra are given in blue; MO_6 octahedra are given in orange; A-site cations in purple; O^{2-} anions in red and H^+ cations in pink-whitish. VESTA software package (Momma and Izumi, 2008) was used to plot the atomic structure.

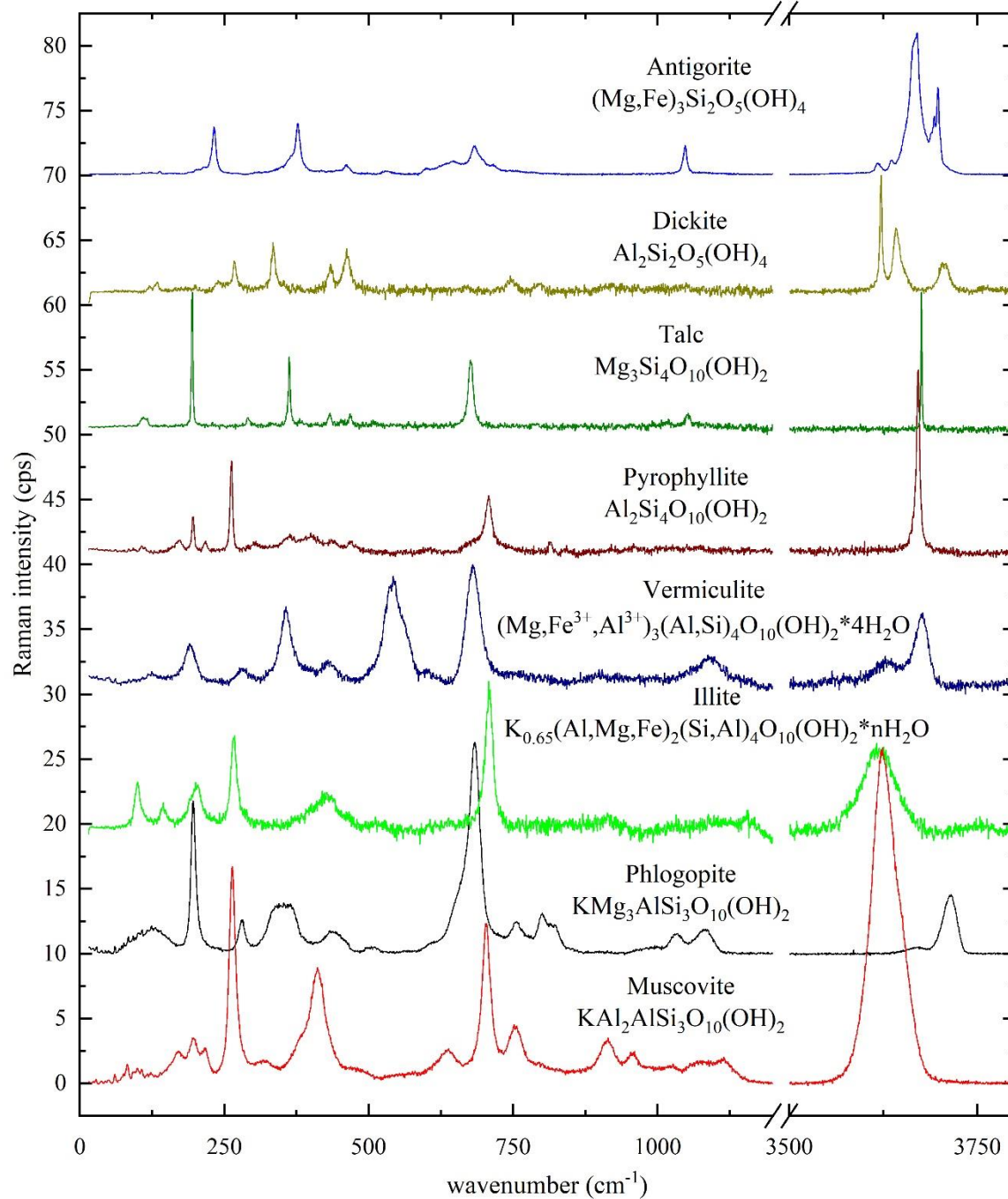


Figure 2: Raman spectra of various phyllosilicates. The spectra are vertically offset for clarity.

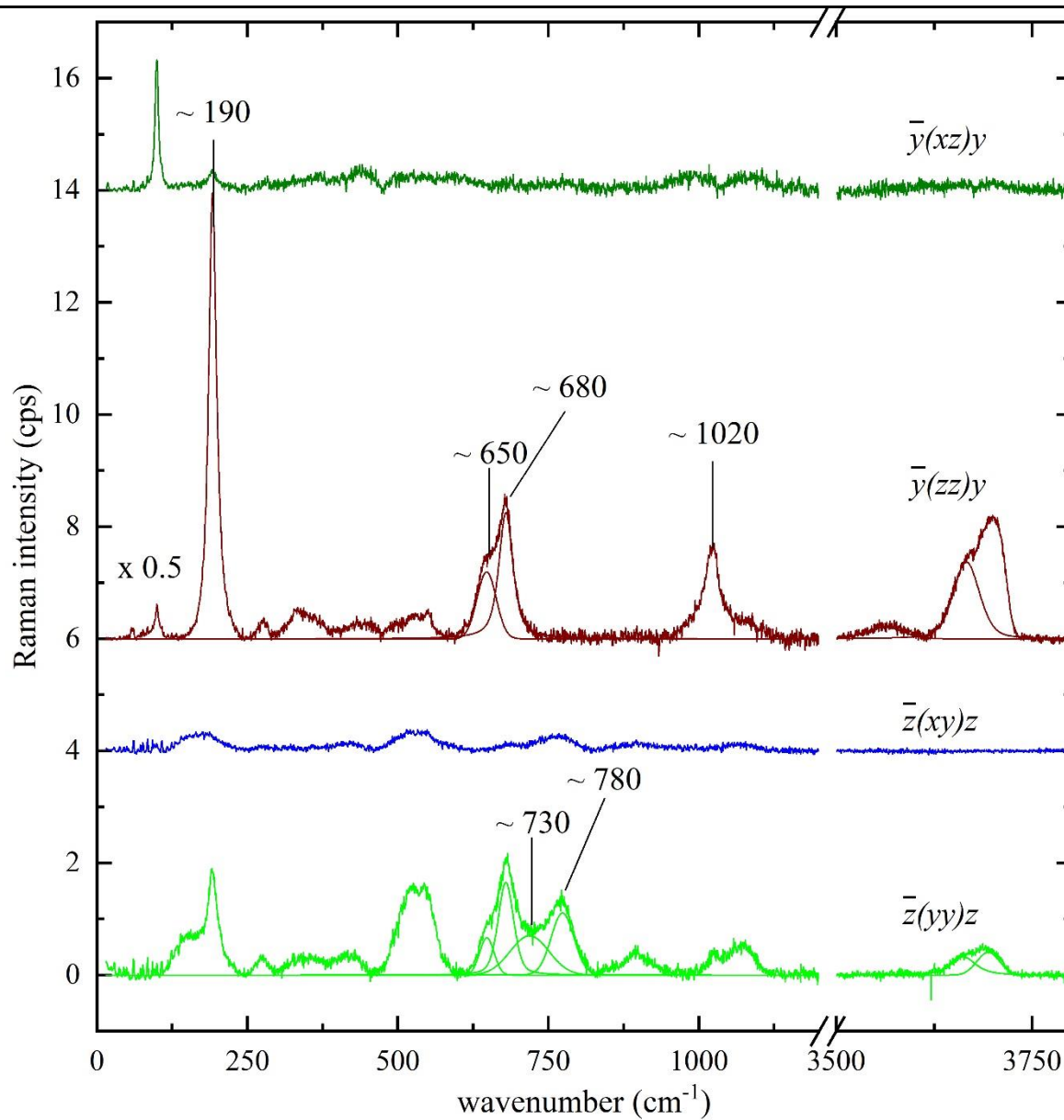


Figure 3: Raman spectra of phlogopite measured in four different scattering geometries, as described in the text. The spectra are vertically offset for clarity.

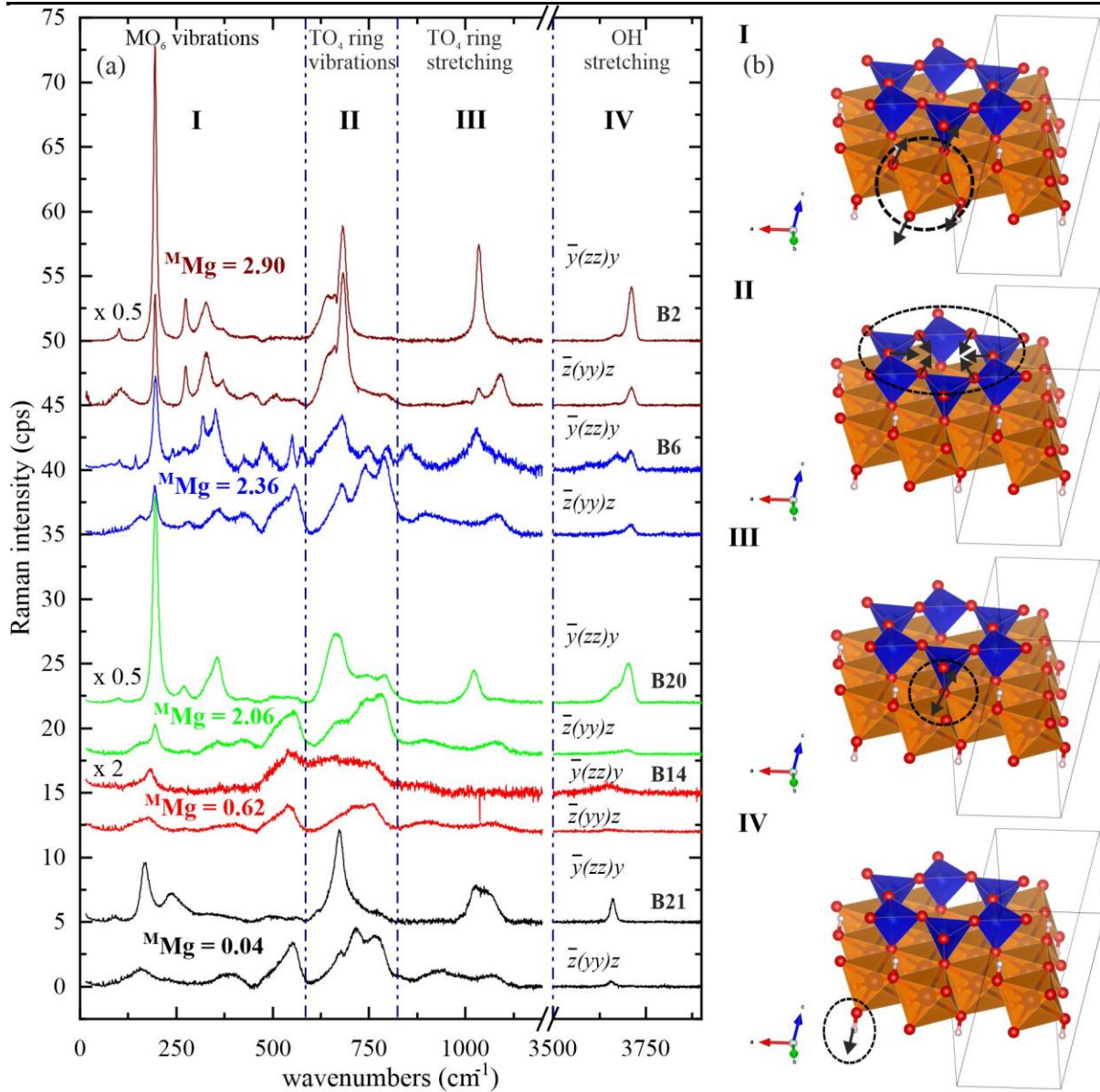


Figure 4: (a) Raman spectra of selected biotite samples with increasing octahedrally coordinated Mg content in apfu from bottom to top. Spectra with the same colour refer to the same sample and were measured in horizontal and vertical parallel-polarized geometries. The spectra are vertically offset for clarity. (b) Sketches illustrate the type of dominating atomic displacements within each spectral range (I-IV). VESTA software package (Momma and Izumi, 2008) was used to plot the atomic structures.

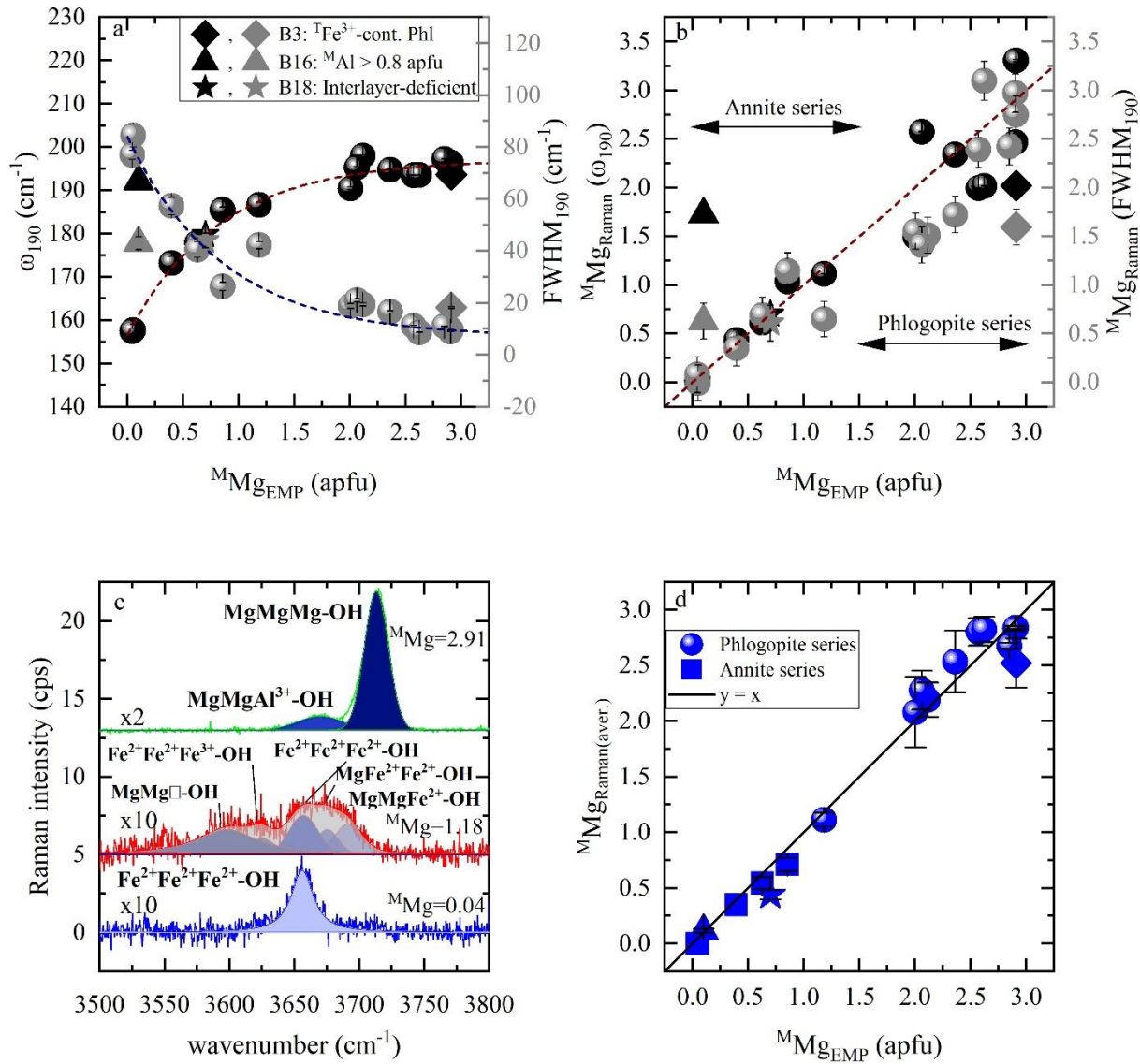


Figure 5: Estimation of ^MMg content according to MO_6 vibrations and OH bond-stretching bands: (a) Raman peak position at $\sim 190 \text{ cm}^{-1}$ vs. ^MMg (black symbols) and FWHM_{190} vs. ^MMg (gray symbols), (b) ^MMg content derived from the Raman spectroscopic analysis ($^M\text{Mg}_{\text{Raman}}$) of ω_{190} (black symbols) and FWHM_{190} (gray symbols) vs. that calculated from EMPA ($^M\text{Mg}_{\text{EMP}}$), and (c) OH-stretching vibrations of three representative biotites (Mg-richest; sample B1, Mg-poorest; sample B21; and with an intermediate composition, sample B12) are presented in horizontal parallel-polarized spectra. (d) $^M\text{Mg}_{\text{EMP}}$ vs. $^M\text{Mg}_{\text{Raman}}$ of the OH-stretching region of both parallel-polarized geometries. Deviating points in (a), (b), and (d): rhombus denotes a ^TFe³⁺-containing OH-rich phlogopite (Phl), triangle an aluminian F-rich annite with ^MAl > 0.8 apfu and star a magnesian interlayer-deficient annite.

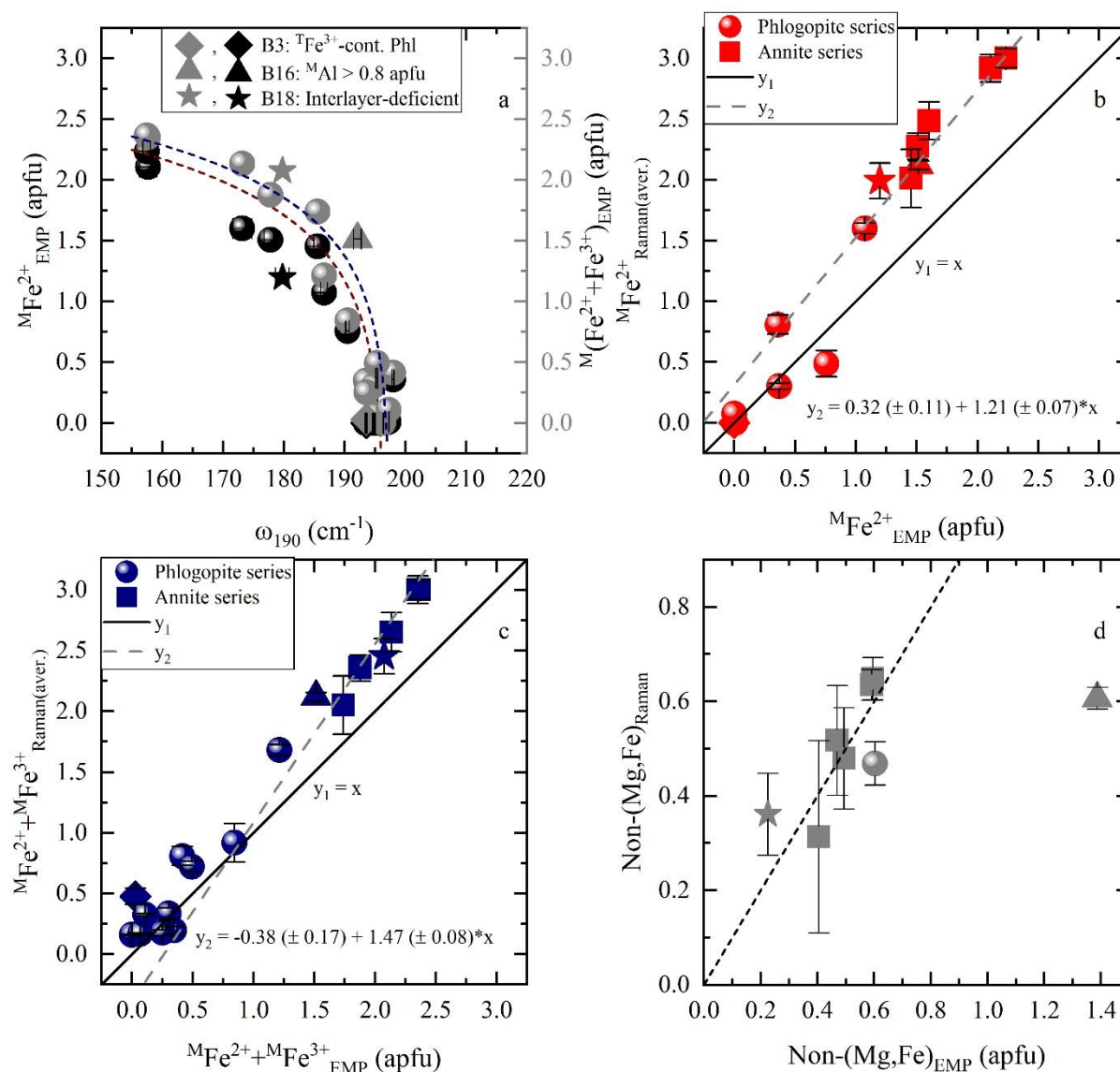


Figure 6: Estimation of MFe^{2+} and $\text{M}(\text{Fe}^{2+} + \text{Fe}^{3+})$ contents according to MO_6 vibrations and OH bond-stretching bands: (a) MFe^{2+} amount vs. Raman peak position at 190 cm^{-1} (black symbols) and $\text{M}(\text{Fe}^{2+} + \text{Fe}^{3+})$ content vs. ω_{190} (grey symbols), (b) MFe^{2+} from the Raman spectroscopic analysis ($\text{MFe}^{2+}_{\text{Raman}}$) of the OH-stretching vibrations vs. that calculated from EMPA ($\text{MFe}^{2+}_{\text{EMP}}$), and (c) $\text{M}(\text{Fe}^{2+} + \text{Fe}^{3+})$ from the Raman spectroscopic analysis [$\text{M}(\text{Fe}^{2+} + \text{Fe}^{3+}_{\text{Raman}})$] of the OH-stretching region vs. that calculated from EMPA [$\text{M}(\text{Fe}^{2+} + \text{Fe}^{3+}_{\text{EMP}})$]. (d) Non-(Mg,Fe) cationic content at the M-site of the samples deviating from the one-to-one correlation lines of Figs. 6b and 6c, where non-(Mg,Fe) amount from the Raman spectroscopic analysis [$\text{non-(Mg,Fe)}_{\text{Raman}}$] was plotted vs. that calculated from EMPA [$\text{non-(Mg,Fe)}_{\text{EMP}}$]. Deviating data points mentioned in the legend are same as in Fig. 5.

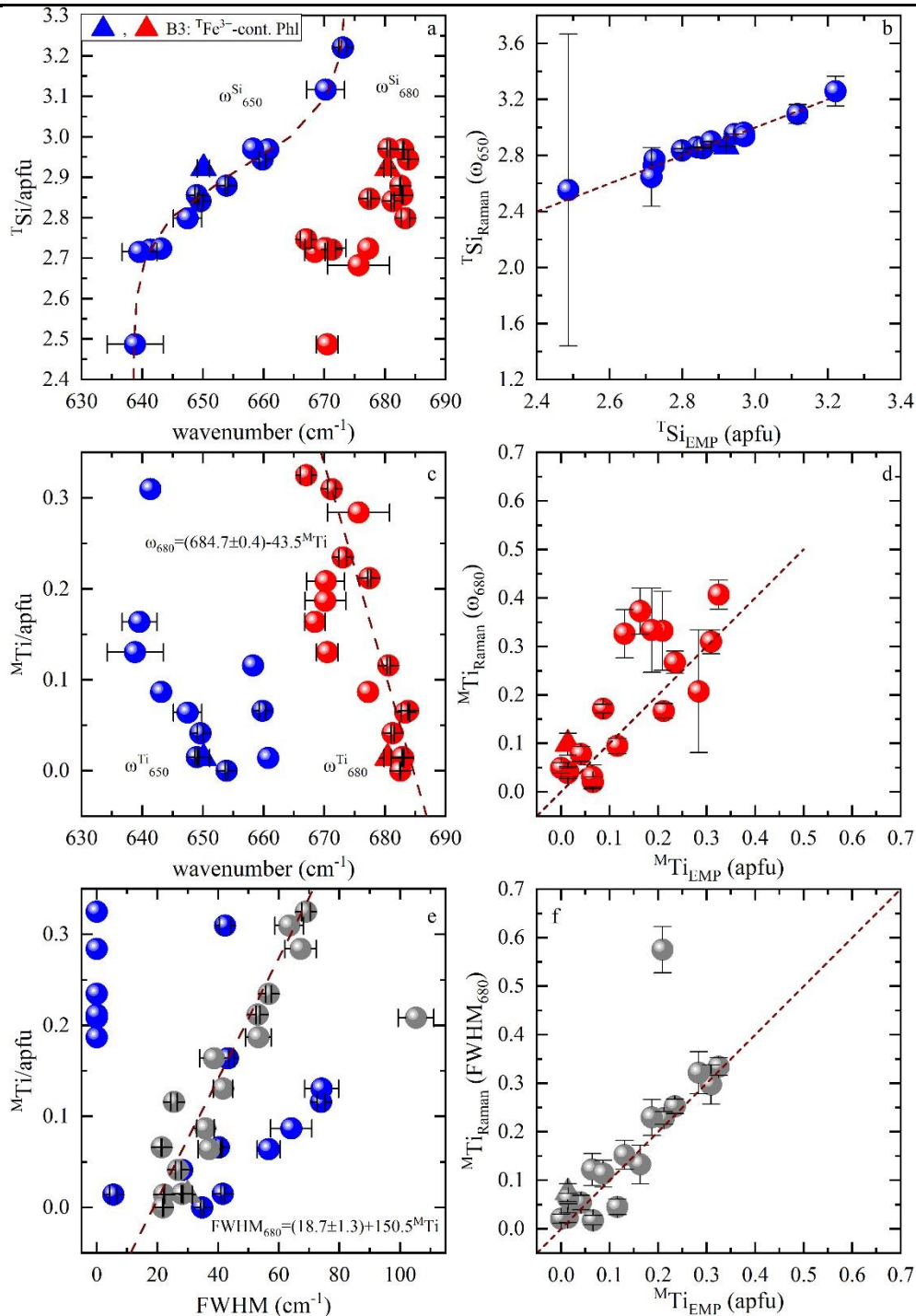


Figure 7: Estimation of ^{29}Si and $^{\text{M}}\text{Ti}$ contents in accordance with the TO_4 -ring modes near 650 cm^{-1} and 680 cm^{-1} : (a) ^{29}Si amount vs. Raman peak position at ~ 650 (blue symbols) and $\sim 680\text{ cm}^{-1}$ (red symbols), (b) ^{29}Si content derived from the Raman spectroscopic analysis ($^{29}\text{Si}_{\text{Raman}}$) of ω_{650} vs. that determined from EMPA ($^{29}\text{Si}_{\text{EMP}}$), (c) $^{\text{M}}\text{Ti}$ content vs. Raman peak position at ~ 650 (blue symbols) and $\sim 680\text{ cm}^{-1}$ (red symbols), (d) $^{\text{M}}\text{Ti}$ content obtained from the Raman spectroscopic analysis ($^{\text{M}}\text{Ti}_{\text{Raman}}$) of ω_{680} vs. that determined from EMPA ($^{\text{M}}\text{Ti}_{\text{EMP}}$), (e) $^{\text{M}}\text{Ti}$ amount vs. FWHM at ~ 650 (blue symbols) and $\sim 680\text{ cm}^{-1}$ (grey symbols), and (f) $^{\text{M}}\text{Ti}$ content obtained from the Raman spectroscopic analysis ($^{\text{M}}\text{Ti}_{\text{Raman}}$) of FWHM_{680} vs. that determined from EMPA ($^{\text{M}}\text{Ti}_{\text{EMP}}$).

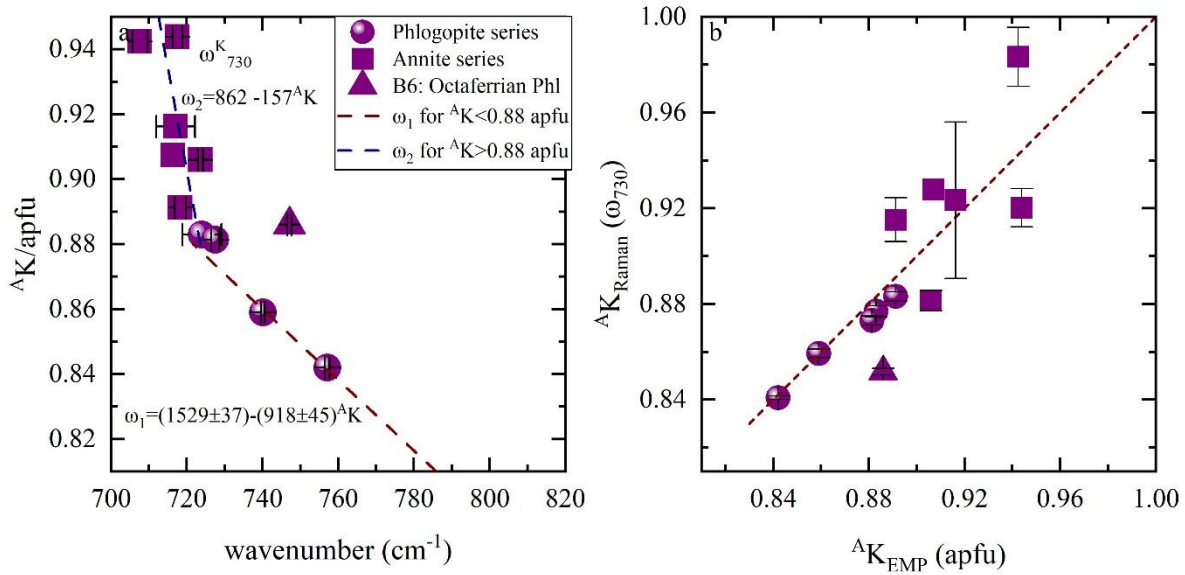


Figure 8: (a) Content of A-site coordinated K vs ω_{730} , where the Raman spectroscopic data are emerging from the $\bar{y}(zz)y$ scattering geometry, while in (b) $^A\text{K}_{\text{Raman}}$ vs $^A\text{K}_{\text{EMP}}$ estimated from both ω_1 and ω_2 linear trends in (a). Deviating point: triangle indicates sample B6; a phlogopite containing octahedrally coordinated Fe^{3+} at concentrations of ~ 0.30 apfu.

Table 1: Biotite chemical formulae (in apfu) calculated from EMPA and Mössbauer spectroscopy (for the samples with an asterisk) on the basis of 12 anions at the X site. Sample provenance and biotite names according to IMA nomenclature (Rieder et al. 1998), are provided as well.

Sample	Location	Name	${}^A\text{K}^M(\text{Mg}_{3-x}\text{Fe}_{x^{2+}})\text{T}(\text{AlSi}_3)\text{O}_{10}^X(\text{OH}_2\text{F})_2^a$			
			Interlayer site (A)	Octahedral site (M)	Tetrahedral site (T)	Anionic site (X)
B1	York, Ontario, Canada	Sodian F-rich phlogopite	$\text{K}_{0.84}\text{Na}_{0.12}\text{Ba}_{0.01}\square_{0.03}$	$\text{Mg}_{2.91}\text{Al}_{0.12}\text{Ti}_{0.07}$	$\text{Si}_{2.94}\text{Al}_{1.06}$	$\text{OH}_{1.08}\text{F}_{0.54}\text{O}_{0.38}$
B2	Portland, Quebec, Canada	(OH)-rich fluorophlogopite	$\text{K}_{0.92}\text{Na}_{0.02}\text{Ba}_{0.01}\square_{0.05}$	$\text{Mg}_{2.90}\text{Fe}^{3+}_{0.07}\text{Al}_{0.02}\text{Ti}_{0.01}$	$\text{Si}_{2.97}\text{Al}_{1.03}$	$\text{F}_{1.10}\text{OH}_{0.84}\text{O}_{0.06}$
B4*	Katugin river, Siberia, Russia	Tetra-ferri-containing fluorannite	$\text{K}_{0.91}\text{Na}_{0.04}\square_{0.05}$	$\text{Fe}^{2+}_{2.11}\text{Fe}^{3+}_{0.25}\text{Ti}_{0.21}\text{Mn}_{0.07}\text{Zn}_{0.07}\text{Mg}_{0.05}\square_{0.23}$	$\text{Si}_{3.12}\text{Al}_{0.78}\text{Fe}^{3+}_{0.10}$	$\text{F}_{1.02}\text{OH}_{0.74}\text{O}_{0.23}\text{Cl}_{0.01}$
B5	Kovdor, Russia	Octaferrian phlogopite	$\text{K}_{0.88}\text{Na}_{0.06}\text{Ba}_{0.02}\square_{0.04}$	$\text{Mg}_{2.57}\text{Fe}^{3+}_{0.35}\text{Ti}_{0.04}\text{Al}_{0.03}\square_{0.01}$	$\text{Si}_{2.84}\text{Al}_{1.16}$	$\text{OH}_{1.67}\text{O}_{0.28}\text{F}_{0.05}$
B6	Phalaborwa, South Africa	F-containing octaferrian phlogopite	$\text{K}_{0.89}\text{Na}_{0.03}\text{Ba}_{0.01}\square_{0.07}$	$\text{Mg}_{2.36}\text{Fe}^{3+}_{0.30}\text{Ti}_{0.21}\text{Al}_{0.07}\text{Cr}_{0.01}\text{Mn}_{0.01}\square_{0.04}$	$\text{Si}_{2.85}\text{Al}_{1.15}$	$\text{OH}_{1.25}\text{O}_{0.53}\text{F}_{0.18}\text{Cl}_{0.04}$
B7	Farmsen, Hamburg, Germany	(OH)-rich fluorophlogopite	$\text{K}_{0.90}\text{Na}_{0.04}\text{Ba}_{0.04}\square_{0.02}$	$\text{Mg}_{2.85}\text{Fe}^{3+}_{0.10}\text{Fe}^{2+}_{0.01}\text{Al}_{0.02}\text{Ti}_{0.02}$	$\text{Si}_{2.86}\text{Al}_{1.14}$	$\text{F}_{1.21}\text{OH}_{0.77}\text{O}_{0.02}$
B8	Laacher See, Eifel, Germany	Titanian ferroan oxy-rich phlogopite	$\text{K}_{0.91}\text{Na}_{0.06}\text{Ba}_{0.02}\square_{0.01}$	$\text{Mg}_{2.12}\text{Fe}^{2+}_{0.36}\text{Ti}_{0.31}\text{Al}_{0.19}\text{Fe}^{3+}_{0.06}\text{Cr}_{0.01}$	$\text{Si}_{2.72}\text{Al}_{1.28}$	$\text{OH}_{1.22}\text{O}_{0.69}\text{F}_{0.09}$
B10	Moravița, Romania	Octa-ferri-containing phlogopite	$\text{K}_{0.91}\text{Na}_{0.03}\square_{0.06}$	$\text{Mg}_{2.62}\text{Fe}^{3+}_{0.25}\text{Al}_{0.11}\square_{0.02}$	$\text{Si}_{2.88}\text{Al}_{1.12}$	$\text{OH}_{1.76}\text{O}_{0.16}\text{F}_{0.08}$
B12	Upper Palatinate, Bavaria, Germany	Aluminian ferroan phlogopite	$\text{K}_{0.91}\text{Na}_{0.02}\square_{0.07}$	$\text{Mg}_{1.18}\text{Fe}^{2+}_{1.07}\text{Al}_{0.36}\text{Ti}_{0.16}\text{Fe}^{3+}_{0.14}\text{Mn}_{0.02}\square_{0.07}$	$\text{Si}_{2.72}\text{Al}_{1.28}$	$\text{OH}_{1.65}\text{O}_{0.35}$
B13*	Johnstown, California, USA	Ti-containing magnesian annite	$\text{K}_{0.89}\text{Na}_{0.02}\square_{0.09}$	$\text{Fe}^{2+}_{1.60}\text{Fe}^{3+}_{0.53}\text{Mg}_{0.39}\text{Ti}_{0.19}\text{Al}_{0.08}\text{Mn}_{0.04}\square_{0.15}$	$\text{Si}_{2.73}\text{Al}_{1.27}$	$\text{OH}_{1.60}\text{O}_{0.34}\text{F}_{0.05}\text{Cl}_{0.01}$
B14*	Ilmensky Mountains, Russia	Ti-containing magnesian oxy-rich annite	$\text{K}_{0.94}\text{Na}_{0.05}\text{Ba}_{0.01}$	$\text{Fe}^{2+}_{1.51}\text{Mg}_{0.63}\text{Fe}^{3+}_{0.37}\text{Ti}_{0.28}\text{Mn}_{0.08}\text{Al}_{0.03}\text{Zn}_{0.01}\square_{0.07}$	$\text{Si}_{2.68}\text{Al}_{1.32}$	$\text{OH}_{1.25}\text{O}_{0.54}\text{F}_{0.21}$
B16	Auvergne, France	Aluminian F-rich annite	$\text{K}_{0.92}\text{Na}_{0.04}\square_{0.04}$	$\text{Fe}^{2+}_{1.51}\text{Al}_{0.89}\text{Mg}_{0.10}\text{Ti}_{0.06}\text{Mn}_{0.06}\text{Zn}_{0.02}\square_{0.36}$	$\text{Si}_{2.80}\text{Al}_{1.20}$	$\text{OH}_{1.30}\text{F}_{0.63}\text{O}_{0.07}$
B17*	Sebastopol, Ontario, Canada	Ferroan (OH)-rich fluorophlogopite	$\text{K}_{0.88}\text{Na}_{0.08}\text{Ba}_{0.01}\square_{0.03}$	$\text{Mg}_{2.01}\text{Fe}^{2+}_{0.76}\text{Ti}_{0.12}\text{Fe}^{3+}_{0.09}\text{Mn}_{0.02}\text{Al}_{0.01}\text{Zn}_{0.01}$	$\text{Si}_{2.97}\text{Al}_{1.03}$	$\text{F}_{0.88}\text{OH}_{0.83}\text{O}_{0.28}\text{Cl}_{0.01}$
B18	Ytterby, Sweden	Magnesian interlayer-deficient annite	$\text{K}_{0.63}\square_{0.37}$	$\text{Fe}^{2+}_{1.20}\text{Fe}^{3+}_{0.88}\text{Mg}_{0.70}\text{Ti}_{0.13}\text{Al}_{0.04}\text{Mn}_{0.02}\square_{0.02}$	$\text{Si}_{2.49}\text{Al}_{1.51}$	$\text{OH}_{1.66}\text{O}_{0.22}\text{F}_{0.06}\text{Cl}_{0.06}$
B19*	Faraday, Ontario, Canada	F-rich magnesian annite	$\text{K}_{0.94}\text{Na}_{0.05}\square_{0.01}$	$\text{Fe}^{2+}_{1.45}\text{Mg}_{0.86}\text{Fe}^{3+}_{0.29}\text{Al}_{0.14}\text{Ti}_{0.09}\text{Zn}_{0.03}\text{Mn}_{0.02}\square_{0.12}$	$\text{Si}_{2.72}\text{Al}_{1.28}$	$\text{OH}_{1.42}\text{F}_{0.50}\text{O}_{0.08}$
B20	Ústí nad Labem, Czech Republic	Titanian ferroan oxy-rich phlogopite	$\text{K}_{0.86}\text{Na}_{0.08}\text{Ba}_{0.01}\square_{0.05}$	$\text{Mg}_{2.06}\text{Fe}^{2+}_{0.37}\text{Ti}_{0.33}\text{Al}_{0.16}\text{Fe}^{3+}_{0.12}\text{Cr}_{0.01}$	$\text{Si}_{2.75}\text{Al}_{1.25}$	$\text{OH}_{1.18}\text{O}_{0.76}\text{F}_{0.06}$
B21*	Kalar Mountains, Siberia, Russia	Tetra-ferri- and Ti-containing fluorannite	$\text{K}_{0.91}\text{Na}_{0.02}\text{Ba}_{0.01}\square_{0.05}$	$\text{Fe}^{2+}_{2.24}\text{Ti}_{0.23}\text{Fe}^{3+}_{0.13}\text{Mn}_{0.06}\text{Zn}_{0.05}\text{Mg}_{0.04}\square_{0.25}$	$\text{Si}_{3.22}\text{Al}_{0.67}\text{Fe}^{3+}_{0.11}$	$\text{F}_{1.03}\text{OH}_{0.71}\text{O}_{0.25}\text{Cl}_{0.01}$

^a Cationic and anionic site occupancy is given in decreasing order of abundance.

Table 2: Group-theory analysis for the monoclinic C2/m space group of biotite.

Site	Wyckoff position	Raman (A_g , B_g) and IR (A_u , B_u) active phonon modes
^A K	2b	A_u+2B_u (acoustic)
<i>M</i> 1	2c	A_u+2B_u
<i>M</i> 2	4h	$A_g+2B_g+A_u+2B_u$
<i>T</i>	8j	$3A_g+3B_g+3A_u+3B_u$
O1	8j	$3A_g+3B_g+3A_u+3B_u$
O2	4i	$2A_g+B_g+1A_u+2B_u$
O3	8j	$3A_g+3B_g+3A_u+3B_u$
^X O4	4i	$2A_g+B_g+1A_u+2B_u$
^X H	4i	$2A_g+B_g+1A_u+2B_u$
Total		30 Raman 33 IR phonon modes

Table 3: Raman peak assignment of the OH-stretching vibrations associated with various local configurations of the octahedrally coordinated cations.

Horizontal				Vertical			
Sample	Wavenumber	Local configuration	Reference	Sample	Wavenumber	Local configuration	Reference
B1, B2, B5, B6, B7, B8, B10, B17, B20	3705-3716	MgMgMg-OH ⁻ -K-OH ⁻	Tili et al. (1989), Scordari et al. (2006), Lacalamita et al. (2011, 2020)	B1, B2, B5, B6, B7, B10, B17, B20	3708-3714	MgMgMg-OH ⁻ -K-OH ⁻	Tili et al. (1989), Scordari et al. (2006), Lacalamita et al. (2011, 2020)
B3	3696	MgMgMg-OH ⁻ -K-F ⁻	This work	B3	3696	MgMgMg-OH ⁻ -K-F ⁻	This work
B8, B12, B17, B20	3692-3698	MgMgFe ²⁺ -OH ⁻ -K-OH ⁻	Lacalamita et al. (2011), Scordari et al. (2012)	B8, B10, B12, B17, B20	3693-3701	MgMgFe ²⁺ -OH ⁻ -K-OH ⁻	Lacalamita et al. (2011), Scordari et al. (2012)
B6, B8, B10, B20	3681-3686	MgMgMg-OH ⁻ -K-O ²⁻	Scordari et al. (2006, 2012)	B5, B8, B10, B20	3681-3686	MgMgMg-OH ⁻ -K-O ²⁻	Scordari et al. (2006, 2012)
B12, B13, B14, B18, B19	3671-3676	MgFe ²⁺ Fe ²⁺ -OH ⁻	Lacalamita et al. (2011)	B12, B13, B14, B19	3674-3677	MgFe ²⁺ Fe ²⁺ -OH ⁻	Lacalamita et al. (2011)
B1, B2, B3, B5, B6, B7, B10, B17, B20	3660-3670	MgMgFe ³⁺ -OH ⁻ -K-OH ⁻ or MgMgAl-OH ⁻ -K-OH ⁻	Tili et al. (1989), Scordari et al. (2006, 2012), Lacalamita et al. (2011), Schingaro et al. (2013)	B1, B2, B3, B5, B6, B7, B10, B17, B20	3660-3672	MgMgFe ³⁺ -OH ⁻ -K-OH ⁻ or MgMgAl-OH ⁻ -K-OH ⁻	Tili et al. (1989), Scordari et al. (2006, 2012), Lacalamita et al. (2011), Schingaro et al. (2013)
B4, B12, B13, B14, B16, B18, B19, B21	3648-3656	Fe ²⁺ Fe ²⁺ Fe ²⁺ -OH ⁻ -K-OH ⁻	Redhammer et al. (2000)	B4, B12, B13, B14, B16, B18, B19, B21	3647-3660	Fe ²⁺ Fe ²⁺ Fe ²⁺ -OH ⁻ -K-OH ⁻	Redhammer et al. (2000)
B12	3625-3630	Fe ²⁺ Fe ²⁺ Fe ³⁺ -OH ⁻ -K-OH ⁻ or AlAl□-OH ⁻ -K-OH ⁻	Redhammer et al. (2000), Libowitzky and Beran (2004), Scordari et al. (2008)	B4, B12, B13, B14, B18, B19	3625-3630	Fe ²⁺ Fe ²⁺ Fe ³⁺ -OH ⁻ -K-OH ⁻ or AlAl□-OH ⁻ -K-OH ⁻	Redhammer et al. (2000), Libowitzky and Beran (2004), Scordari et al. (2008)
B12, B18, B19	3600-3607	MgMg□-OH ⁻	Kodama et al. (1974), Lacalamita et al. (20020)	B6, B12, B14, B16	3600-3603	MgMg□-OH ⁻	Kodama et al. (1974), Lacalamita et al. (20020)
B16	3596	Fe ²⁺ Al□-OH ⁻ -K-OH ⁻	Redhammer et al. (2000)				
B18	3570	Fe ²⁺ Fe ²⁺ Fe ³⁺ -OH ⁻ - ^A □-OH ⁻	This work	B18	3570	Fe ²⁺ Fe ²⁺ Fe ³⁺ -OH ⁻ - ^A □-OH ⁻	This work

C.b. Supplementary material

Non-destructive determination of the biotite crystal chemistry using Raman spectroscopy: how far we can go?

Stylios Aspiotis^{1,*}, Jochen Schlüter², Günther J. Redhammer³, Boriana Mihailova¹

¹Fachbereich Erdsystemwissenschaften, Universität Hamburg, Grindelallee 48, 20146 Hamburg, email: stylios.aspiotis@uni-hamburg.de, email: boriana.mihailova@uni-hamburg.de

²Museum der Natur Hamburg-Mineralogie, Leibniz-Institut zur Analyse des Biodiversitätswandels (LIB), Grindelallee 48, 20146 Hamburg, email: jochen.schluter@uni-hamburg.de

³Fachbereich Chemie und Physik der Materialien, Paris-Lodron Universität Salzburg, 5020 Salzburg, Austria, email: guenther.redhammer@plus.ac.at

*Correspondence to: Stylios Aspiotis (stylios.aspiotis@uni-hamburg.de)

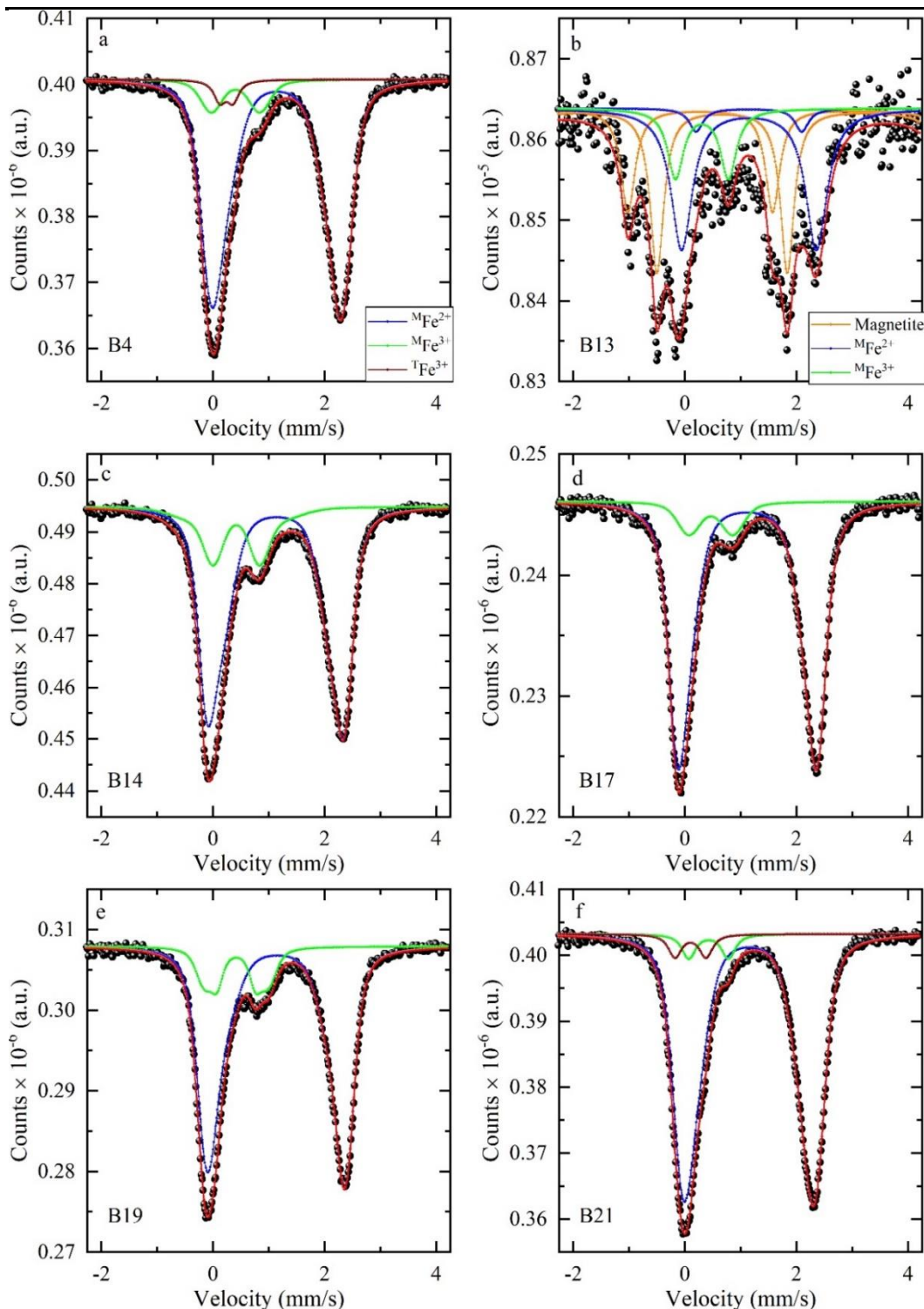


Figure S1: (a) - (f) Room-temperature experimental ^{57}Fe Mössbauer spectra (circles) along with the fitting doublet functions (green, blue, and brown lines) and the resulting spectrum (red line). For sample B13 (b) a classical approach with Lorentzian-shaped doublets (one for $^{\text{M}}\text{Fe}^{3+}$ and two for $^{\text{M}}\text{Fe}^{2+}$) was used instead of the quadrupole splitting distribution (QSD) approach due to the presence of magnetite of $\sim 70\%$. For sample B19 (e) the green line is the QSD approach of $^{\text{M}}\text{Fe}^{3+}$, composed of two doublets due to differences in the local distortion geometry around $^{\text{M}}\text{Fe}^{3+}$.

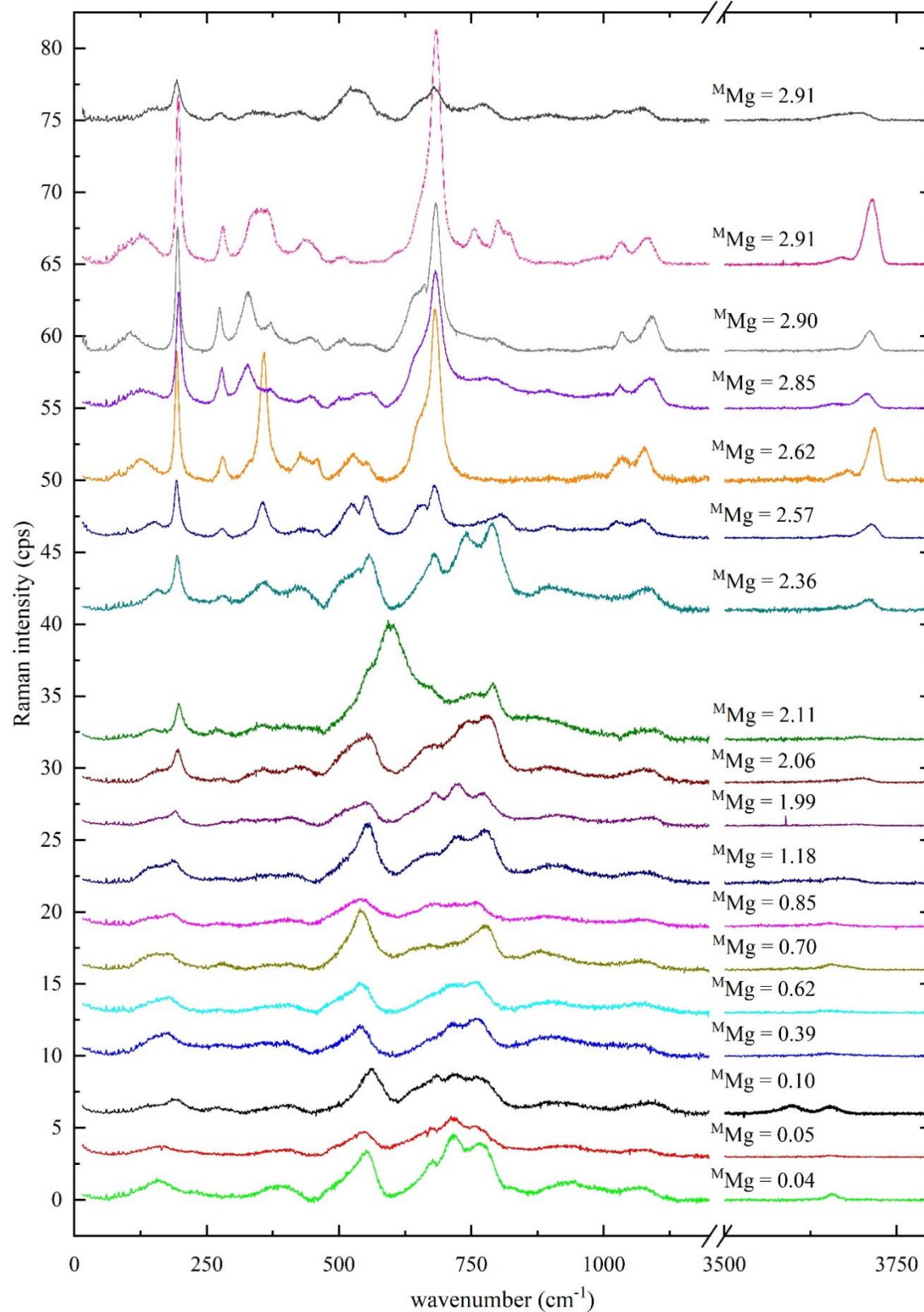


Figure S2: Raman spectra of the analysed biotites in horizontal parallel-polarized geometry, where ^MMg content in apfu increases from bottom to top. For better comparison, the spectra are vertically offset.

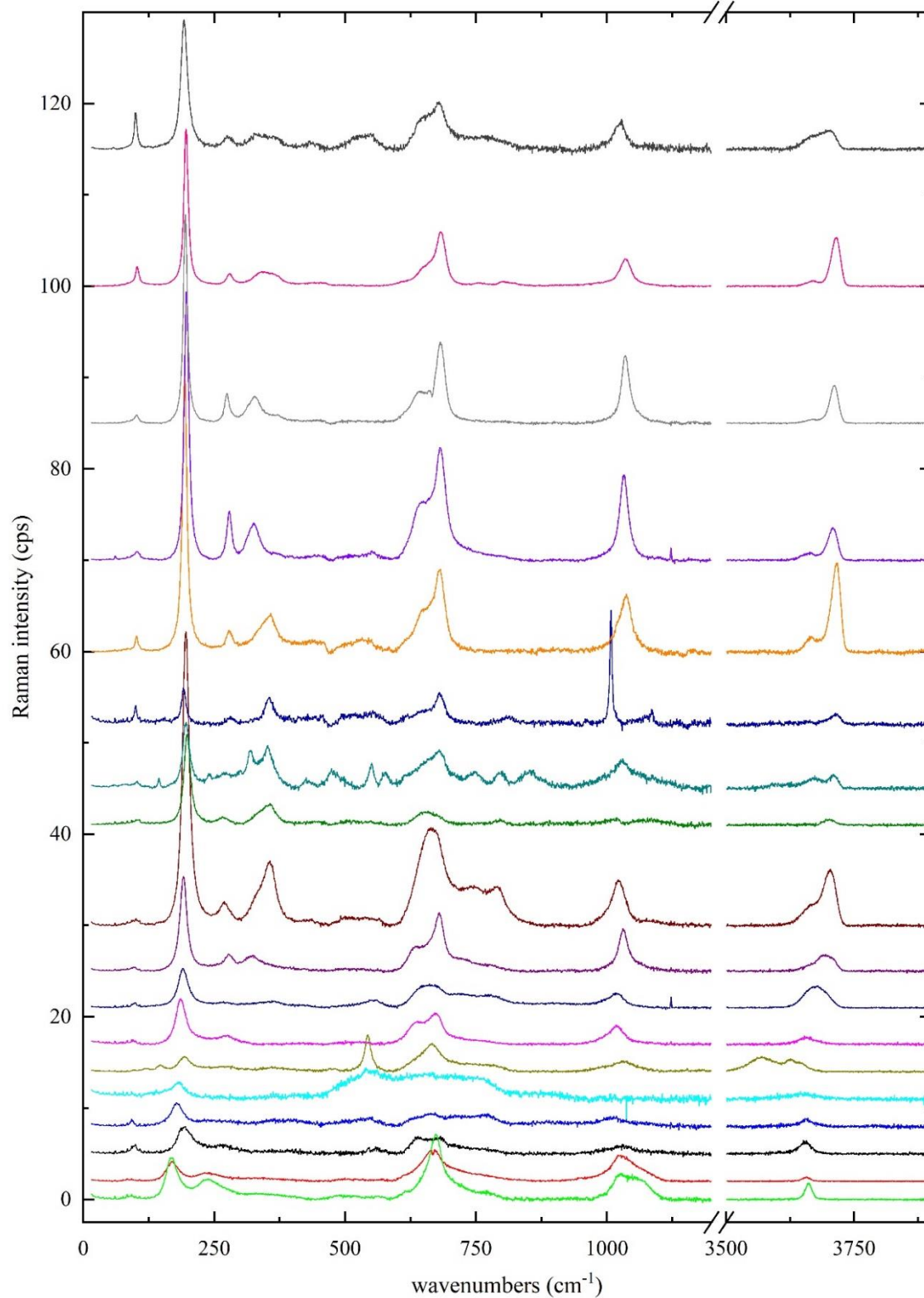


Figure S3: Raman spectra of the studied biotites in vertical parallel-polarized geometry, where ^{Mg} content increases from bottom to top. Colours are the same as in figure S1 and correspond to equal Mg contents. For better comparison, the spectra are vertically offset.

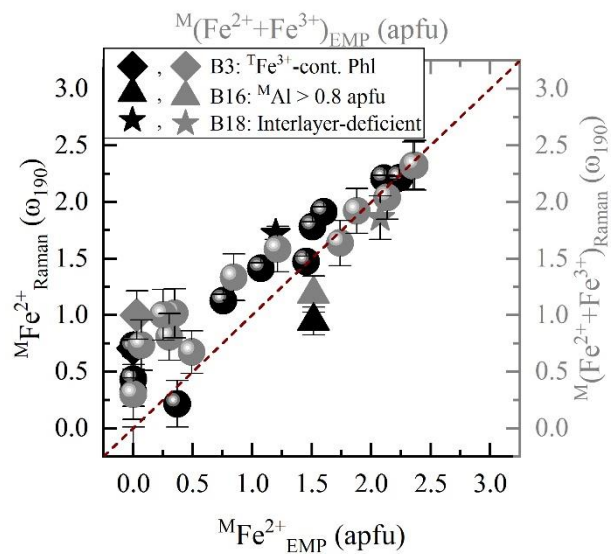


Figure S4: Estimation of $M\text{Fe}^{2+}$ and $M(\text{Fe}^{2+}+\text{Fe}^{3+})$ contents according to MO_6 vibrations: $M\text{Fe}^{2+}$ content derived from the Raman spectroscopic analysis ($M\text{Fe}^{2+}_{\text{Raman}}$) of ω_{190} (black symbols) and $M(\text{Fe}^{2+}+\text{Fe}^{3+})$ content (grey symbols) vs. that calculated from EMPA [$M(\text{Fe}^{2+}+\text{Fe}^{3+})_{\text{EMPA}}$]. Deviating points mentioned in the legend are same as in Fig. 5.

Table S1: Average chemical composition (wt. %) and statistical standard deviation (σ) of the studied biotite crystals. FeO, H₂O, and Fe₂O₃ were calculated following the guidelines of the charge balance approach of Li et al. (2020) and via Mössbauer spectroscopy (FeO and Fe₂O₃ of the samples with an asterisk). Abbreviations in the table: T: total; calc.: calculated; b.d.l.: below detection limit; init.: initial; n.d.: not determined.

	B1	B2	B3	B4*	B5	B6	B7	B8	B10
SiO ₂	41.9(3)	42.5(1)	35.8(1.1)	36.5(1)	39.5(4)	39.2(3)	40.2(1)	36.6(4)	40.3(8)
TiO ₂	1.25(36)	0.27(2)	0.22(2)	3.26(4)	0.75(5)	3.89(5)	0.27(1)	5.53(15)	0.01(3)
Al ₂ O ₃	14.3(1)	12.8(1)	10.9(4)	7.73(8)	14.1(2)	14.3(2)	14.0(1)	16.8(2)	14.6(2)
FeO _T	0.05(5)	1.16(5)	0.98(6)	34.4(2)	5.8(1)	4.99(9)	1.84(7)	6.66(15)	4.20(3)
MnO	b.d.l.	0.001(7)	b.d.l.	0.99(3)	0.04(3)	0.13(2)	b.d.l.	0.008(20)	0.08(1)
MgO	27.8(2)	27.8(1)	23.9(7)	0.41(2)	24.0(2)	21.8(2)	26.9(1)	19.1(5)	24.6(7)
CaO	b.d.l.	b.d.l.	0.01(3)	b.d.l.	0.003(11)	b.d.l.	0.001(5)	0.02(3)	b.d.l.
Na ₂ O	0.90(4)	0.18(2)	0.16(1)	0.26(2)	0.43(1)	0.18(3)	0.26(1)	0.41(4)	0.18(2)
K ₂ O	9.39(9)	10.3(1)	8.49(29)	8.37(7)	9.62(10)	9.56(9)	9.91(8)	9.55(26)	10.0(2)
Cr ₂ O ₃	b.d.l.	b.d.l.	b.d.l.	b.d.l.	0.02(2)	0.10(1)	b.d.l.	0.18(1)	b.d.l.
NiO	b.d.l.	b.d.l.	b.d.l.	b.d.l.	0.06(1)	b.d.l.	b.d.l.	0.07(1)	b.d.l.
CuO	b.d.l.	b.d.l.	b.d.l.	b.d.l.	b.d.l.	b.d.l.	b.d.l.	b.d.l.	b.d.l.
ZnO	b.d.l.	b.d.l.	b.d.l.	1.08(2)	b.d.l.	b.d.l.	b.d.l.	b.d.l.	0.001(9)
SrO	b.d.l.	b.d.l.	b.d.l.	b.d.l.	b.d.l.	b.d.l.	0.04(4)	b.d.l.	b.d.l.
BaO	0.20(2)	0.46(2)	0.40(2)	0.04(4)	0.56(2)	0.45(4)	1.35(4)	0.52(3)	b.d.l.
Cl	0.03(4)	0.003(9)	0.38(10)	0.06(1)	0.002(7)	0.35(1)	0.02(2)	0.015(29)	0.01(2)
F	2.43(8)	4.95(9)	4.88(13)	3.77(9)	0.21(3)	0.80(4)	5.37(9)	0.37(16)	0.37(3)
-O=F+Cl	1.03(3)	2.09(4)	2.14(5)	1.60(4)	0.09(1)	0.42(2)	2.26(4)	0.16(7)	0.16(2)
Sum init.	97.2(6)	98.4(2)	84.0(2.5)	95.3(3)	94.9(5)	95.3(6)	97.9(2)	95.6(1.4)	94.3(1.2)
FeO calc.	n.d.	0.00	0.17	29.52	0.00	0.00	0.13	5.74	0.00
Fe ₂ O ₃ calc.	n.d.	1.29	0.88	5.43	6.43	5.54	1.90	1.02	4.67
H ₂ O calc.	2.30	1.79	1.57	1.30	3.49	2.58	1.63	2.46	3.69
Sum calc.	99.5(6)	100.3(2)	85.7(2.4)	97.1(1)	99.1(4)	98.5(6)	99.7(1)	98.1(1.3)	98.5(9)

	B12	B13*	B14*	B16	B17*	B18	B19*	B20	B21*
SiO ₂	34.9(3)	33.7(3)	32.7(7)	34.1(3)	39.4(3)	30.7(2.4)	33.6(4)	35.9(5)	37.0(3)
TiO ₂	2.80(5)	3.07(11)	4.60(17)	1.04(3)	2.05(5)	2.14(41)	1.42(3)	5.65(8)	3.58(6)
Al ₂ O ₃	17.9(2)	14.4(2)	14.2(4)	21.6(2)	11.7(1)	16.2(7)	14.9(2)	15.6(3)	6.49(7)
FeO _T	18.6(2)	31.5(3)	27.3(3)	22.0(4)	13.5(2)	30.6(2.1)	25.6(2)	7.68(18)	34.1(3)
MnO	0.3282)	0.52(2)	1.11(4)	0.91(3)	0.29(2)	0.33(4)	0.35(2)	0.02(3)	0.82(31)
MgO	10.2(1)	3.28(5)	5.13(28)	0.81(34)	17.9(2)	5.8(8)	7.07(10)	18.1(3)	0.33(2)
CaO	b.d.l.	0.01(3)	b.d.l.	b.d.l.	0.05(6)	0.12(24)	0.003(14)	0.03(2)	b.d.l.
Na ₂ O	0.14(1)	0.11(1)	0.29(3)	0.24(1)	0.53(2)	0.02(3)	0.32(4)	0.53(2)	0.15(2)
K ₂ O	9.13(8)	8.63(15)	8.99(11)	8.74(9)	9.18(14)	6.1(2.8)	9.12(12)	8.8(1.3)	8.16(12)
Cr ₂ O ₃	b.d.l.	b.d.l.	0.001(5)	b.d.l.	b.d.l.	b.d.l.	b.d.l.	0.23(1)	b.d.l.
NiO	b.d.l.	b.d.l.	b.d.l.	b.d.l.	0.001(5)	b.d.l.	b.d.l.	0.02(2)	b.d.l.
CuO	b.d.l.	b.d.l.	b.d.l.	b.d.l.	b.d.l.	b.d.l.	b.d.l.	b.d.l.	b.d.l.
ZnO	0.02(3)	0.07(4)	0.12(2)	0.26(2)	0.11(2)	0.004(17)	0.45(2)	b.d.l.	0.69(2)
SrO	b.d.l.	b.d.l.	b.d.l.	b.d.l.	b.d.l.	b.d.l.	b.d.l.	b.d.l.	b.d.l.
BaO	0.07(4)	0.07(4)	0.15(3)	b.d.l.	0.21(2)	0.007(23)	0.09(4)	0.44(3)	0.13(3)
Cl	0.01(1)	0.08(1)	0.001(7)	0.004(12)	0.07(1)	0.45(16)	0.02(2)	0.002(7)	0.07(1)
F	0.06(7)	0.18(4)	0.82(13)	2.44(8)	3.72(10)	0.23(10)	1.94(8)	0.24(4)	3.73(11)
-O=F+Cl	0.03(3)	0.09(2)	0.35(5)	1.03(4)	1.58(4)	0.20(7)	0.82(3)	0.10(2)	1.59(5)
Sum init.	94.2(5)	95.5(5)	95.0(1.2)	91.1(6)	97.1(4)	92.6(2.8)	94.0(7)	93.1(1.6)	93.7(6)
FeO calc.	16.48	23.64	21.93	22.03	12.02	17.66	21.40	5.78	30.75
Fe ₂ O ₃ calc.	2.41	8.76	6.02	0.00	1.54	14.39	4.70	2.11	3.71
H ₂ O calc.	3.17	2.95	2.29	2.37	1.66	3.06	2.62	2.31	1.22
Sum calc.	97.6(4)	99.3(3)	97.9(9)	93.5(2)	98.9(2)	97.1(7)	97.1(5)	95.6(1.4)	95.3(3)

Table S2: Mössbauer parameters determined by the Voigt based hyperfine distribution approach; IS = isomer shift (mm/s), QS = quadrupole splitting (mm/s), HWHM = Lorentzian half width at half maximum (mm/s), σ = Gaussian broadening to the underlying Lorentzian line width (mm/s), and A = relative area fraction.

Sample	χ^2	IS (mm/s)	QS (mm/s)	HWHM (mm/s)	σ (mm/s)	A (%)	Species
B4	0.645	1.145(2)	2.175(3)	0.123(8)	0.389(4)	85.7(5)	^M Fe ²⁺
		0.404(2)	0.867(4)		0.270(4)	10.1(4)	^M Fe ³⁺
		0.239(2)	0.236(4)		0.053(3)	4.2(5)	^T Fe ³⁺
B13*	0.721	1.15(2)	1.894(14)	0.15(2)	-	7.4(1.9)	^M Fe ²⁺
		1.151(9)	2.416(11)	0.151(6)	-	67.7(1.8)	^M Fe ²⁺
		0.309(13)	0.947(14)	0.172(5)	-	24.9(1.2)	^M Fe ³⁺
B14	0.807	1.133(2)	2.241(4)	0.124(6)	0.368(4)	80.2(4)	^M Fe ²⁺
		0.4188(3)	0.827(5)		0.249(3)	19.8(5)	^M Fe ³⁺
B17	0.685	1.123(2)	2.367(4)	0.134(5)	0.297(4)	89.1(7)	^M Fe ²⁺
		0.469(4)	0.788(3)		0.282(4)	10.1(8)	^M Fe ³⁺
B19	0.673	1.136(3)	2.311(5)	0.113(8)	0.385(4)	83.5(5)	^M Fe ²⁺
		0.416(3)	0.945(5)		0.272(4)	16.5(7)	^M Fe ³⁺
B21	0.685	1.151(3)	2.204(5)	0.124(5)	0.362(5)	90.3(5)	^M Fe ²⁺
		0.427(5)	0.711(7)		0.121(4)	5.0(7)	^M Fe ³⁺
		0.192(4)	0.556(5)		0.098(5)	4.7(5)	^T Fe ³⁺

* σ values not applicable for sample B13, due to the high fraction of magnetite (~ 70%) and thus the data were fitted with Lorentzian shaped lines and a full static Hamiltonian behind QS, IS, and internal magnetic field of magnetite. No Gaussian broadening of the lines is applied here.

Versicherung an Eides statt

Hiermit erkläre ich an Eides statt, dass ich die vorliegende Dissertationsschrift selbst verfasst und keine anderen als die angegebenen Quellen und Hilfsmittel benutzt habe.

A handwritten signature in blue ink, consisting of a series of connected loops and curves, positioned above the word 'Unterschrift'.

Hamburg, den 04.07.2023

Unterschrift